



City Research Online

City, University of London Institutional Repository

Citation: Cavouras, D. (1981). A study in the reconstruction of a three-dimensional object from its two-dimensional emission images, with application to the human heart. (Unpublished Doctoral thesis, The City University)

This is the accepted version of the paper.

This version of the publication may differ from the final published version.

Permanent repository link: <https://openaccess.city.ac.uk/id/eprint/34605/>

Link to published version:

Copyright: City Research Online aims to make research outputs of City, University of London available to a wider audience. Copyright and Moral Rights remain with the author(s) and/or copyright holders. URLs from City Research Online may be freely distributed and linked to.

Reuse: Copies of full items can be used for personal research or study, educational, or not-for-profit purposes without prior permission or charge. Provided that the authors, title and full bibliographic details are credited, a hyperlink and/or URL is given for the original metadata page and the content is not changed in any way.

City Research Online:

<http://openaccess.city.ac.uk/>

publications@city.ac.uk

THE CITY UNIVERSITY
DEPARTMENT OF SYSTEMS SCIENCE

'A STUDY IN THE RECONSTRUCTION OF A THREE-DIMENSIONAL OBJECT FROM ITS
TWO-DIMENSIONAL EMISSION IMAGES, WITH APPLICATION TO THE HUMAN HEART.'

DIONISIS CAVOURAS

A thesis submitted for the award of the degree of Doctor of Philosophy
in Systems Engineering.

January 1981.

Table of Contents

List of Illustrations.....	5
List of Tables.....	10
List of Abbreviations.....	11
Acknowledgements.....	13
Abstract.....	14
1 INTRODUCTION.....	15
1.1 OBJECTIVE.....	21
1.2 DIFFICULTIES.....	24
1.3 PROPOSED APPROACH.....	26
2 CRITICAL SURVEY OF APPLICABLE IMAGE PROCESSING METHODS.....	30
2.1 FILTERING.....	33
2.2 BOUNDARY DETECTION.....	42
2.3 METHODS FOR TOMOGRAPHIC RECONSTRUCTION.....	47
3 PROBLEM DEFINITION.....	52
3.1 HEART CHAMBER DESCRIPTION AND OPERATION.....	54
3.2 CORONARY HEART DISEASE.....	57
3.3 MODELLING THE HEART.....	58
3.4 DISCUSSION.....	64
4 DATA ACQUISITION AND DATA PROCESSING SYSTEMS.....	68
4.1 PATIENT EXAMINATION.....	70
4.2 DATA ACQUISITION SYSTEM (GAMMA-11).....	72
4.2.1 Gamma Camera Detection System.....	74
4.2.2 GAMMA-11 Computer System.....	77
4.2.3 Data Recording and File Structure.....	82
4.3 DATA PROCESSING SYSTEM (PDP-11/10).....	85
5 FORMATION AND PROPERTIES OF GAMMA CAMERA IMAGES.....	90
5.1 THE IMAGE.....	91
5.1.1 Mathematical analysis of image formation process.....	92
5.1.2 Radioactive source-Process of radioactive decay.....	95
5.1.3 Image formation procedure.....	97
5.2 SOURCES OF DEGRADATION.....	100
5.2.1 Poisson Noise.....	101
5.2.2 Scattering.....	104
5.2.3 Attenuation.....	106
6 PREPROCESSING ALGORITHMS.....	111
6.1 SCATTERING ELIMINATION.....	112

6.1.1	Assessing the restoration problem.....	113
6.1.2	The Restoration.....	117
6.1.3	Practical Implementation.....	123
6.2	ATTENUATION ELIMINATION.....	126
6.3	NOISE ELIMINATION.....	127
6.4	BOUNDARY DETECTION AND IMAGE PREPARATION.....	128
7	RECONSTRUCTION ALGORITHMS.....	131
7.1	DESCRIPTION.....	134
7.1.1	Practical Implementation.....	139
7.2	STRAIGHT PSEUDOINVERSE METHOD.....	142
7.2.1	The Generalized Inverse or Pseudoinverse.....	143
7.2.2	Description of the SP-Algorithm.....	145
7.2.3	Minimum Least Square Estimate method (MLSE).....	148
7.2.4	Mathematical derivation of the MLSE method.....	150
7.2.5	Description of the MLSE-Algorithm.....	151
7.3	COMPARISON BETWEEN SP AND MLSE ALGORITHMS.....	153
8	CONE PHANTOM RECONSTRUCTION EXPERIMENT.....	155
8.1	THE CONE.....	157
8.2	IMAGE HANDLING.....	159
8.2.1	Inverse Filtering.....	160
8.2.2	Boundary Detection.....	162
8.3	RESULTS.....	166
8.3.1	SP-Algorithm.....	167
8.3.2	MLSE-Algorithm.....	170
8.4	CRITICAL COMPARISON.....	172
9	THREE-DIMENSIONAL HEART RECONSTRUCTION.....	174
9.1	DIFFICULTIES AND APPROXIMATIONS IN DATA ACQUISITION.....	175
9.2	IMAGE HANDLING.....	178
9.2.1	Filtering.....	179
9.2.2	Heart Motion.....	182
9.2.3	Boundary Detection.....	184
9.2.4	Modifications in the Reconstruction Algorithms.....	188
9.3	RECONSTRUCTION OF A HEALTHY HEART.....	190
9.3.1	SP-Algorithm.....	192
9.3.2	MLSE-Algorithm.....	193
9.3.3	Comparison-Conclusions.....	194
9.4	RECONSTRUCTION OF A DEFECTIVE HEART.....	196
9.4.1	Image Handling and Boundary Detection.....	198
9.4.2	SP-algorithm.....	199
9.4.3	MLSE-algorithm.....	200
9.4.4	Comparison-Conclusions.....	201
10	DISCUSSION.....	204
10.1	CRITICAL REVIEW-CONCLUSIONS.....	205
10.2	CLINICAL IMPLEMENTATION.....	215
10.3	FUTURE WORK.....	221

Appendix I.....	223
Appendix II.....	228
Appendix III.....	230
References.....	236

LIST OF ILLUSTRATIONS.

List of Illustrations

2.1. $P(u,\theta)$ is the projection of a 2-dimensional object $g(x,y)$ at angle $\theta+90$.

3.1. External view of the heart.

3.2. Internal view of the heart.

3.3. Two-dimensional display of Left-Ventricular boundaries at end-diastole and end-systole cardiac cycle states.

4.1. Typical images of the heart using Tl-201.

4.2. Gamma-11 system schematic diagram.

4.3. Anger camera schematic diagram.

4.4. Multiple-Static-Study file.

4.5. Schematic diagram of the PDP-11/10 computer system.

LIST OF ILLUSTRATIONS.

4.6. Demonstration of overprinting routine on Left Lateral view of the heart.

5.1. Image formation principle.

5.2. The two-dimensional projected image $g(Y,Z)$ of the three-dimensional object $f(m,n,l)$ emitting gamma ray photons.

5.3. Poisson distribution curves.

5.4. Anger camera resolution variation with distance from collimator.

5.5. Attenuation of photons in water.

5.6. Block diagram of the image formation process.

6.1. The emitted images of two-adjacent parallel slices overlap.

6.2. Plot of the one-dimensional point spread function.

6.3. Gated Image.

LIST OF ILLUSTRATIONS.

- 7.1. A slice of the cone is considered to be divided into unit volume pixels.
- 7.2. The process of image formation by projection.
- 7.3. Calculation of distances travelled by a photon in different media before reaching the projection line.
- 7.4. Flowchart of the Fractional Areas algorithm.
- 7.5. Flowchart of the SP-algorithm.
- 7.6. Flowchart of the MLSE-algorithm.

- 8.1. Conical cavity in cylindrical perspex block.
- 8.2. The cone phantom.
- 8.3. Cone phantom scintigrams.
- 8.4. Flowchart of the inverse filtering routine.
- 8.5(a). Filtered cone images.

LIST OF ILLUSTRATIONS.

8.5(b). Diagram indicating triangular shape of projection at the boundary.

8.6. Flowchart of the Boundary Detection method.

8.7-8.10. Cone reconstructions using the SP-algorithm.

8.11-8.14. Cone reconstructions using the MLSE-algorithm.

9.1. Healthy heart images.

9.2. Inverse Filtering working on healthy heart images.

9.3. Smoothed healthy-heart images, with 3-point smoothing.

9.4. 'Smooth-Inverse' filtered healthy heart images.

9.5. Anterior view of heart 'Smooth-Inverse' filtered with 5-point smoothing.

9.6(a). Parabola as used for Boundary Detection algorithm.

9.6(b). Calculation of the intensity of an off-grid point.

LIST OF ILLUSTRATIONS.

- 9.6(c). Parabola superimposed on healthy heart images.
- 9.6(d). Flowchart of the Boundary Detection algorithm.
- 9.7. SP-reconstruction, no attenuation correction.
- 9.8. SP-reconstruction, attenuation eliminated.
- 9.9. MLSE-reconstruction, no attenuation correction.
- 9.10. MLSE-reconstruction, attenuation eliminated.
- 9.11. Original defective heart images.
- 9.12. Heart images contained in 32x32 frame matrices.
- 9.13. Parabola tracing edges of defective heart images.
- 9.14. SP-reconstruction, no attenuation correction.
- 9.15. SP-reconstruction, attenuation eliminated.
- 9.16. MLSE-reconstruction, no attenuation correction.

LIST OF ILLUSTRATIONS.

9.17. MLSE-reconstruction, attenuation eliminated.

9.18. Typical slice through Left Ventricle.

10.1. Reconstruction Package.

I(a). PDP-11 diagram.



List of Tables

Table I. Storage and Execution times for Reconstruction Package,
page 220.

LIST OF ABBREVIATIONS.

List of Abbreviations

ACA: Attenuation Coefficient in Air.
ACP: Attenuation Coefficient in Perspex glass.
ACW: Attenuation Coefficient in Water.
ADC: Analogue to Digital Converter.
ANT: Anterior view.
+ATT: Attenuation eliminated.
-ATT: No Attenuation correction.
CPU: Central Processing Unit.
CVDU: Colour Visual Display Unit.
CRT: Cathode Ray Tube.
ECG: Electrocardiographic Gating.
ECT: Emission Computed Tomography.
EI: Emission Imagery.
EIS: Emission Imagery System.
FFT: Fast Fourier Transform.
FT: Fourier Transform.
FWHM: Full Width at Half Maximum.
IDS: Image Detecting System.
IFFT: Inverse FFT.
IFS: Image Formation System.
I/O: Input/Output.
LA: Left Atrium.
LAO: Left Anterior Oblique view.
LL: Left Lateral view.
LV: Left Ventricle.

LIST OF ABBREVIATIONS.

MID: Middle view.
MLSE: Minimum Least Squares Estimate.
MTF: Modulation Transfer Function.
ODT: On-line Debugging Technique.
PIP: Peripheral Interchange Program.
PSF: Point Spread Function.
+PSF: Image corrected for Point Spread Function.
-PSF: No elimination for image PSF.
RA: Right Atrium.
RV: Right Ventricle.
SNR: Signal to Noise Ratio.
SP: Straight Pseudoinverse.
SVD: Singular Value Decomposition.
TCT: Transmission Computed Tomography.
TI: Transmission Imagery.
TK: Tektronix.
VDU: Visual Display Unit.

ACKNOWLEDGEMENT

Acknowledgements

This research has been performed in collaboration with the Department of Nuclear Medicine at Guys Hospital, London. The cooperation and advice of [REDACTED], director of the department, of [REDACTED] principal physicist in the department and of [REDACTED] is gratefully acknowledged. The encouragement of Professor L. Finkelstein, Professor of Instrumentation and Control Engineering at the City University who directed this research generally, is sincerely appreciated.

The assistance of Mr. L. Norton-Wayne in supervising and coordinating the progress of this project is gratefully acknowledged.

Finally, gratitude is expressed to my colleague [REDACTED] for collaboration in common areas of research interest and [REDACTED] for assistance in the preparation of the illustrations.

ABSTRACT

The intention of this thesis is to examine the problematic nature of Emission Imagery (EI) in its application to medicine, analyse and provide solutions to the inherent processes of EI that degrade valuable information carried by the emitted gamma-photons, study the problem of the reconstruction of a three-dimensional (3-D) object from its emitted 2-D images, and develop digital processing methods, which determine the 3-D distribution of gamma emitting radionuclides in the human heart from a small number of projected gamma images. The objective is to map areas of heart muscle which have ceased to function, due to failure of blood supply following a coronary infarction, and thus provide the cardiologist with valuable information concerning the location and extent of cardiac infarcts in the myocardium.

Patient-examination involved injecting the patient intravenously with ^{201}Tl -Thallium, which accumulates in regions of the heart muscle which are active but not in those which are defunct. The 3-D distribution of the gamma ray emissivity, and hence the heart muscle activity, was then reconstructed from three 2-D gamma images, collected by an Anger camera at different angles around the patient chest wall.

Attention was concentrated on the Left Ventricle (LV) of the myocardium, where most of the infarcts occur. A 2-D filter, based on the 'inverse-filter' principle, was used to remove the imaging system point spread function from the images and a boundary detection technique to detect the image-boundaries and correlate the images. Two-algorithms, the Straight Pseudoinverse (SP) and the Minimum Least Square Estimate (MLSE) were employed to reconstruct the radioisotope distribution in the LV. Both algorithms provided significant compensation for attenuation, scattering, and Poisson noise. Image processing and reconstruction algorithms were first validated on a phantom consisting of a thick walled hollow cone filled with a solution of the radioisotope and a non-emitting rubber wedge to simulate cardiac infarcts. Then, successful reconstructions of healthy and infarcted hearts were obtained by both algorithms revealing the location and extent of infarcts with an estimated 15 min. computer processing time employing the SP-algorithm.

1 INTRODUCTION

The discovery of penetrating radiations (x-rays, gamma-rays) provided a means for viewing objects originally inaccessible to optical systems. Image formation by penetrating radiation is different from image formation by optical systems because the penetrating nature of the radiation and its extremely short wavelength eliminates the diffraction phenomena associated with optical systems. Consequently, new image detectors and recorders had to be developed (e.g. the Anger camera), since conventional lenses and photographic films used for optical systems were unsuitable for the formation of the penetrating radiation images. The resulting imagery was of great significance to science and found a wide range of applications in different scientific disciplines like astrophysics, electron microscopy, and radiology. Lately, the concept of penetrating radiations has been adopted in medicine to assist in diagnosis, research, and therapy. Internal organs of the human body (heart, brain, liver etc.) could now be imaged safely and their malfunctions evaluated atraumatically. However, such images suffer from the drawback that they constitute two-dimensional shadow projections of three-dimensional objects, highly distorted by the statistical limitations of the penetrating radiations. Consequently, much effort was placed on retrieving good quality images and extracting useful information from these images. This resulted in the rapid development of sophisticated imaging equipment, the manufacture of suitable radiation emitting substances, the use of computers for the analysis of pictorial data, and the advancement of

Chapter 1

computer-aided image processing techniques. Inevitably, a new branch of medicine was established, Nuclear Medicine, accounting for a large number of Nuclear Medicine Departments in highly industrialised countries.

The impact of computers in nuclear medicine was immense because the machine tends to carry out tasks similar to those performed by trained human observers. Additionally, the computer is fast, accurate, can handle large amounts of pictorial data and extract useful information reliably, without fatigue or boredom which degrade human performance significantly. Consequently, much emphasis was placed on the use of computers in processing, evaluation and classification of pictorial data, which assisted greatly in fast and accurate diagnosis and facilitated routine patient examination.

Penetrating radiation imaging systems are divided into two distinct categories, according to the nature of the radiation and the image formation process. Emission Imagery (EI) systems, where images are formed by the emission of penetrating radiation from a radioisotope substance (e.g. ^{201}Tl -Thallium) distributed in the object and Transmission Imagery (TI) systems, where images are formed by the transmission of penetrating radiation (e.g. X-rays) through the object. In EI the object and the source coincide and EI-images are functions of the radioisotope distribution and the attenuating medium that exists between the source, the body edge, and the detector, while in TI the source and the object are different and TI-images are functions of the distribution of the attenuating medium in the object.

Chapter 1

Thus, EI-images provide useful information concerning the radioisotope distribution in the object but this information is distorted by the attenuating medium, while TI-images provide information on the density of matter within the object which attenuates the penetrating radiation. This difference is depicted in the different applications for which each kind of Imagery is used in medicine.

TI gives major emphasis on the anatomic description of internal human organs, thus tissue density is important. It is also used to determine blood flow rates through the organ by providing useful information on the changes that occur in radiopaque contrast material inserted in the blood. Thus, TI can be used to study the relationships between anatomic structure and physiologic function of the different organs and determine the mechanisms of the disease processes which affect their structure or function. Examples of clinical applications include investigations in cardiovascular disabilities, abnormalities of vascular anatomies, circulatory dynamics in any region of the body, dynamic changes in shape and dimensions of the lungs, and tumor detection.

EI places emphasis on the quantitative determination of physiological and biochemical processes in the body. These processes are quantified by injecting radioactive chemicals or radioactive elements, which concentrate in specific organs (heart, brain etc.) or are important for life processes (aminoacid and fat metabolism), and detecting their distribution during radioactive decay. Applications of EI in clinical diagnostic medicine include determination of areas of

Chapter 1

tissue where there has been a significant decrease in blood flow (myocardial infarcts), investigation of brain and heart metabolism, detection of pulmonary embolism, cerebral aneurism, and methods of cancer detection.

The difference in the objectives and nature of each kind of Imagery has led to differences in the mathematical and instrumentation methods employed for image detection and processing. Two branches of nuclear medicine were thus developed based on the TI and EI, which progressed independently but with continuous cooperation and strong links. TI-technology progressed immensely mainly because of the better images it provided and the efficiency of the image detecting equipment. EI-images are characterised by poor statistics because each single photon must be analysed by a pulse height selector individually (see chapter 4) in contrast to the TI-images where the integrated output of the phototube over a short time period is sufficient for measurements. Additionally, in EI photon attenuation limits the number of photons reaching the detector considerably (only 50% of ^{201}Tl can be transmitted through 5cm of human tissue) thus requiring long imaging periods. However, the necessity of EI in clinical medicine emanated from its effectiveness in dealing with medical applications that TI could not handle effectively. As a result much effort has been put lately to developing machinery and methods for more drastic application of EI in Nuclear Medicine.

Chapter 1

Initially, research concentrated on extracting valuable diagnostic information by improving the quality of the images and performing statistical calculations locally to evaluate defects or malfunctions. Soon, different workers realised that there were serious limitations in the amount of diagnostic information that could be obtained, because images constituted two-dimensional projections of three-dimensional objects and thus most valuable information was 'compressed' in the images in a manner that rendered its extraction impossible. The concept of 'reconstructing the internal structure of an object from its two-dimensional projected images collected at various external positions around the object and thus revealing valuable information about the anatomical structure of the object' had been a subject of investigation in Mathematics and Radioastronomy for about fifty years, but it was first applied in the field of nuclear medicine in 1963 by Kuhl and Edwards[34]. This concept assumed major importance in 1973 by the development of the EMI-Scanner[35], a highly sophisticated computerised x-ray scanning system capable of reconstructing cross sectional images (tomograms) of the human head. The development of the ACTA-Scanner[36], an x-ray computerised axial tomographic system, followed shortly afterwards capable of reconstructing every part of the human body. Transmission Computed Tomography (TCT) progressed fast in contrast to the Emission Computed Tomography (ECT), which has lagged far behind mainly due to specialised problems encountered concerning instrumentation, inadequate spatial resolution of images, lengthy imaging procedures and cumbersome mathematical manipulations. The simplest data collection method, but the most cumbersome, involves an Anger gamma camera interfaced to a minicomputer that rotates around the

Chapter 1

patient collecting images of particular organs of the human body. Different tomographic methods[2] (most of them borrowed from TCT and adequately modified to compensate for attenuation) can then be used to reconstruct slices of the particular object. However, clinical implementation of the above procedure is inapplicable, since most tomographic algorithms require a large number of images which proves too time consuming for routine patient examination.

Several of the problems encountered in ECT have been partly solved by the design of expensive sophisticated systems, which use the Anger camera on a rotating mechanical structure that is capable of 360 degree rotation around the patient and a minicomputer system that records data and reconstructs slices. Such systems are the Homogotron[22] and the Searle[20] single photon system that are designed to reconstruct slices through the brain. Both consume about 30 mins for image collection and approximately about 4 minutes of computing time for each of nine slices. Recently a very interesting system was designed [23] that reconstructs the human heart using a seven pinhole collimator for simultaneous data acquisition and an Anger camera.

ECT systems are inferior to TCT systems and further research is required if ECT's capabilities are to be ever exploited fully. The target is to provide the clinician a powerful diagnostic tool that combines accuracy, speed, and economy in purchase and maintainance. This work will consider this objective and will develop procedures that deal adequately with most of the problems of ECT concentrating on the reconstruction of the human heart.

Chapter 1

1.1 OBJECTIVE

There is a requirement in medicine for the non-invasive examination of the human heart and in particular for measurement of areas of heart muscle which have ceased operating following a cardiac infarction. X-ray transmission imagery is not suitable in quantitating infarcts since the attenuation of x-rays by muscle tissue is not altered significantly when the blood supply is removed. Thus gamma photon imagery must be used, in which the patient is injected with radioactive isotope ^{201}Tl -Thallium, which accumulates selectively in the heart muscle. This then becomes self-luminous by emitting low energy gamma rays. Regions deprived of their blood supply as a consequence of the infarction do not receive the isotope and thus appear 'dark' on the received images (gamma images).

Cardiac infarct quantification has to be seen in perspective of the EI's inherent complexity, machinery availability, and clinical requirements for routine patient examination. It is required to develop a procedure, which will use the available machinery at the Nuclear Medicine Department of Guy's Hospital (an Anger gamma camera interfaced to a PDP-11/40 minicomputer system) to obtain and record gamma images of the cardiac muscle and which will provide the clinician with valuable information concerning the exact location and extent of damage in the muscle tissue of the myocardium. The overall procedure of image recording and processing must be fast,

Chapter 1

which implies minimum number of gamma images and short computer processing time , inexpensive, in that purchase of new hardware (e.g. special collimators or floating point arithmetic) is not necessary, and easy to use, which means that the process of image recording must be similar to the one already in use at Guy's for routine patient examination. Any software must be compatible to the available PDP-11/40 system with minimum requirements for computer core and operator's intervention, and most important, the procedure must be accurate enough to improve drastically the cardiologist's diagnosis which is presently restricted to conventional two-dimensional procedures of image analysis.

Evidently, the author is presented with a complicated problem that introduces multiple constraints and limitations. Past experience has shown that complex problems can find solutions if a concrete theoretical background is established first that examines the problem in its generality. Next, the work of different researchers, who have dealt with similar problems, is examined to reveal the relationships between particular applications and theoretical background, and then any new ideas suitably linked with other workers innovations and in the light of the requirements, limitations, and constraints of the particular application, are carefully examined to reveal the optimum path to the solution of the problem.

Chapter 1

The objective of this thesis is accordingly:

1. A thorough examination of the nature of Emission Imagery and analysis of its particular properties and problems, so that representative mathematical formulations can be derived to describe the image formation process for subsequent computer simulation.
2. The development of signal processing and tomographic reconstruction algorithms that overcome the complicated problems inherent in EI, provide efficient solutions to the difficulties of the particular application, satisfy its constraints and limitations, fulfil the requirements set by the clinicians at Guy's, and retrieve accurately the radioisotope distribution in the myocardium.

Chapter 1

1.2 DIFFICULTIES

There are three types of difficulties arising in this particular application.

First, are the difficulties arising from the nature of the Emission Imagery. Gamma images are characterised by their low contrast, low resolution, and noisy nature. The removal of those degradations from the images is problematic, since most of them have to be somehow estimated or assessed. Another difficulty is the non-linearity of the imaging system, which complicates the mathematical formulations and thus the speed and efficiency of the computer simulation. It is necessary to investigate and if possible obtain an estimate of the degree of the system's non-linearity, lest there be a possibility of linear approximation.

Second, are those difficulties arising from the particular organ (heart) under investigation. Problems induced by the structure, shape, magnitude, and function of the heart seem difficult to overcome. For example, the living human heart performs a complicated movement during a cardiac cycle inducing serious image blurring, which is difficult to remove digitally from the images. Additionally, are those difficulties arising during the patient-examination. The patient has to remain still during the process of image recording (about 40 minutes), thus imaging time must be short to secure patient comfort.

Chapter 1

Third, there are difficulties arising from the requirements of this work. Difficult decisions have to be made in the choice of methods to balance the contradicting demands of obtaining accurate results with minimum amount of information (images), so that we safeguard against violations of the time and computer core constraints.

In the chapters to follow all these difficulties are analysed and find appropriate solutions.

Chapter 1

1.3 PROPOSED APPROACH

The analysis of the requirements of this application and the determination of the objectives of this research, as described in section 1.1, will form the guidelines in our attempt to search for an approach that will tackle efficiently the problem of quantitating cardiac infarcts.

Cardiac images will be obtained by an Anger camera fitted with a multichannel parallel hole collimator. The camera will be situated at a particular position close to the chest wall for continuous imaging of the myocardium until a certain number of events have been detected. Then the camera will be rotated to a new position around the chest wall to obtain a different cardiac view. Images will be digitized and stored as 64X64 or 128X128 square matrices. A small number of images will thus be recorded and digital methods will be employed for further processing.

This research is mainly concerned with the development of suitable digital image processing techniques, which will extract from the images valuable information concerning the structural layout of the functional sections of the myocardium and determine the location and extent of the non-functional tissue (i.e. infarcts). The approach proposed for tackling the problem is the following:

Chapter 1

First, the nonlinear image formation process will be analysed and a representative linear mathematical model will be formulated to describe the process with good approximation. This is a necessary step taken to avoid complicated formulations and time consuming computations.

Second, suitable algorithms will be developed to improve the quality of the highly degraded images, as the first measure to making the information carried by the images more accessible. The linear formulation of the image formation process indicates the employment of linear filters, which are easy to implement, in correcting for the point spread function of the imaging system. In addition, one of the fundamental assumptions of any tomographic algorithm is that images are formed by parallel non-overlapping rays, but the presence of interactions such as scattering gives the system an imperfect point spread function. This must be removed as far as possible, prior to any reconstruction.

Third, a boundary detection algorithm will be developed to trace the boundary outline of the projected image of the LV (the chamber of the myocardium where most of our attention will concentrate) within the overall recorded gamma image. The LV-images will be correlated and segmented in consecutive parallel regions, which represent the projected gamma images of consecutive parallel slices through the LV. Correlated segments selected from each image will be stacked together to be used by the tomographic algorithm. The effectiveness of the boundary detection algorithm is directly

Chapter 1

related to the contrast of the gamma images. This is an additional reason for removing the imaging system's point spread function, by digitally filtering the images prior to any image manipulating procedure.

Fourth, an image reconstruction method will be chosen, which requires the least amount of information (gamma images) and reconstructs consecutive slices of the LV with speed and accuracy. Such method should not employ Fourier techniques, since a large number of images is required, or iterative techniques, since they are time consuming. As is explained in later chapters, the reconstruction method adopted for this work is based on generalised matrix techniques. It requires a minimum of three images, the computations involved are drastically reduced by suitable exploitation of the anatomic structure of the myocardium, and it is very effective in compensating for photon attenuation and Poisson noise image degradations. Two versions of this technique will be examined in this work. Both have not found medical applications before.

Fifth, the reconstructions of consecutive slices of the LV, the Left Ventricle, will be stack together and displayed on a Tektronix screen. The anatomic structure of the Left Ventricle (thick walled hollow object) facilitates the deployment of its walls onto a flat surface. Thus the display of consecutive, stack-together, reconstructed slices will provide a picture of the radioisotope distribution in the walls of the Left Ventricle, where the location

Chapter 1

and extent of infarcts will be visually apparent.

The validation of the methods and algorithms will be first accomplished in a simulated environment. A phantom consisting of a thick walled hollow cone will be constructed from perspex glass (this object resembles the Left Ventricle). The walls of the cone will be filled with a solution of the radioisotope and a rubber wedge will be inserted at a known position to simulate infarcts. Image collection and processing will be accomplished as described above.

The algorithms will be then adjusted to deal with real heart images. First, the algorithms will be tested on healthy hearts to investigate if any artifacts result owing their existence to factors other than infarcts. Next, the algorithms will be used on infarcted heart images to determine their ability in reconstructing the radioisotope distribution in the muscle-tissue of the Left Ventricle and exhibiting with clarity the location and extent of infarcts.

2 CRITICAL SURVEY OF APPLICABLE IMAGE PROCESSING METHODS

The use of radiopharmaceuticals in examining the internal structure of different organs in the human body has initiated the development of sophisticated equipment for image acquisition and supporting image processing techniques in the attempt to improve the diagnosis of organ irregularities by non-invasive means. The target is to develop atraumatic methods for patient examination which cause minimum discomfort, provide adequate information regarding organ defects (tumors, lesions, etc.), and assist the cardiologist to improve his diagnostic capability.

The development of the Scintillation Camera in 1957 by Hal O. Anger[41] and the design of efficient collimators[18] provided a means for imaging the internal organs of the human body (heart, liver, brain, lungs, etc.). Parallel development of radioisotopes like Potassium, Rubidium, Caesium, and Thallium[18,13,42] that concentrate well on the myocardial muscle tissue or Technetium[18] in the liver, lungs, brain, assisted greatly in the non-destructive examination of patients.

Emitted gamma rays carry useful information that is difficult to evaluate or extract because the images are highly degraded by Poisson noise, photon scattering, and attenuation phenomena.

Chapter 2

Most attention, therefore, was concentrated in extracting this information, which resulted in the development of highly sophisticated image processing techniques and of ingenious machinery that assisted and speeded up the 'examination-diagnosis' procedure. Filtering techniques, that deconvolve the image from the system's point spread function, and boundary detection techniques, that extract the region of interest from the background radiation, were developed or adopted from other disciplines and suitably modified to suit the nature of the highly distorted images.

Further insight into the composition of the internal human organs was gained by the development of ingenious software methods, which reconstruct slices of the three dimensional radioisotope distribution of the organ from several of its two-dimensional gamma images projected in different directions. This reconstruction is generally called Tomography. Living tissue defects could be now located and evaluated, thus increasing the diagnostic ability of the cardiologist. Emission Computed Tomography (ECT) has found wide application in Nuclear Medicine. Several ECT systems employing the Anger Camera with sophisticated hardware and supporting software have been developed lately[20,22,23]], which although they produce valuable reconstructions, are expensive in purchase and maintainance.

The purpose of this chapter is to examine different image processing methods within the perspective of the objectives, limitations, and constraints of this research project. Our objective is not to provide a detailed description of all image processing and

Chapter 2

reconstruction methods applicable in ECT, since this would require enormous space, but to describe certain existing methods, closely linked with our objective, and investigate the usefulness of their probable adoption in satisfying the objectives of this work. Within this framework several filtering methods will be described first, then an account of several boundary detection routines will be given, and finally several reconstruction algorithms will be described. This procedure will enable us to develop a critical review of applicable image processing methods, useful in justifying the adoption of certain methods for this work.

Chapter 2

2.1 FILTERING

Gamma images are two-dimensional projections of three-dimensional objects (e.g. the heart) stored as square discrete matrices by the image formation system (e.g. the GAMMA-11 system). These images are highly distorted by the point spread function of the gamma camera, the Poisson noise effect, and the photon scattering and attenuation phenomena. Additionally, in the present application gamma images are distorted by the continuous complicated movement of the heart and the spontaneous movement of the patient.

Elimination or partial removal of those image degradations from the images has puzzled many workers, who in their attempt to improve image contrast or visualisation of fine detail, have adopted, after suitable modification, image processing techniques developed for optical deblurring.

The search for suitable filters in the 'infinite' field of filters can only be optimised if a guideline is suitably designed by the objectives, limitations, constraints of this work and the nature of the imaging system.

Chapter 2

Filters can be divided into two main categories, Linear filters and Nonlinear filters, depending on whether they are designed to deal with degradations caused by linear or nonlinear image formation systems. It is known that the gamma camera image formation system is nonlinear, but as is shown in later chapters, its nonlinearity is 'mild' and the system can be considered approximately linear. The loss of accuracy, in considering the system linear and using linear filters, is adequately compensated by economising in computation. Nonlinear deblurring methods, in their majority, are difficult to implement, since for large samples require excessive computations. This, however, has not deterred several workers from developing, with relative success, non-linear filtering techniques[9,27,43,54], for medical applications.

Linear filters are easy to implement and this has tempted many workers to use them for deblurring images [55-56]. These filters, however, require knowledge of a priori information, concerning the system's point spread function and noise, which for any particular camera operated under specified conditions are difficult to determine. Image restoration can be performed in the Fourier domain by deconvolving the system's PSF from the image. This is possible because the PSF of the Anger camera is to a good approximation (see chapter 5) invariant. Many workers have attempted to restore images developing filters based on the 'Wiener-filter' principle, which is somewhat more powerful provided the nature of the source is known. Lately, Boardman[28] has adopted the Constraint Optimisation filter due to Hunt[37] and has applied

Chapter 2

it successfully on scintigraphic images of the brain. A very interesting filter was developed by Mead et al.[32] for cardiac images, in which the operator, through the interactive facility of the computer, designs in the frequency domain the system's PSF, which is then deconvolved from the image and transformed back to the spatial domain revealing high quality restored cardiac images.

Most of the above mentioned filters, however, are not applicable in this work, since some require much a priori information (like noise power spectra) and others large computer core or time consuming 'operator's-interact'. In the attempt to search for a linear filter to satisfy the constraints and fulfil the requirements of this work, four basic linear filters are summarised below, from which one will be chosen on its merits, structural simplicity, and efficiency. Restoration is performed in the Fourier domain and image transformations from the spatial to the frequency domains and inversely are performed by the Fast Fourier Transform (FFT) and the Inverse FFT respectively (see chapter 6). Detailed descriptions of these filters are given in[11,12,27].

Let the discrete form of the image formation process in the frequency domain (see chapter 6 for explanation) be represented by:

$$G(u,v)=H(u,v)F(u,v)+N(u,v), \quad u,v=1,2,\dots,N \quad 2.1$$

where:

$G(u,v)$: is the blurred image

$H(u,v)$: is the Modulation Transfer Function (the FT of the PSF)

Chapter 2

$N(u,v)$: is the Noise, considered additive

$F(u,v)$: is the original image

The objective is to recover $F(u,v)$ or a close estimate $F'(u,v)$ of $F(u,v)$.

1. Inverse Filter

This is the simplest approach to image deblurring, requiring the least a priori information (knowledge of the imaging system PSF). The Inverse filter [11,17] is derived from equation 2.1, by dividing both sides of 2.1 by the MTF:

$$\frac{G(u,v)}{H(u,v)} = F(u,v) + \frac{N(u,v)}{H(u,v)} \quad 2.2$$

from 2.2

$$F(u,v) = \frac{G(u,v)}{H(u,v)} - \frac{N(u,v)}{H(u,v)} \quad 2.3$$

If the quotient $N(u,v)/H(u,v)$ is considered small then 2.3 reduces to:

$$F'(u,v) = \frac{G(u,v)}{H(u,v)} \quad 2.4$$

This expression gives an estimate $F'(u,v)$ of the original image $F(u,v)$ providing the point spread function of the imaging system is known.

Chapter 2

There are two basic problems which are usually encountered in the practical application of the above filter. The first, is that noise is always present and the second, is the occurrence of zeroes in the MTF term $H(u,v)$. Therefore, for some values of u and v the quotient $N(u,v)/H(u,v)$ is not usually negligible and $F'(u,v)$ in some cases does not approximate $F(u,v)$. This is evident under ill-conditioned circumstances, where by the magnitude of $H(u,v)$ drops to zero with distance from the origin of the $u-v$ plane more rapidly than the magnitude of $N(u,v)$, thus the quotient $N(u,v)/H(u,v)$ is drastically magnified at high frequencies and noise is predominant in the resulting image.

2. Wiener Filter (or Minimum Mean Square Error [MMSE] filter)

The sensitivity of the Inverse filter to noise and ill-conditioning is avoided by the MMSE-filter, which minimises the statistical expectation of the square of the difference, in the spatial domain, between the original image $f(x,y)$ and the estimate $f'(x,y)$:

$$\text{Minimise: } E((f(x,y) - f'(x,y))^2) \quad 2.5$$

The derivation of the estimator is described in [11] and the filter in the frequency domain has the following expression:

$$F'(u,v) = \frac{H^*(u,v)}{H(u,v)^2 + \frac{S_n(u,v)}{S_f(u,v)}} \cdot G(u,v) \quad 2.6$$

Chapter 2

where, $H'(u,v)$ is the complex conjugate of $H(u,v)$, and S_n and S_f are the power spectra of the noise and signal respectively. In the absence of noise $S_n=0$ and 2.6 reduces to the Inverse filter. Thus, in the low frequencies of the image, where noise is low, the Wiener filter behaves similarly to the Inverse filter. In the high frequencies, where the signal is usually small, it is evident from 2.6 that the gain of the Wiener filter becomes small. Thus, the image distortion due to ill-conditioning is tackled adequately.

3. Homomorphic filter

In this filter a linear estimate $f'(x,y)=L(g(x,y))$ is sought for which the power spectra of the estimate and the original signal are equal, i.e.

$$S_f = S_{f'} \quad 2.7$$

and from 2.1

$$S_{f'} = L(u,v)^2 (H(u,v)^2 \cdot S_f(u,v) + S_n(u,v)) \quad 2.8$$

and from 2.7 solving for $L(u,v)$

$$|L(u,v)| = \left[\frac{1}{H(u,v)^2 + \frac{S_n(u,v)}{S_f(u,v)}} \right]^{\frac{1}{2}} \quad 2.9$$

Thus,

$$F'(u,v) = \frac{1}{\left[H(u,v)^2 + \frac{S_n(u,v)}{S_f(u,v)} \right]^{\frac{1}{2}}} \cdot G(u,v) \quad 2.10$$

It can be observed from 2.10 that for $S_n \rightarrow 0$ the filter reduces to the Inverse filter and for $S_f \rightarrow 0$ the filter gain tends to zero. Elsewhere, the filter gain is greater than the Wiener gain and smaller than the Inverse filter gain, as it can be observed from equations 2.4, 2.6, 2.10. Thus the Homomorphic filter has the properties of the Wiener filter and provides deblurred images having more structural detail associated with high frequencies, due to its larger gain.

4. Constrained Optimisation Filter

The main shortcoming of the Wiener and Homomorphic filters is the requirement for knowledge of the power spectra S_n and S_f , which in many situations is difficult to obtain. The Constraint Optimisation filter, devised by Hunt[37], provides a deblurred estimate of the degraded image, requiring knowledge of the system's PSF and the noise variance alone, and assumes that the intensity variation across the original image is smooth, a valid assumption for gamma images.

Chapter 2

In this filter a linear estimate $F'(u,v)$ is sought for which the residual $(G-HF')$ has the same average properties (i.e, standard deviation) as N . In particular the residual must satisfy:

$$\sum_{u=1}^N \sum_{v=1}^N ((G(u,v)-H(u,v) \cdot F'(u,v)) \cdot (G(u,v)-H(u,v) \cdot F'(u,v))^*) = e \quad 2.11$$

where e is a known constant, function of the noise standard deviation, and $*$ is the complex conjugate symbol.

However, there may exist a number of estimates F' that satisfy equation 2.11, thus an additional constraint is employed to produce the optimum solution. This constraint, frequently called the smoothness criterion, is the minimisation of a function, which describes the intensity variation across the image. In the fourier domain the smoothness criterion is expressed as:

$$\text{Minimise: } \left(\sum_{u=1}^N \sum_{v=1}^N (C(u,v) \cdot F'(u,v)) \cdot (C(u,v) \cdot F'(u,v))^* \right) \quad 2.12$$

where, $C(u,v)$ is the Fourier Transform of a second difference operation, such as the Laplacian operator.

The restoration problem is then to find F' of 2.1 which minimises 2.12 subject to the constraint 2.11. The solution is found by employing Langrangian multipliers[28,37].

$$F'(u,v) = \frac{H^*(u,v) \cdot G(u,v)}{H(u,v) \cdot H^*(u,v) + \gamma \cdot C(u,v) \cdot C^*(u,v)} \quad 2.13$$

$\gamma = 1/\lambda$, where λ is the Lagrangian multiplier.

Chapter 2

where, γ is a parameter which is determined iteratively so that equation 2.11 is satisfied. This filter requires the least a priori information of either the Wiener or Homomorphic filters and provides an optimum restoration for the image to be restored. On the other hand, the Constrained Optimisation filter requires large core and time consuming iterations for the restoration of each image.

The choice of a particular filtering method to restore the gamma images of the heart can be now seen as the best compromise between the advantages and disadvantages of each filter and the demands and constraints imposed by this application. A restoration method is required which is simple in its structure and implementation, requires the least a priori information and operator's interact, demands low computer core and processing time, can be successfully and equally applied without alterations to all cardiac gamma images of each study and of any study, and provides good quality of restored images. The Wiener and Homomorphic filters require knowledge of a priori information which is not readily available, while the Constrained Optimisation filter is time consuming and core demanding. The Inverse filtering method seems to be the best compromise in satisfying the constraints of this application provided that it can improve the quality of the gamma images. The latter can be achieved only if the signal to noise ratio is large and ill-conditioning is not severe. The Inverse filtering method was finally adopted and a filter was designed which provided good quality of restored images.

2.2 BOUNDARY DETECTION

The problem of extracting the image of an object from an irrelevant background in a picture is termed segmentation and is one of the most difficult tasks in image processing. The effectiveness of a technique in extracting digitally the object from its background depends directly on the quality of the overall image at hand and the nature of the object that is imaged. Consequently, the problem of 'object-extraction' has no unique solution, but on the contrary found numerous solutions for different applications.

The large variety of techniques proposed for 'object-extraction' can be divided in four basic categories[10,11]:

1. Thresholding, where the image of the object is separated from the image of the background by setting the grey level values of the overall image below a threshold grey level equal to zero.
2. Edge Detection, where the object is extracted from the rest of the image by the detection of the regions of discontinuity (edges), i.e the regions of the image where there is an abrupt change in grey level. Such edges indicate the end of one region and the beginning of another.
3. Matching, where the search is directed towards locating points in the image that follow a given pattern of grey levels. The pattern can be an edge or the boundary line of a known object.

Chapter 2

4. Tracking, where the outline of an object is traced by accepting new points, which fulfil certain criteria and depend on the nature and location of the points already accepted as part of the object's outline.

'Object-extraction' in medical images is generally considered a difficult task but gamma images of the heart, in particular, present additional problems due to their noisy-low contrast nature and the blurring caused by photon-scattering and the continuous movement of the heart. As a result, there have been only a limited number of approaches proposed by several workers. Most attention has been concentrated on X-ray images, because of their superior quality, and several successful 'object-extraction' techniques have been proposed. However, the examples set in TI (Transmission Imagery) must be taken under consideration, since this is the way that EI (Emission Imagery) has progressed, i.e exploiting the achievements of TI. Therefore, this section will provide indicative examples of successful 'object-extraction' techniques both in TI and EI.

In order to isolate the image of the heart within the overall gamma image, where background and other organs (e.g, the liver) may be visible, we need only determine the boundary line of the cardiac image. We are looking, therefore, for a method to trace the boundary edges of the heart or a 'boundary-detection' technique.

Chapter 2

Chow and Kaneko[38] have developed an impressive method of detecting the boundary of the Left Ventricle in X-ray cardiac images using an ingenious thresholding technique. Their fundamental assumption was that the probability distribution of the intensity of any small region of the picture, consisting solely of the object or the background, is unimodal and that in a small region containing a boundary there exist two unimodal distributions, one for the object (Left Ventricle) and one for the background. The LV-image is brighter than the background-image, thus the histogram for any region of the image that contains a boundary will exhibit two peaks, one for the LV and one for the background, and a valley, where generally the two distributions overlap. A local threshold can be thus determined at the valley point, which separates the LV from the background. In this manner, Chow and Kaneko developed an algorithm which divides the entire picture into a set of small overlapping regions, calculates the local histograms, determines the regions exhibiting bi-modal distributions and computes their local thresholds, calculates local thresholds for the remaining regions interpolating from the 'boundary-regional'-thresholds, performs a binary decision for each image point, and finally employs an edge-following algorithm on the binary image to select the boundary silhouette of the Left Ventricle.

An alternative boundary detection method, combining the principles of Edge Detection and Tracking, was developed by Herman and Liu[39] for x-ray images. This algorithm utilises the following properties of a boundary point: (a) high contrast (b) connectivity

Chapter 2

of boundary points and (c) agreement with a priori knowledge. The routine requires a starting boundary point, which is provided interactively, and chooses the next boundary point from the neighbouring points (principle of connectivity) that has the maximum gradient value (high contrast principle) among those not already on the boundary, provided that the current gradient value is larger than a threshold value, which is proportional to the average gradient value along the boundary found so far. If a new boundary point cannot be determined, then the algorithm returns to the previous boundary point (backtracking), flags the path between the previous and current boundary points so that the algorithm does not enter the same path, and searches for a new track. The algorithm ends when a termination criterion is satisfied. This technique has been applied successfully on x-ray cardiac images.

Kuwahara et al[40] give account of a boundary detection technique which was applied on cardiac gamma images. This algorithm requires a starting point, which it considers as an estimate, and determines the actual initial boundary point by determining the 'best orientation' from the local maximum gradient value and searching along the direction of the best orientation by means of an edge-detector to locate the actual boundary point. Then the algorithm moves to a point near the detected boundary point in a direction perpendicular to the 'best orientation' and takes this point as the new 'estimated boundary point', from where the procedure repeats itself.

Chapter 2

P.Varoutas et al[9] give account of another boundary detection technique which was used to detect the LV-boundary in cardiac gamma images. According to this method the images are transformed into binary matrices by setting all values above a threshold equal to one and the rest equal to zero. For each point its nearest six neighbours, arranged in a rhombic pattern, are examined and certain combinations of ones and zeroes are chosen to indicate that the current point is a boundary point.

The above boundary detection techniques indicate the attempt of several workers to locate the LV-boundary employing different or a combination of 'object-extraction' principles. Others [38] require complicated statistical operations and large computer core while others[9] are oversimplified to be included in the present work. In this work, alternative boundary detection techniques were developed, utilising a priori information and minimum operator's interact, which proved adequate for the satisfaction of the time and core constraints and were efficient in their application. Additionally, the technique developed for detecting the LV-boundaries is applicable for any cardiac gamma image.

2.3 METHODS FOR TOMOGRAPHIC RECONSTRUCTION

The problem of reconstructing a two-dimensional object from a number of its one-dimensional projections was first studied by J. Radon in 1917. He produced a transformation which describes the projection process by mapping the object function $g(x,y)$ into the projection function $p(u,\theta)$ [51], given here in polar coordinates:

$$p(u,\theta) = \int_{-\infty}^{\infty} g(u.\cos\theta - v.\sin\theta, u.\sin\theta + v.\cos\theta).dv \quad 2.14$$

where, $p(u,\theta)$: is the projection at an angle $\theta+90$.

$x=ucos\theta-usin\theta$ and $y=usin\theta+ucos\theta$

θ : is the angle of projection.

u,v : are the rotated coordinates (see figure 2.1)

The reconstruction problem is thus based on the development of different techniques for solving 2.14, by recovering $g(x,y)$ given a number of one-dimensional projections around the two-dimensional object. In the same work Radon developed the theoretical background for inverting 2.14 and produced an inversion formula, the convolution reconstruction formula, whose principle is presented below.

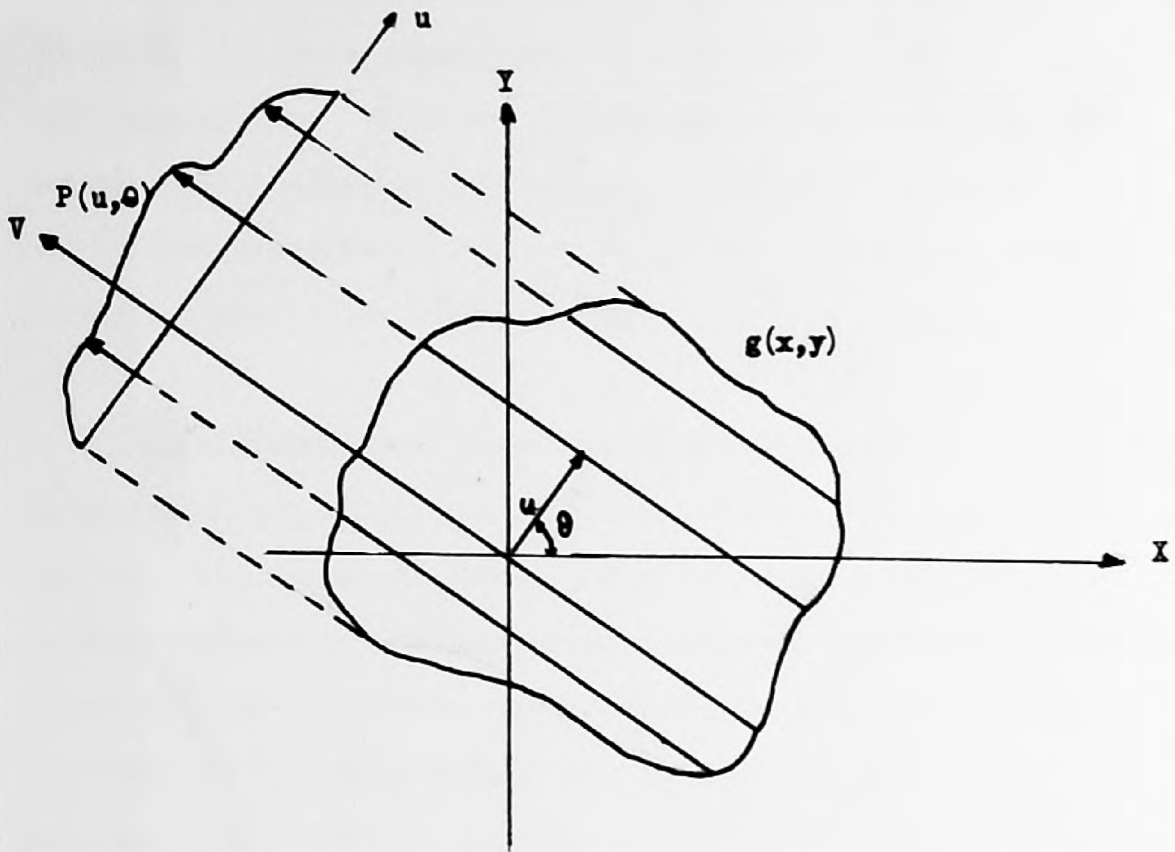


Figure 2.1

$P(u, \theta)$ is the projection of a
 2-dimensional object
 $g(x, y)$ at angle $\theta + 90$

Chapter 2

Radon's work provided the tools for examining the interior structure of three-dimensional objects and found numerous applications in different scientific disciplines, like radioastronomy, electron microscopy, biology etc. Lately, his work was adopted in medicine for examining the structure of the different internal organs of the human body.

Several methods have been devised for reconstruction of the three dimensional distribution of radioisotope within an object from multiple two-dimensional views. For the sake of simplicity, the reconstruction of a two-dimensional object from its one-dimensional views will be considered in this section. A recent survey is provided in [2]. These methods fall into four main categories, as follows:

- (i) Fourier Techniques.
- (ii) Convolution, or Filtered Back Projection Techniques.
- (iii) Iterative Estimation Techniques.
- (iv) Direct Matrix Techniques.

The Fourier technique is based on the projection slice theorem which states, [19], that the Fourier transform of the projection of a two-dimensional pattern $f(x,y)$ at an angle θ to the x axis is equivalent to the radial line slice of the Fourier transform $F(u,v)$ of the pattern, at an angle θ with the u axis. If therefore a sufficiently large number of projections of $f(x,y)$ are taken at

Chapter 2

different angles θ , then the Fourier domain description of the pattern can be constructed, $F(u,v)$, and the spatial domain description $f(x,y)$ then obtained from this by inverse Fourier transformation.

The Convolution or Filtered Back Projection technique reconstructs a two-dimensional pattern $g(x,y)$, by back-projecting a filtered version of the projections formed by $f(x,y)$. In [19] it is proved that the reconstructed image is:

$$g(x,y) = \int_0^{\pi} q(u,\theta) d\theta \quad 2.15$$

where,

$q(u,\theta)$: is the filtered version of the projection at angle $\theta+90$,

and:

$$q(u,\theta) = \tilde{f}^{-1}(|\omega| P(\omega,\theta))$$

where, \tilde{f}^{-1} is the Inverse FT symbol, and $P(\omega,\theta)$ is the FT of the projection $p(u,\theta)$.

Chapter 2

The Iterative Estimation (or algebraic reconstruction) technique involves guessing the distribution $f(x,y)$ then modifying this guess iteratively until the projections measured and those computed on the basis of the assumed distribution are sufficiently in agreement.

Finally, the Direct Matrix technique assumes the distribution to comprise a rectangular grid of cells, whose projection at any angle is obtained merely by summing intensities in the line of view. Thus, projected views and distribution are connected by a set of linear equations. Provided a sufficient number of projections is available, the distribution can be obtained by solving these equations, i.e. inverting a weighting matrix and multiplying this onto vectors representing observations.

The first three reconstruction techniques have been widely used to reconstruct different parts of the human body, often with notable success, [1-6],[19-23]. Several workers have compared these methods in reconstructing the same object, [2], and evaluated their respective merits and shortcomings. However, the methods are in general tedious and expensive computationally.

Recently systems have been devised employing several gamma cameras to view the heart simultaneously. These produce a good reconstruction but require expensive special purpose equipment which is difficult to set up, [20-23].

Chapter 2

In the past, direct matrix inversion seems to have been of little use as a reconstruction technique[2,7] in tomography, probably because of the excessive computation which is required, which makes the approach impractical on the small computers used routinely in medical diagnosis. Further the system of equations involved in the reconstruction is generally singular. However in the present application we are reconstructing a hollow object whose shape is known approximately. This reduces the processing and storage required considerably, rendering the approach viable. Only a small number of projected images is required. It takes about ten minutes for the Anger camera to record a good two-dimensional image of the heart, thus methods requiring many projected views for reconstruction would be unacceptable. In fact the method we have developed produces a series of tomographic reconstructions of consecutive slices, with great speed and accuracy.

Chapter 3

3 PROBLEM DEFINITION

The objective of this work is to develop image processing and reconstruction techniques, which will prove effective in reconstructing the radioisotope distribution in the myocardium of the heart with accuracy and clarity, and will facilitate the location of non-functional myocardium muscle tissues or lesions resulting from a heart attack. In view of this objective, the object under consideration (heart) has to be examined closely, so that a better understanding of its function, structure, and possible malfunctions can be obtained. This will assist us in developing a mathematical model for the heart, which will make possible the computer simulation of the processes involved in the projection, formation and degradation of the gamma images. The functional formulation of the image formation process will then assist us in deriving methods, which 'reverse' the image formation process and thus recover the three-dimensional radioisotope distribution from its two-dimensional projected images.

Mathematical models usually constitute approximate configurations of reality. As it is often the case, the better the approximation the more complicated the mathematical formulation of the model becomes. It is apparent, therefore, that in searching for a mathematical model of the heart, a compromise has to be made between approximation and simplicity in functional formulation. This compromise has also to be seen within the perspective of the requirements and constraints of this work.

Chapter 3

It seems necessary, therefore, that the conception of a mathematical model of the heart is first realised in structure, to test the validity of the image processing and reconstruction methods. In this way, results can be obtained, which are not influenced by approximations made between mathematical model and heart, but indicate the ability of the algorithms to reconstruct correctly. Verification of the validity of the algorithms will then allow the application of these methods to reconstruct the heart, attributing any discrepancies to the model approximations made.

The purpose of this chapter is to derive such a mathematical model for the heart, suggest its structural realisation, and point out its similarities and differences from the living human heart.

3.1 HEART CHAMBER DESCRIPTION AND OPERATION

The heart of an adult person has approximately the shape and size of the person's two fists fitted together, so that the knuckles of one hand are against the knuckles of the other hand and the two wrists are touching[44].

The normal weight of the heart is approximately half of one percent, or a little less, of the total body weight. The bigger the person the bigger the heart, thus there is a variation in the size and weight of the heart amongst humans. Figure 3.1 shows the external view of the heart and Figure 3.2 shows the internal structure of the heart. Basically, the heart consists of four chambers, Left and Right Atria (LA,RA) and Left and Right Ventricles (LV,RV), of four valves, and of veins and arteries, which allow blood to be pumped in and out of the heart.

The innermost lining of the heart wall is called the Endocardium. It is a strong layer of fibrous and endothelium over which the blood runs smoothly. The endocardium also coats the four heart valves. There are two valves in the right side of the heart and two in the left side of the heart. In the right side the triscupid valve separates the RA from the RV and the pulmonary valve separates the RV from the pulmonary artery. In the left side of the heart the mitral valve separates the LV from the aorta. These valves open and close during a cardiac cycle regulating the flow of

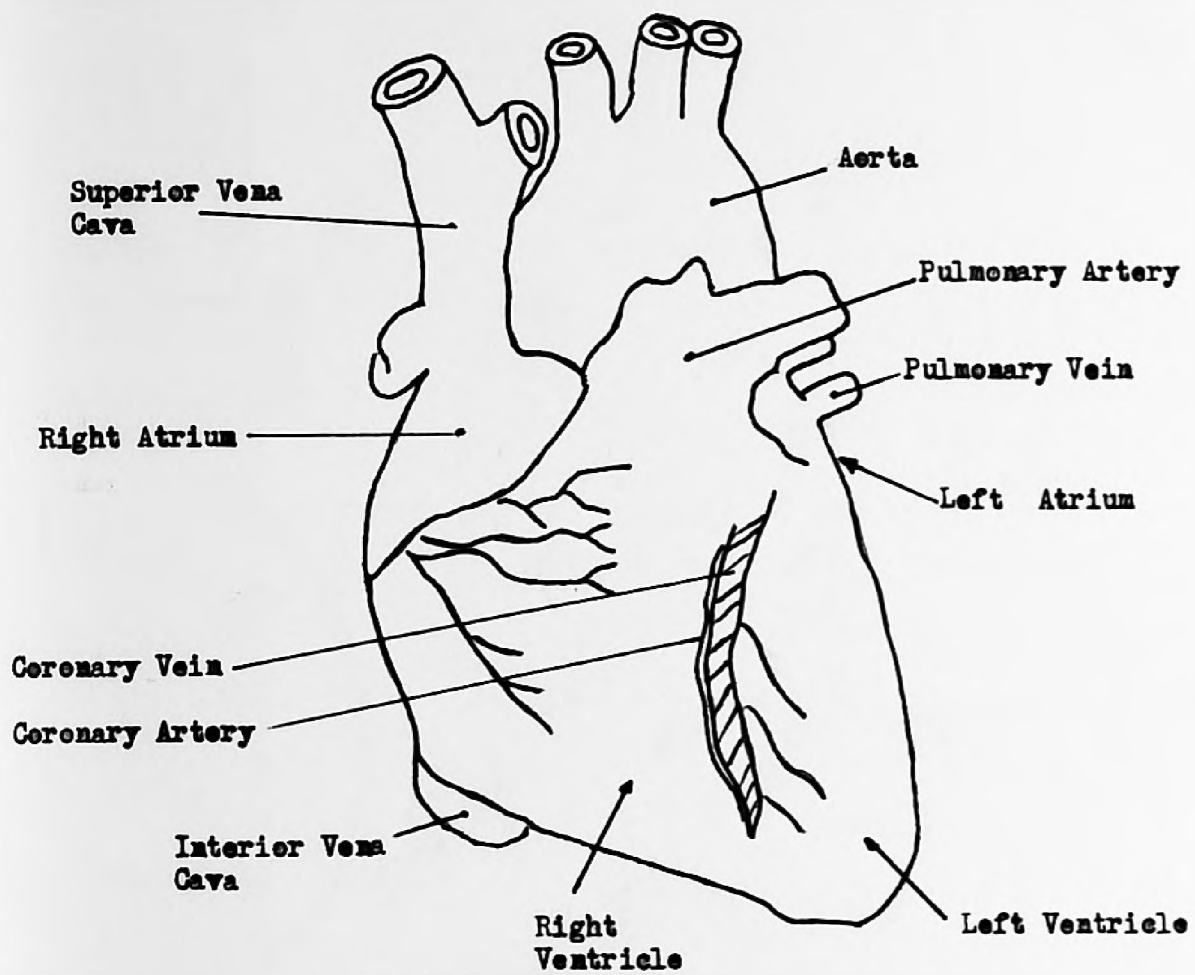


Figure 3.1

EXTERNAL VIEW OF THE HEART

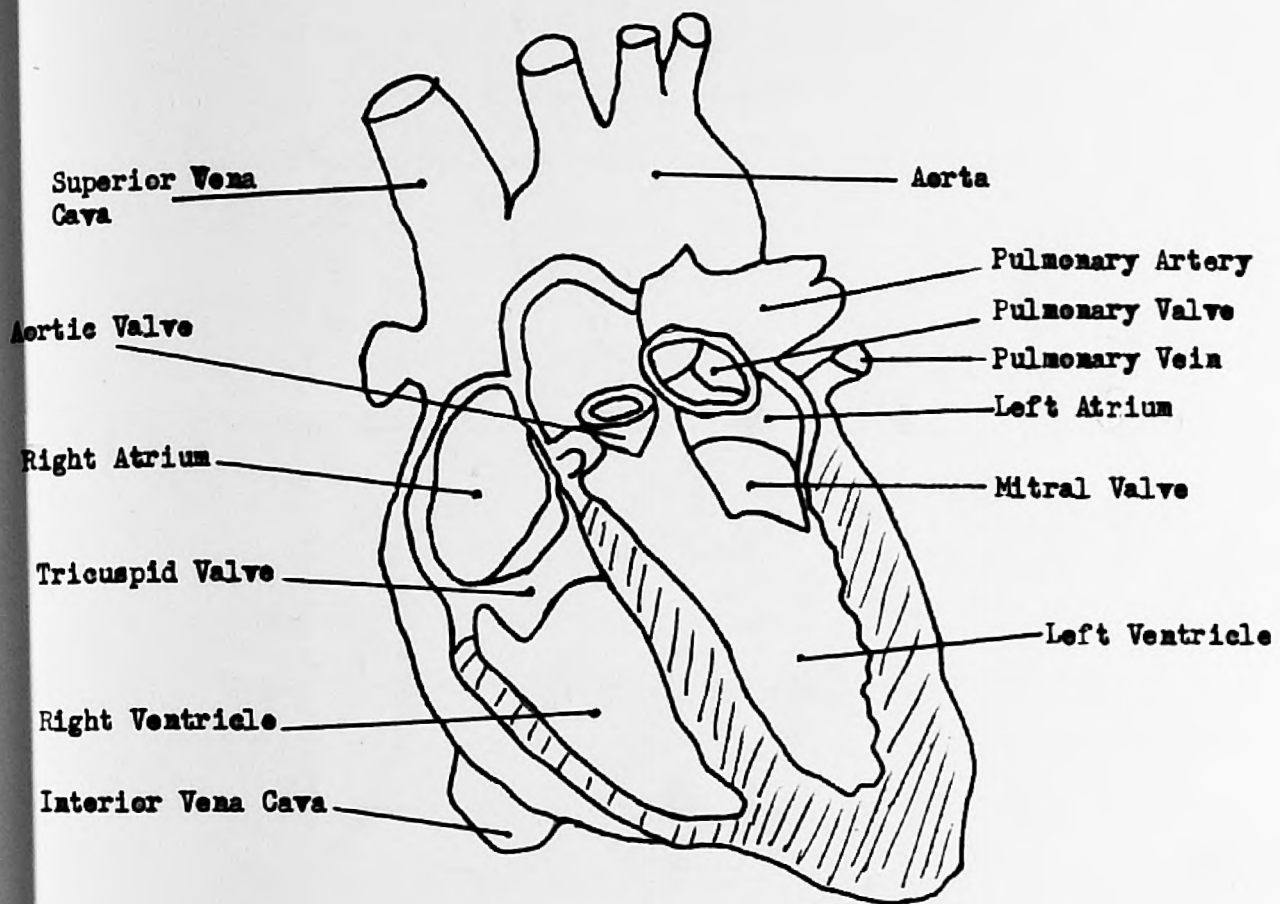


Figure 3.2

INTERNAL VIEW OF HUMAN HEART

Chapter 3

blood in a certain direction.

The middle layer of the heart wall is called the Myocardium. It is made up of thick heart muscle arranged in more or less concentric layers. The wall thickness of the LV is approximately 1cm while the RV wall thickness is about 0.3cm. The ventricles differ in muscle mass with the LV weighing approximately twice the RV.

The outer layer of the heart is called the Pericardium and it forms a sac in which the heart lies.

The heart beats on its own by means of a natural pacemaker situated at the superior vena cava. This is a large vein carrying blood to the heart from the upper parts of the body and it is technically known as the sinoatrial node. Every second an electrical impulse of 1/10 millivolts travels down over the two atria causing the atrial muscle to contract. The impulse proceeds to the so called atrioventricular node of Tawara. This node sparks the electrical stimulus causing both ventricles to contract.

The path that the blood flows in the heart chamber is the following: While the atria and the ventricles are relaxed blood enters the RA from the vena cavae and the LA from the pulmonary veins. When the two atria contract, the blood supply is forced into the ventricles. The walls of the ventricles are still relaxed. After the ventricles are filled they start to contract. The

Chapter 3

triscupid and mitral valves snap shut and the pulmonary and aortic valves start to open. As the ventricles contract further, blood from the LV is forced into the aorta and blood from the RV is forced into the pulmonary artery.

Normal heart rates are about 60-72 beats per minute. Under stress or exercise the heart rate may reach 170-180 beats per minute. An athlete's heart at rest may beat as low as 45 b/min.

3.2 CORONARY HEART DISEASE

The term 'heart attack' signifies the acute failure of the pumping action of the heart. Most heart attacks are attributed to the heart disorder called coronary thrombosis. In this disorder, the coronary arteries are blocked by the accumulation of fat and fibrous tissue cells, thus the supply of blood and oxygen to the heart muscle is obstructed. Blood clotting in one of the coronary arteries may cause the destruction of the muscle segment, which the artery supplies with blood, reducing the efficiency of the heart. Dead muscle tissue in the heart muscle is usually called an 'infarct' or 'lesion'.

Such a heart attack may cause immediate death or according to its severity the patient may live for a week, a month, a year, or he may recover completely to live an ordinary life.

There are two different approaches for treating patients with myocardial infarction, depending on the severity of the damage done on the muscle tissue. Infarcted areas can be reduced by either administering chemicals in the body of the patient or by surgical intervention. Obviously, early diagnosis of the extent of damaged muscle is important to ensure appropriate treatment. Thus, the need arises to develop methods for non-invasively quantitating the volume of the infarcted muscle tissue in the myocardium. This is achieved by administering radioisotopes to the patient, which concentrate

Chapter 3

well in the healthy areas of the myocardium, and examining the images that are projected. This is where this research concentrates, that is to improve the diagnosis of lesions given the gamma images of the heart.

3.3 MODELLING THE HEART

The need to seek for a mathematical formulation of the heart arises from the nature of the objective of this work, i.e. the reconstruction of the radioisotope distribution in the myocardium from a number of projected gamma images. This objective can be reached if image formation processes are functionally formulated so that the 'reverse' process of reconstituting a three-dimensional object from its projected two-dimensional images can be suitably simulated in the computer. But the three-dimensional shape of the distribution, that is its geometric presentation in space, is functionally involved in the mathematical formulation of the object reconstitution process.

It could be argued that there is no need for seeking such a model for use in the reconstruction process, since the problem can still find a solution, as indeed is the case with many reconstruction algorithms, even if the radioisotope distribution in the functional formulations finds a general description. Such consideration, however, would increase considerably the number of

Chapter 3

gamma images required to achieve a reasonable reconstruction and the dimensionality of the matrices involved, thus rendering the reconstruction problem impossible for the limited core memory of the PDP-11 computer system. On the other hand, it was our belief that we could find a simple mathematical formulation for the myocardium together with the fact that a small number of gamma images were required that led us to adopt the particular reconstruction method, the Pseudoinverse, in that low computer memory was thus insured. Finally, it would be very difficult to eliminate the photon attenuation effect from the images (which was proved to be an important step for achieving correct reconstructions) without knowledge of the geometric distribution of the radioisotope.

Searching for a functional formulation for the shape of the heart, it will be always kept in mind that the target is to find a model which is simple, to avoid complicated calculations, and suitable, to secure a good degree of approximation to the real heart. Balancing simplicity with accuracy is a difficult task, since one increases at the expense of the other. Thus, further insight into the structure of the myocardium and image formation processes is needed.

First, the structure of the myocardium had to be closely examined. Several heart phantoms were studied, in collaboration with experts from Guy's Hospital, in the attempt to determine particular features of the heart's muscle structure. The reader may be assisted by examining the structural model of Figure 3.2. Two

Chapter 3

remarkable observations, which will form the back-bone of this chapters contribution, were made: First, the left ventricle is the largest and most massive chamber of the myocardium and second the LV-wall seems, to a good accuracy, symmetric about an axis, which from now on will be called, the axis of symmetry of the LV.

Next, if it is assumed that the radioisotope distributes evenly in the myocardium, which is true, then most of the radioisotope residing in the myocardium must be concentrated in the most massive chamber of the heart, the Left Ventricle. Indeed, this is the case and it can be easily verified by examining the images that a radioisotope administered heart projects in different directions in space. Some typical images are shown in Figure 9.1 or Figure 9.4, where the images projected from the myocardium consist mainly of the image of the LV with no visual evidence of the RV. Facts, therefore, show that the attention of this work should concentrate on the most massive part of the myocardium, the LV, which is the most evident part of the heart in the images, despite the contributions that the RV may induce in the images. The above conclusion was also reassured by Guy's, for most infarcts occur in the LV and especially in the area close to the apex of the LV. Additionally, most image processing work, which is done at Guy's for quantitating the volume of the infarcted tissue, concentrates on the LV-wall.

Chapter 3

The above considerations suggest that the problem of deriving a mathematical model for the myocardium can be simplified to deriving a mathematical model for the left ventricle of the heart. Thus attention is immediately concentrated on the shape of the LV-wall and any considerations made will be assisted by the drawing of Figure 3.3, which shows the two-dimensional display of the LV-borders as they would have been shaped on a Tk-screen configuration of an end-diastolic (systolic) image. The continuous line shows the LV-boundary at end-diastole and the dashed line shows the LV-boundaries at end-systole. As hinted before, the area of interest, where most infarcts occur, is close to the apex of the LV, thus we need only examine the area below the X-axis, about 2/3 of the total LV-chamber. Looking at the end-diastole boundary its egg-shaped presentation is evident and an axis of symmetry Y can be easily imagined. Examining a LV phantom, which was specially prepared at Guy's for the author, it is easily verified that there is indeed an axis of symmetry for the three-dimensional object. Concentrating in the area below the X-axis it is not difficult to observe that a PARABOLA would easily fit the the boundary line. Considering wall thickness of 1cm (infact thickness is variable) and noting that the LV chamber is hollow, a hollow, thick-walled, parabolic model with circular cross section would seem to provide a good approximation to the real shape of the heart, having at the same time a simple mathematical description.

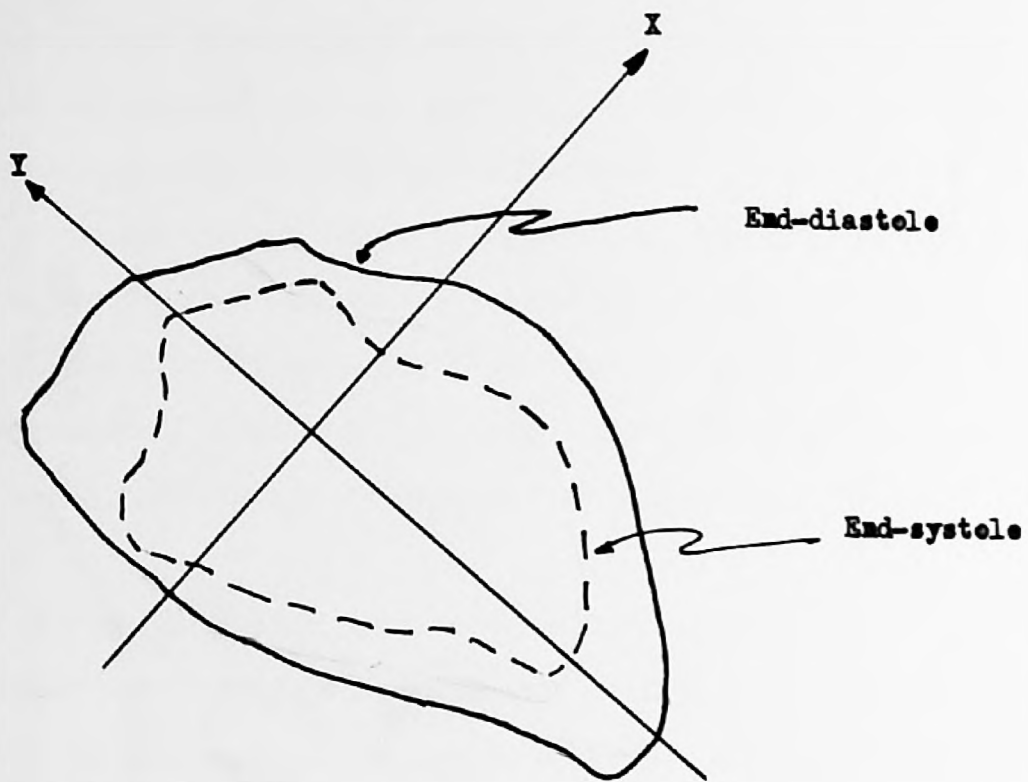


Figure 3.3

Two-dimensional display of Left-ventricular boundaries at end-diastole and end-systole cardiac cycle states.

Chapter 3

Such a model, however, was conceived by examining the shape of the end-diastolic boundary of the LV. It would be inefficient to use this model on real heart images, while developing the image processing and reconstruction algorithms, since the heart performs a continuous periodic complex movement of rotation and translation with subsequent displacement of its boundary, as indicated by the continuous and dashed lines of Figure 3.3. Thus the emitted gamma images are degraded by the motion, contributing further to the point spread function. Evidently, the end-diastolic parabolic model does not correspond accurately to such images and approximation errors are mostly undesirable in developing the software for this work.

The implementation of this model requires a thorough examination of the heart motion and its implications on the gamma images, as well as the existence of accurate image processing and reconstruction algorithms. Indeed, such a model was assumed and successfully used in chapter 9, but after multiple testing on heart images.

The need to develop and at the same time test the correctness of the algorithms, diverted us to search in the conventional solid objects for a simple representation, which would be easy to design and implement in the functional formulations of the image formation processes, but at the same time would bear a resemblance to the LV. We came up with the thick-walled, hollow cone, which could be easily constructed in the laboratory and conveniently find a mathematical expression. The cone was used to obtain images, which

Chapter 3

were then used to reconstruct the radioisotope distribution in the cone's walls. This procedure safeguarded the results against errors, which might have occurred due to approximations made between model and LV. Once the validity and efficiency of the image processing and reconstruction algorithms were verified, then the parabolic model was used to reconstruct the radioisotope distribution in the LV-walls from the heart images.

Chapter 3

3.4 DISCUSSION

This chapter has stressed the importance of using a mathematical model in the functional formulation of the image formation process, has indicated the methodology to be followed in retrieving the radioisotope distribution in the myocardium, has confined the area of interest to the left ventricle, and has suggested mathematical models to be used in developing the software of this work and attempting the reconstruction of the radioisotope distribution in the LV-wall.

But, how well do these models approximate to the real left ventricle, can a mathematical model which is designed for static imaging conditions be used to simulate dynamic image collection procedures (continuous movement of the heart during image recording), do all these considerations to obtain and implement a mathematical model really safeguard against any violation of the constraints imposed by this work?

Certainly, concrete answers cannot be given at this stage of the thesis, but we can attempt to analyse those questions, provide suggestions, and forecast the proximity between simulation and reality.

Chapter 3

Obviously, modelling the LV and developing the image processing and reconstruction algorithms are influenced by the objective of this work, which together with the available machinery induce limitations and constraints. The main intention of this research is its practical implementation in the Nuclear Medicine Laboratory for routine patient examination. Thus, it has to be fast, reliable, and demand little computer core memory. Our opinion is that those demands are adequately dealt with because, first the reconstruction method, that is the procedure which simulates the 'reversal' of the image formation process by referring the images back to the radioisotope distribution, that has been adopted requires a small number of images with consequent reduction in image recording time and computer memory, second the use of a priori information, that is the LV-model implementation in image processing functional formulations, results in further reduction in the number of gamma images necessary to achieving the reconstruction and increases the algorithms reliability, and third LV-model implementation and gamma image filtering provisions facilitate greatly the reconstruction of consecutive slices through the LV reducing drastically the computer core memory required by the reconstruction algorithm.

DESIGN IN CHAPTER 3

Slice-reconstruction cannot be treated locally, that is modelling the slices as thick-walled circles whose radii are extracted suitably from the images, but globally, in that slices are indeed modelled as thick-walled circles but related to each other as part of the LV-model. In that case, the dimensions of the LV-model have to be computed first to reveal the radii of the individual

Chapter 3

slices.

The calculation of the LV-model's dimensions is a two-fold procedure: using a priori information of the shape and approximate size of the LV and obtaining structural information from working interactively on the gamma images. This procedure insured, to a good approximation, that the LV-model attained realisable dimensions and secured the proximity of the model's size to that of the LV of the particular study. Considering that the size of the heart, and consequently the size of its gamma images, differs amongst humans, the above twofold procedure assisted greatly in the efficient and correct calculation of the LV-model's dimensions in different heart studies.

It is stressed, however, that there is a limit to how closely such a model could fit the actual LV structure, since structural information obtained from the images is distorted by the heart-motion effect. Additionally, LV muscle thickness varies around the walls of the left ventricle, while the LV-model assumes constant wall thickness. Both cases are analysed and suitably treated in Chapter 9.

The distinct difference between the cone reconstruction and the LV reconstruction is that in the cone experiment the mathematical formulation of the conical structure is exact, while the paraboloid used for the LV-model constitutes an approximation to the LV-structure. Consequently, better results are to be expected from

Chapter 3

the cone reconstruction than from the LV reconstruction.

As we progress to the following chapters, most of the questions posed at the beginning of this section will be examined extensively, and in view of the results that will be obtained later on, will find satisfactory answers.

4 DATA ACQUISITION AND DATA PROCESSING SYSTEMS

The purpose of this chapter is dual. First, to describe the methods, instruments, and computer system employed by the Nuclear Medicine Laboratory at Guy's Hospital in the collection and recording of the gamma images used in this work and second, to describe the Departmental computer laboratory, where specialised software was developed to process the gamma images and attempt the three-dimensional reconstruction of the heart. Fortunately, both laboratories have similar PDP-11 computer systems, PDP-11/40 and PDP-11/10 respectively, under the same RT-11 operating system, thus software compatibility was possible. Differences in peripheral devices (magnetic tapes or discs) between the two systems rendered the transformation of data problematic, since communication was only possible via paper tapes.

This chapter will not provide a detailed account of the design and construction of the different equipment and interfaces, since this is not the objective of this thesis, but it will highlight certain procedures or instruments, which play a major part in data acquisition and data processing, and will give the operational outline of others.

First, a description will be given of the procedure involved in the preparation of the patient for gamma camera scanning, second, the data acquisition system at Guy's will be described with particular reference to the gamma camera, computer system, and data recording, and finally an outline of the data processing system will be given with

Chapter 4

particular emphasis on the computer system.

Chapter 4

4.1 PATIENT EXAMINATION

Clinical examination of patients for the diagnosis of acute myocardial infarction using Thallium-201 scintigraphy is divided into three stages: Patient preparation, heart image recording, and image evaluation or diagnosis. This section will deal mainly with the first two stages, since they are employed in this work, and will additionally present an outline of the method used for Thallium-201 preparation.

The quality of myocardium images improves appreciably when they are recorded following patient exercise. Thus, a short intravenous catheter is connected to a syringe with 1.5mCi ^{201}Tl and is inserted in a vein of the forearm, with the syringe taped to the arm[42]. The patient is next subjected to exercises, probably on a gym-cycle, and the Thallium is injected one or two minutes before the end of the exercising period. Thallium accumulates in the various organs of the human body (heart, liver, stomach, kidney etc.) with about 4% of its total amount residing in the heart muscle.

After ten minutes from the end of the exercises, the patient is positioned in a bed, where the image collection process is initiated. The Anger camera is fitted with a low-energy, high resolution, parallel hole collimator, is positioned close to the chest wall, and four different views of the myocardium are

Chapter 4

collected. The projections used for patient examination are : the Anterior, 45 Left Anterior Oblique (45 LAO) and 55 LAO, with the patient resting on his back side, and the Left Lateral, with patient lying on his right side. Figure 4.1 shows typical projected views of the heart as described above.

The positioning of the camera is very critical since the heart images may include contributions from other organs (e.g. liver). It is common practice to restrict these contributions by placing a radiation absorbing frame over the chest wall, which only allows viewing of the area of interest (i.e. the heart). Each image requires about ten minutes of recording time, during which about 200,000 counts are registered.

Radioactive Thallium-201 is manufactured from non-radioactive Thallium in a cyclotron, by bombarding it with high energy protons. The result is the creation of radioactive lead isotopes which after separation decay back to thallium. Following a second purification process an end product is obtained with main constituent ^{201}Tl -the rest being ^{200}Tl and ^{202}Tl - which is then manufactured as a solution suitable for clinical applications.

Tl-200 and Tl-202 in the Thallium solution do not affect the quality of the images because they emit high energy photons. The low toxicity of the Tl -solution makes it popular for medical applications.

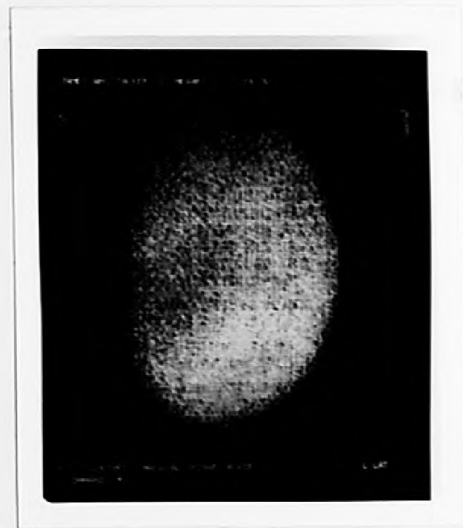
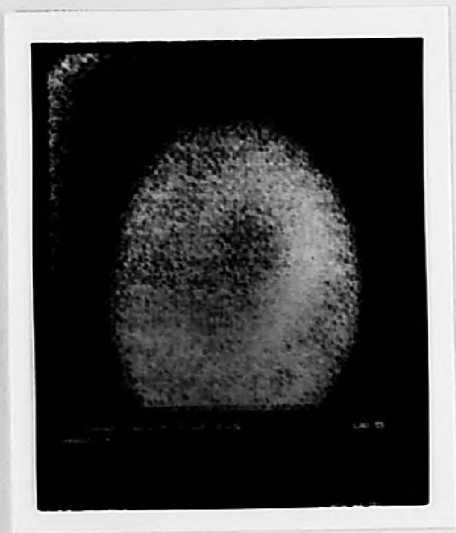
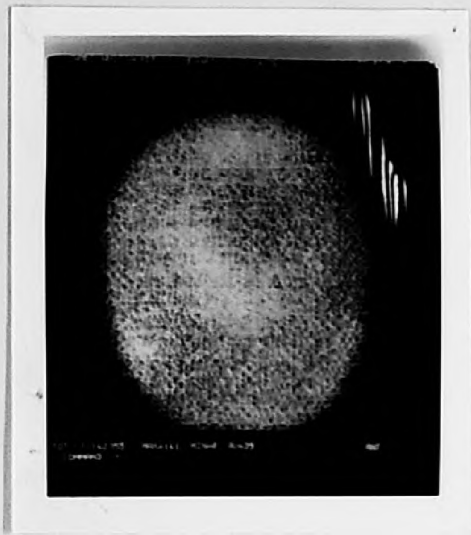


Figure 4.1
Typical images of the heart using Tl-201.

4.2 DATA ACQUISITION SYSTEM (GAMMA-11)

The data acquisition system used in the Nuclear Medicine Laboratory of Guy's Hospital is the GAMMA-11 system manufactured by D.E.C. It is a computer system, specifically designed for nuclear medicine applications, interfaced with a gamma camera. The gamma camera is used to obtain data on the distribution of a radionuclide in the human body, and for this particular application the camera is used to form images of the Thallium distribution in the myocardium of the human heart.

The GAMMA-11 system is used to collect the gamma images and to digitize, store, manipulate, and display them, thus constituting an efficient tool for the clinician in the diagnosis of myocardial lesions. The GAMMA-11 system is controlled by a PDP-11/40 minicomputer equipped with special software and interfaced to suitable peripherals to assist in the routine patient examination[49].

Figure 4.2 provides a schematic diagram of the GAMMA-11 system. The process of image formation and recording is as follows:

Thallium-201 radioisotope, distributed in the myocardium, emits gamma photons which on impact with the solid-sodium-iodide scintillation crystal (NaI) in the gamma camera produce scintillations, which are magnified by a hexagonal array of

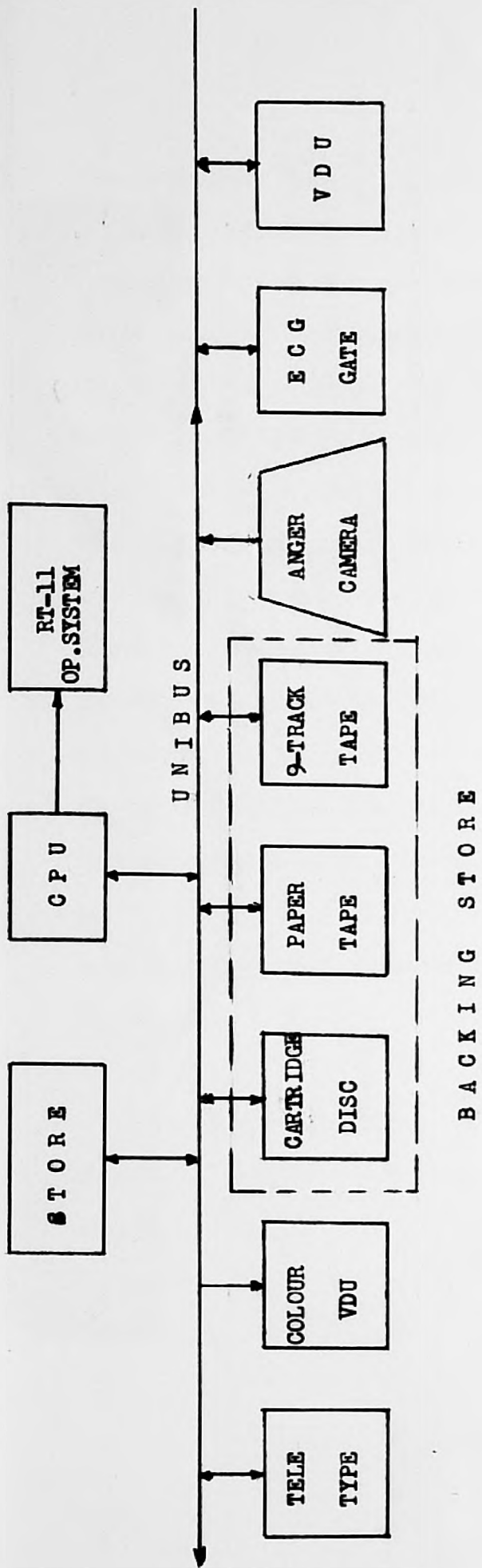


Figure 4.2
GAMMA - 11 SYSTEM Schematic Diagram.

Chapter 4

photomultiplier tubes. Electronic circuitry senses the position of the scintillations and produces three signals, two giving the X and Y coordinates of the position of the scintillation and a third Z proportional to the brightness of the scintillation. The signal at this stage is analogue and can be displayed on the visual display monitor of the camera as point flashes of light (see Figure 4.1). This provides the facility of an early estimation of the correctness of the received image before data recording commences. Next, the analogue-to-digital converter (A.D.C) of the gamma camera interface transforms the image information to digital form, which is stored on the cartridge disc peripheral. Images can now be read from store and plotted on the colour VDU by typing commands on the keyboard of the typewriter on the CRT-unit. The system incorporates magnetic tape storage and paper tape facility. ECG-gating is an optional facility which can be used to provide static (motion free) heart images, though this increases the time taken to record an image by a factor of 3.

Further details on the instrumentation, software, and image data file structure are documented on the relevant sections of this chapter.

4.2.1 Gamma Camera Detection System

The gamma camera detection system used in this application incorporated an OHIO NUCLEAR 100 series Anger camera fitted with a parallel multihole collimator. The basic structure of the gamma camera detection system is shown in Figure 4.3. The multichannel parallel hole collimator consists of a plate made of gamma ray absorbing material, usually lead, with numerous channels through it. Its purpose is to 'look' at the heart, excluding from the detector gamma photons travelling in some direction other than a straight line from the heart, and form the gamma ray image at the exit side of the collimator. The size of the image is independent of the distance of the heart from the collimator, but image resolution changes in inverse proportion with the distance of the heart from the entrance side of the collimator. The resolution and sensitivity of the collimator also depend on its structure, that is, on the number, size, and length of the holes, and on the thickness of septa between the holes. They are also related to the energy of the emitted gamma photons. All these factors determine the geometric construction of the collimator, which for the particular application collimator thickness of 2.6mm will discard 95% of the unwanted radiation, which is incident in a non-parallel direction, and will allow the transmission of only one in 10,000 photons for Tl-201 or 99m-Tc.

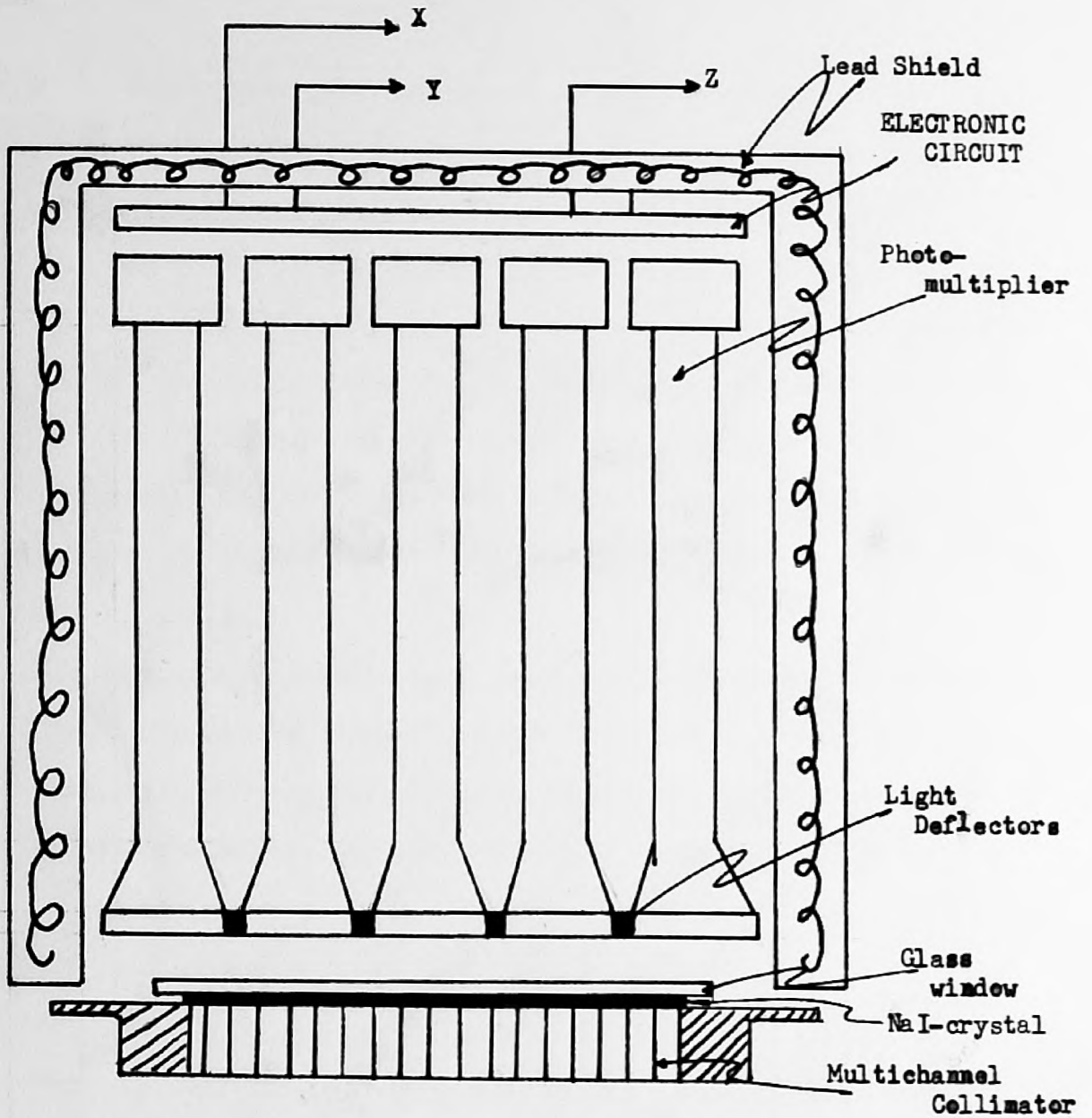


Figure 4.3
 Anger Camera - Schematic Diagram.

Chapter 4

Those gamma photons, which manage to pass through the collimator, impinge on the scintillator, which is made of solid sodium iodide crystal contained in a hermetically sealed can with a glass window and aluminium oxide reflector. On impact with the crystal, a fraction of the gamma photon energy is transferred into a secondary electron, which in turn produces a flash of visible light in proportion to its energy. Again the efficiency and resolution of the scintillator are related to the thickness of its crystal and the energy of the gamma photons.

The optical light guide provides a high-refractive-index path between the crystal and the photomultipliers and the light deflector reflects the light that falls between the tubes. Both provisions secure passage of light to the phototubes directly above its occurrence, thus improving the resolution and linearity of the images.

On exit from the photomultiplier tubes the electronic circuitry provides the X and Y positioning signals and the Z amplitude signal, which is proportional to the brightness of the scintillation. The Z signal is previously applied to the input of a single-channel pulse-height selector, which is adjusted to accept the photopeak of the gamma ray spectrum[13], thus eliminating scattered photons and other background radiation.

Chapter 4

Finally, the overall detection system is housed in lead as shown in Figure 4.3.

Thus the gamma camera detection system -collimator and Anger camera-, which constitutes the best available imaging instrument in emission imagery for internal organ radioisotope examination, is suitably designed to improve image definition and provide realisable images. However, despite the advance of camera technology in recent years, the resulting images are distorted. Poor resolution is still a major problem and is partly due to the gamma camera detecting system. Its overall image resolution is the resultant of the resolution of the image produced at the exit of the collimator and the image produced at the end of the photomultiplier tubes. Same considerations are applicable for the system's sensitivity too. The loss of image clarity is due to several factors which include: geometric structure and material composition of the detecting system, photon scattering in the different stages of the system, statistical variations in the distribution of photons amongst the phototubes largely due to the statistical variation in the number of photoelectrons produced by a single scintillation, discrimination ability of pulse selector, background radiation due to stray gamma rays, and distance of subject from the collimator. All those sources of distortion can be combined in a function, which finds a mathematical formulation and is referred to as the gamma camera point spread function (see chapter 5).

Chapter 4

In the present application, an additional source of image distortion results from the movement of the heart. Heart images are severely distorted, a fact that led many researchers to devising techniques to freeze the heart in the images. A hardware implementation, which is the most popular in Nuclear Medicine, is to use electrocardiographic gating (ECG) to synchronise the camera (see Figure 4.2) to the cardiac cycle. Thus image recording is performed during a particular time interval of the cardiac cycle (e.g. end diastole). This is an ingenious method[33], that improves the clarity of the gamma images immensely. Such an image can be seen in Figure 6.3(a) and its superiority is established immediately from comparing it with the images of Figure 9.1. It is disadvantageous, however, in that it is time consuming and thus not convenient for routine patient examination. For this reason it still comprises a provisional facility in the Nuclear Medicine departments.

4.2.2 GAMMA-11 Computer System

The GAMMA-11 computer system consists of hardware and software components. The hardware comprises the machinery and interfaces and Software comprises the various computer programs, which establish communication between operator and machinery, and specific programs for nuclear medicine applications.

Chapter 4

(i) There are five categories of Hardware

The PDP-11/40 central processing unit (CPU), which performs all calculations and controls all operations of the computer system.

The computer memory or core, which holds data being processed by the central processor.

The communication peripherals or input-output peripherals, which enable communication between operator and central processor.

The backing stores, which are mass storage peripherals on which data are stored on a long term basis.

The interface hardware, which connect peripherals to the central processor.

The PDP-11 central processor's basic function is to perform all arithmetic and logical operations and communicate with the peripherals. The CPU uses the computer memory to store the programming instructions and image matrix data. This storage facility is temporary and it is used while program execution and data manipulation take place. More specific description of the PDP-11 CPU and computer memory are given in Appendix{I}.

The communications peripherals are devices which enable the operator to transfer information to the CPU, by typing commands on an input device, and the CPU to communicate with the operator via an output device. Some peripherals incorporate both input

Chapter 4

and output facilities (I/O). The following communication peripherals are used in the GAMMA-11 computer system:

Input/output device, in that it provides

The LA30 DEC-writer has a key-board on which the operator types commands to the CPU and the computer responds by printing back on the DEC-writer's paper the result of the requested operation (e.g. patient's study file). The computer's response can be also directed to other terminals, depending on the operator's request. The DEC-writer is an I/O dot matrix printer, with printing speed 30 characters per second.

The colour video display unit (CVDU) is capable of

The colour video display unit (CVDU) is capable of displaying the gamma images in 16 different intensity levels, which describe the intensity variations within the image. Each of the 16 different intensity levels is either represented by a distinct colour (in fact there are 64 different colours, but only 16 colours can appear on the screen of the CVDU at a time) or by a distinct shade of grey for black and white configurations. The colour display terminal is an output device used only for displaying gamma images.

Specification 11. This unit is used for

The Cathode Ray Tube (CRT) is functionally similar to the DEC-writer only that all communication between operator and computer appears on the CRT's screen. Again it is an I/O device which can only display text.

Input/output device, in that it provides

device, this is the only device used for

Chapter 4

The backing store or mass storage peripherals are cartridge discs, magnetic tapes, and paper tapes. Each one is an input/output device, in that it transfers data images to the CPU and receives data images from the CPU. They are utilised to increase the storage capacity of the computer memory and to store data for long periods.

Cartridge discs are the most convenient means of storing data and communicating with the CPU. Data are stored magnetically on the disc in eight-bit bytes. Two bytes constitute one word and 256 words one block. One cartridge disc is capable of storing over 1.2 million words. Each image data file comprises a set of blocks and each disc contains a directory with all the data files and their location on the disc. The disc directory is created by the software of the computer system and facilitates the random access of the files. The cartridge disc peripheral is a mass storage disc drive and control device, which contains a fixed system disc, with the operating-system software, and a removable user's disc with data files and user's programs. Overall it is a fast and efficient mass storage device with data transfer speed specification 11.1usec/word and track positioning time 50msec.

Magnetic tapes are used for long term storage of image data, but they are slow in transferring data to and from the computer. They are also used for data transformation between different computer systems. The magnetic tape is a sequential-access device, thus it may take several minutes to locate a file. This

Chapter 4

particular magnetic tape device uses 9-track tapes, on which data are stored as 8-bit bytes. The ninth track is used for the parity bit, and data transfer speed is specified as 36,000 bytes per second.

The paper tape reader/punch device is rarely used for storing data because it is slow and the paper tape is 'bulky'. It can read 300 characters per second and punch 50 characters per second. Unfortunately, the paper tape facility was the only means of communication between the GAMMA-11 system and our Department's PDP-11 system.

Finally, the interface hardware of the GAMMA-11 system include the interfaces between the CPU and the peripherals and the gamma camera interface, which links the camera to the computer. The gamma camera interface is responsible for receiving the gamma camera data, digitizing them in a form suitable for the computer and transferring them to the computer.

(ii) Computer Software

The GAMMA-11 computer system operates under the RT-11 operating system. This operating system is divided into two parts: the monitor and the utilities. The monitor enables the user to call programs, programming languages, and the utilities by typing appropriate commands. It also controls the efficient operation of the computer system. The utilities are commands

Chapter 4

that provide the user with services, like editing programs, copying programs etc. Appendix {II} gives an outline of the RT-11 operating system.

The software of the GAMMA-11 system allows the user to program the computer to execute different tasks in three different programming languages: BASIC, FORTRAN, and FOCAL.

The GAMMA-11 software also includes specific programs for the analysis and processing of gamma images.

4.2.3 Data Recording and File Structure

The three output signals of the Anger camera are received by the gamma camera interface. There, a pulse height selector retains only the events whose energy falls within a desired range. From there the X and Y location signals of the events which manage to pass through the pulse-selector are digitised and transferred to the computer, where for each received event the matrix cell (X,Y) of a square matrix array is incremented by one. After a time interval of continuous imaging, each matrix cell will contain a count number, which is proportional to the number of acceptable events that occurred in a finite area on the scintillation plate of the Anger camera. Finally, the image matrix is transferred from core to be permanently stored on disc.

This type of data collection is referred to as Matrix-Mode.

Matrices can be collected in three different sizes: [32X32], [64X64], [128X128]. Each matrix cell is stored as a digital 8-bit number (byte), or as a 16-bit number (word) on the cartridge disc.

There is another type of data collection, the List Mode, which collects a list of events as they occur. To view an image, the list has to be transferred into a matrix after collection. In this work data were collected in the Matrix Mode.

Each study of the heart may consist of a number of image matrices, e.g. the matrices of the four conventional views of the heart, and is stored on a disc as GAMMA-11 file. The structure of the GAMMA-11 files used for this work is the following:

1. The first disc block, the administrative block, holds general information such as the patient's name, doctor's name, isotope, dose etc. There is an administrative block for each data matrix (or frame) of the GAMMA-11 file.
2. The second block, the comment block, holds the text of comments typed during the patient examination. There is one comment block in each GAMMA-11 file.
3. The rest of the blocks hold the data matrix.
4. The pattern 'administrative block-matrix blocks' repeats itself for all image matrices of the particular

study.

This type of GAMMA-11 file is called a Multiple-Static-Study-File. Figure 4.4 shows its structural diagram. From this diagram it is noted:

- (a) Each administrative block is linked to the other administrative blocks of the file.
- (b) Each image matrix (data frame) is linked to the common block.

(First Administrative
Data Block is \emptyset)

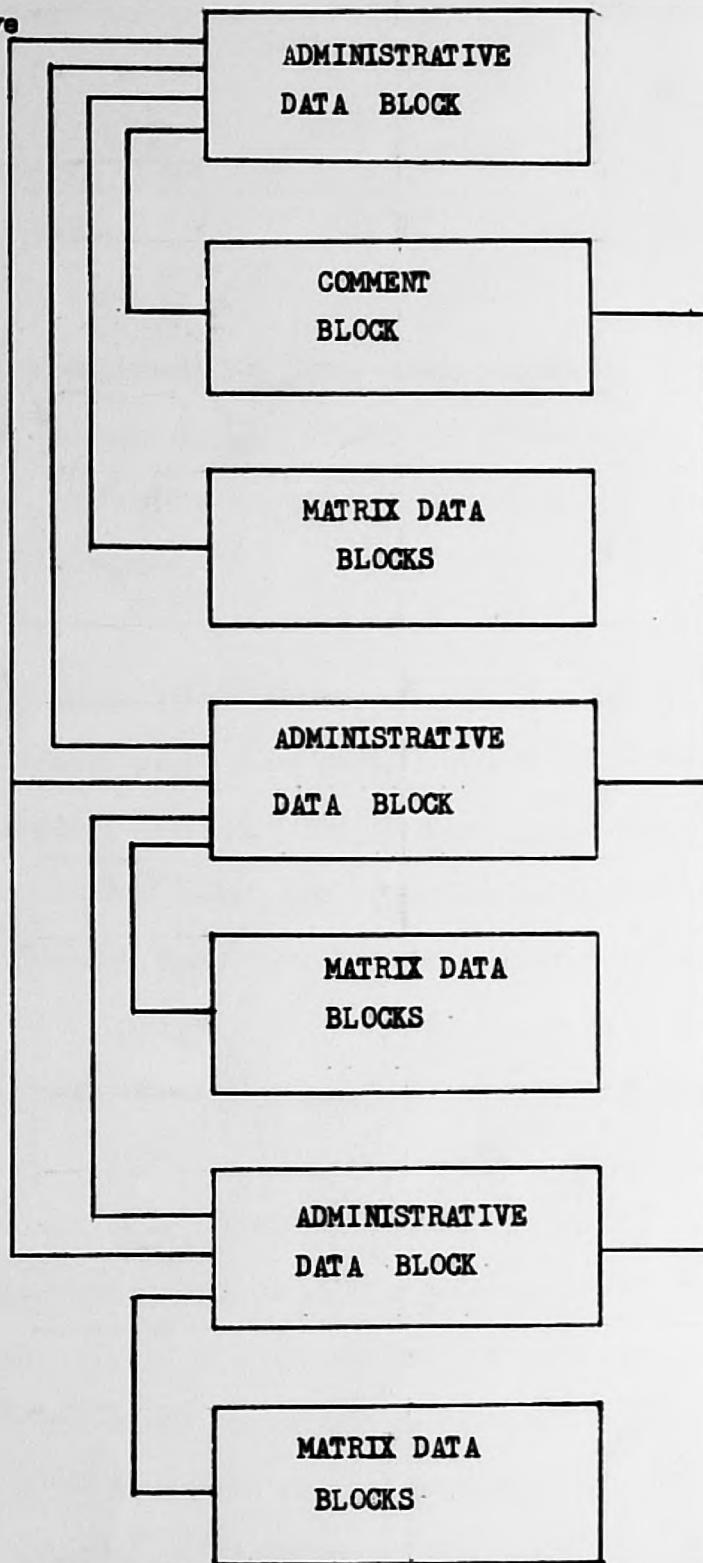


Figure 4.4
Multiple - Static - Study File.

4.3 DATA PROCESSING SYSTEM (PDP-11/10)

Software development for gamma image processing was performed in the Systems Science PDP-11/10 computer system. Data were punched on paper tape at Guy's and read into the PDP-11/10 minicomputer by the system's tape reader.

Figure 4.5 shows a block diagram of the PDP-11/10 computer system. The central processing unit is the PDP-11/10 version of the PDP-11 minicomputer series (see Appendix{I}) with core memory capacity of 24K words. The CPU controls all functions of the computer and operates under the RT-11 operating system.

(i) Hardware: Communication and Backing store peripherals.

The Tektronix 4006-1 computer display terminal is an I/O device used for communicating with the CPU and for plotting images. It is a storage tube device fitted with a keyboard, operating controls, and electronic circuitry to operate the display and communicate with the computer. The Tektronix (TK) resolution is 1024 addressable points along the X-axis and 780 along the Y-axis. It operates under two modes: Alphanumeric mode, which permits entry and display of letters, numbers, special characters to the computer to control the computer and to display the computer's response and Graphic mode, which permits the user to plot graphs, images, etc. All image processing results produced in this work, were displayed on the

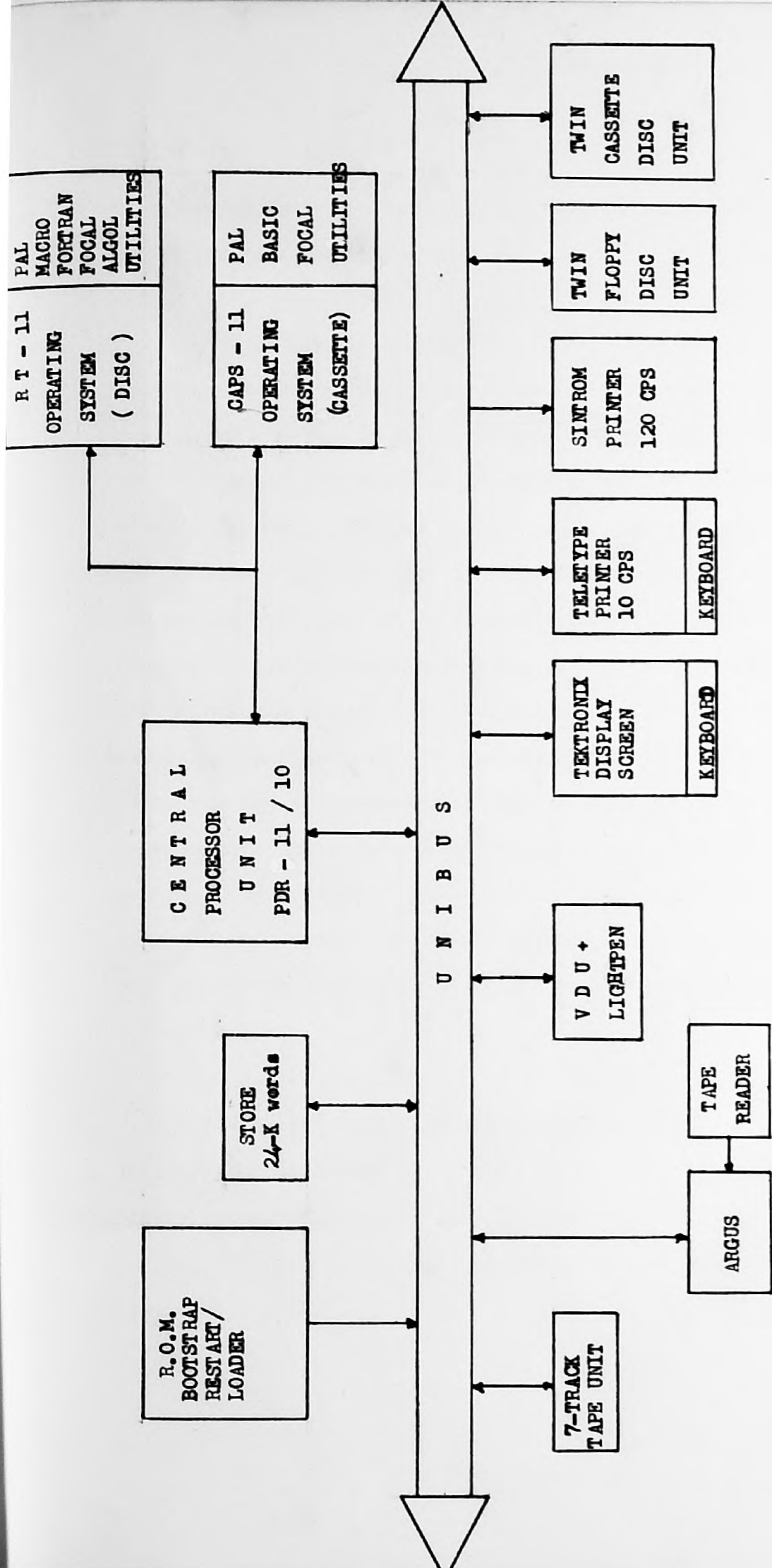


Figure 4.5
Schematic diagram of the PDP-11/10 computer system.

Chapter 4

TK-screen by means of specialised software existing or developed by the author (see software of this section).

The GT42 visual display unit (VDU) is an I/O terminal interfaced to the computer, which can display either alphanumeric or graphic information such as drawings, diagrams or patterns. It can display dynamic fast changing information such as waveforms, which can be instantly modified using the light pen facility. The TK-keyboard is also used for typing commands on the GT42 VDU to communicate with the CPU. It can display 8 intensity levels (tones of grey) having a resolution of 1024 addressable points along the X-axis and 768 along the Y-axis. It is a refresh display device rendering the display of two-dimensional gamma images inconvenient, since it requires large computer memory space for displaying a 64X64 image array. This terminal, however, was extensively used for programming the computer, since it permits advanced editing, in that it can display under the editor (see Appendix{II}) several lines of text and modify it by positioning a pointer to the desired location in the text.

Hardcopy output of program listings and results can be obtained by the Sintrom Printer. This is a dot matrix printer, microprocessor controlled, fast enough to print 120 characters per second. The printer is an output peripheral interfaced to the computer.

Chapter 4

The Teletype Printer is an I/O device fitted with a keyboard capable of printing only 10 characters per second, thus it is rarely used. It includes a tape reader/punch facility.

The Tape Reader is a fast reading device interfaced to the Argus computer, which is in turn linked to the PDP-11/10 computer system. This facility was used extensively for reading the paper tapes on which the image data were punched at Guy's.

The Twin-Floppy-Disc device is the most convenient mass storage device existing in the Department's computer system. It is similar to the cartridge disc device of the GAMMA-11 system. The floppy disc peripheral is a mass storage disc drive and control device with two discs: the SYSTEM disc, which contains the system's software and the user's disc, on which the user's programs and data are stored. Floppy discs are convenient and inexpensive, but they are limited in their storage capacity. Each floppy disc has 480 blocks and can store 256 bytes per block, thus providing the user with about 120 thousand words of available store. They are random access devices having directories similar to the cartridge discs.

The 7-track Magnetic Tape unit is similar to the 9-track Magnetic Tape unit of the GAMMA-11 system, except that information is stored as 6-bit characters. This facility was only used for storing on long term basis image data from floppy discs. Obviously, 9-track tapes cannot be read from the 7-track device.

Chapter 4

Finally, interfaced to the computer is the Twin Cassette unit, operating under the CAPS-11 operating system, mainly used nowadays for bootstrapping the computer. It can be also used for storing data on cassettes.

(ii) Software

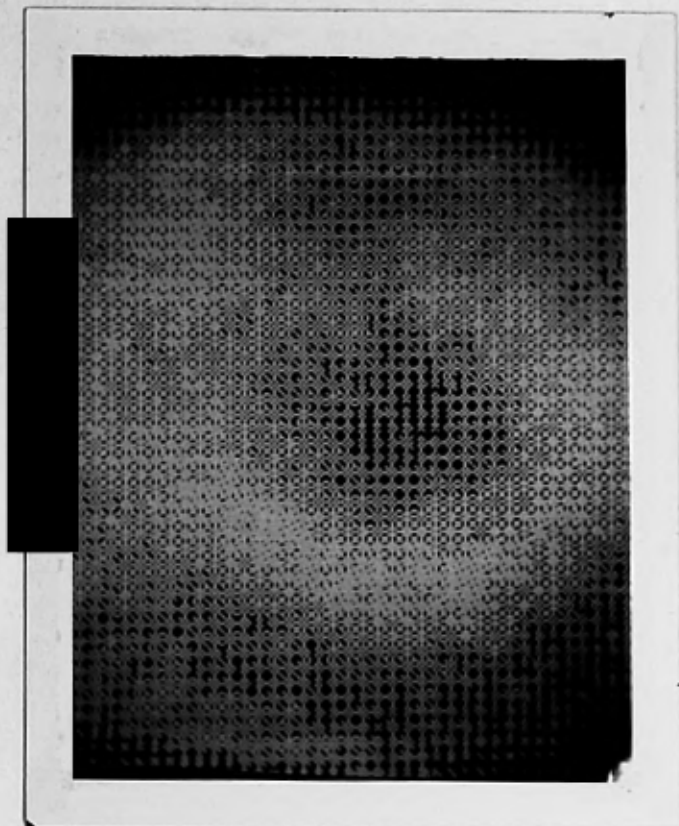
The PDP-11/10 computer system operates under the RT-11 operating system (see Appendix{II}). Programming languages include PAL, MACRO, FORTRAN, FOCAL, and ALGOL. The CAPS-11 operating system, for cassettes only, includes PAL, BASIC, and FOCAL programming languages.

Specialised software for plotting images on the Tektronix screen include the GPLOT library of routines, residing on the SYSTEM'S disc, which plot points or draw lines between points. These routines were used for developing a HALF-TONE routine, which depicts the intensity variation across the image by filling up a square pixel of 5X5 dimensions with bright spots for each image matrix cell. Obviously, the image matrix values had to be previously scaled down to 0-25 value range. Thus 26 distinct levels of grey could be plotted on the TK-screen. All images used in this work were plotted using this HALF-TONE routine. Plotting an image by this routine is a lengthy process, consuming about 20mins for a 64X64 image. This necessitated the development of an OVERPRINTING routine, which was used for plotting images during the development

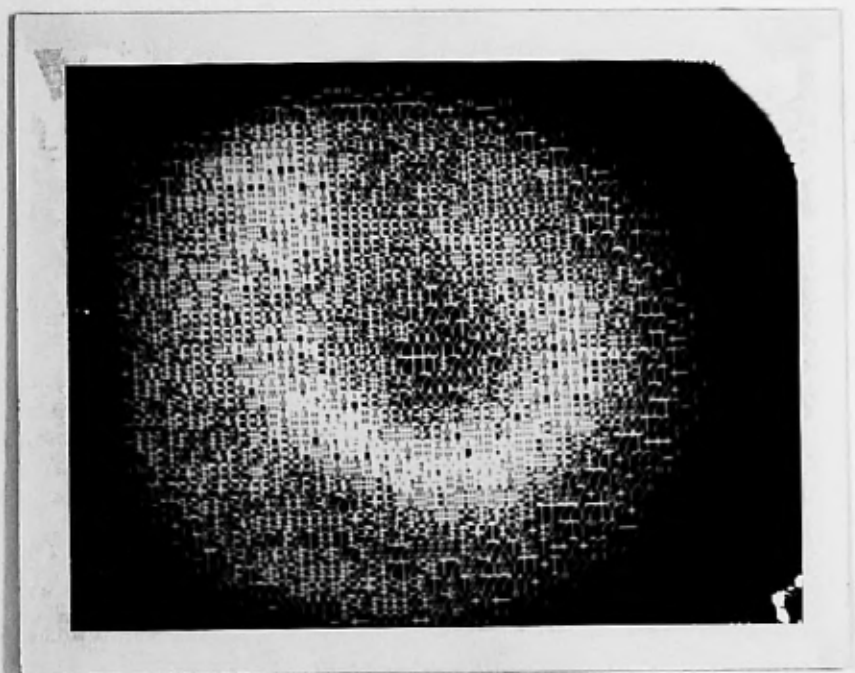
Chapter 4

of the image processing algorithms. The TK-screen displays characters in 7X5 dot matrix form. Suitable combinations of alphanumeric characters can fill up the rectangular dot-matrix cell, by means of the overprinting facility of the TK, thus providing 36 distinct grey levels. Interpolatory techniques were used on the images in compensating for the 7X5 rectangular shape of the cell so that the images would not appear 'long'. The image of Figure 4.6(a) is the plot of a heart image using the overprinting routine. The same image, but plotted with the HALFTONE routine, appears in Figure 4.6(b). Obviously, the plots obtained by the OVERRPRINTING routine are impressive. The time consumed for a 64X64 image to be plotted was about 3 mins, a remarkable reduction, which facilitated greatly the authors work.

The rest of the specialised software developed for image processing and three-dimensional reconstruction are extensively described in chapters 6, 7, 8, and 9.



(a)



(b)

Figure 4.6

Demonstration of overprinting routine on Left Lateral view of the heart.

Chapter 5

5 FORMATION AND PROPERTIES OF GAMMA CAMERA IMAGES

The purpose of this chapter is to give the theoretical background for the processes involved in the formation of the Anger camera images and to investigate their properties. Gamma images are severely degraded by Poisson noise, photon attenuation and photon scattering phenomena. These sources of image degradation are thoroughly examined in this chapter and their distortions are mathematically formulated or assessed, as a preliminary step to our attempt to reverse their effect on the gamma images prior to any three-dimensional reconstruction attempt.

5.1 THE IMAGE.

The Anger camera image is a two-dimensional projection of a three-dimensional radioisotope distribution. The image function, which describes the Anger camera image, can be thought of, for a black-and-white picture, as a real, single-valued nonnegative function $g(x,y)$ of the two variables (x,y) . The value of this function at a point (x,y) is proportional to the gamma ray energy incident on that point. This is called the 'intensity', 'brightness', or 'grey level' of the picture at this point.

In computer image processing the images are represented as discrete matrices, or arrays, of nonnegative numbers. In this work the different grey levels of a picture will be plotted on a Tektronik screen using for this purpose a specially devised half-tone routine. Each image will be scaled down to 26 distinct levels (0-25), where 0 corresponds to a zero intensity point and 25 corresponds to the maximum intensity point of the discrete $g(x,y)$ function. Each point of $g(x,y)$ will be represented on the TK-screen by a square 5*5 point pixel. An example of such a picture is given in chapter 6 Figure 6.3.

5.1.1 Mathematical analysis of image formation process

The process of image formation is adequately explained by the schematic diagram of Figure 5.1. As observed $f(m,n)$ is a two-dimensional object in the (M,N) coordinate system emitting radiant energy which propagates through space. The image formation system, the rectangular box in Figure 5.1, transforms the radiant energy propagating towards the image plane appropriately to be sensed and recorded by a sensor in the image plane. Thus an image $g(x,y)$ is formed in the (X,Y) plane.

However, in this image formation process there is not a 'one to one' relationship. A point (x_1, y_1) in the image plane is formed by the radiant energy contributions of its corresponding point (m_0, n_0) in the object plane and the neighbourhood points surrounding the object point.

The image formation system is responsible for the transformation of radiant energies from the object plane to the image plane. This transformation can be mathematically described by a function h , which describes how an object point and its neighbourhood contribute radiant energies in the formation of an image point. If the image formation system and the image detection system are considered linear and assuming that the image is formed by an infinite number of point sources, then the formation of an image can be described by the equation:

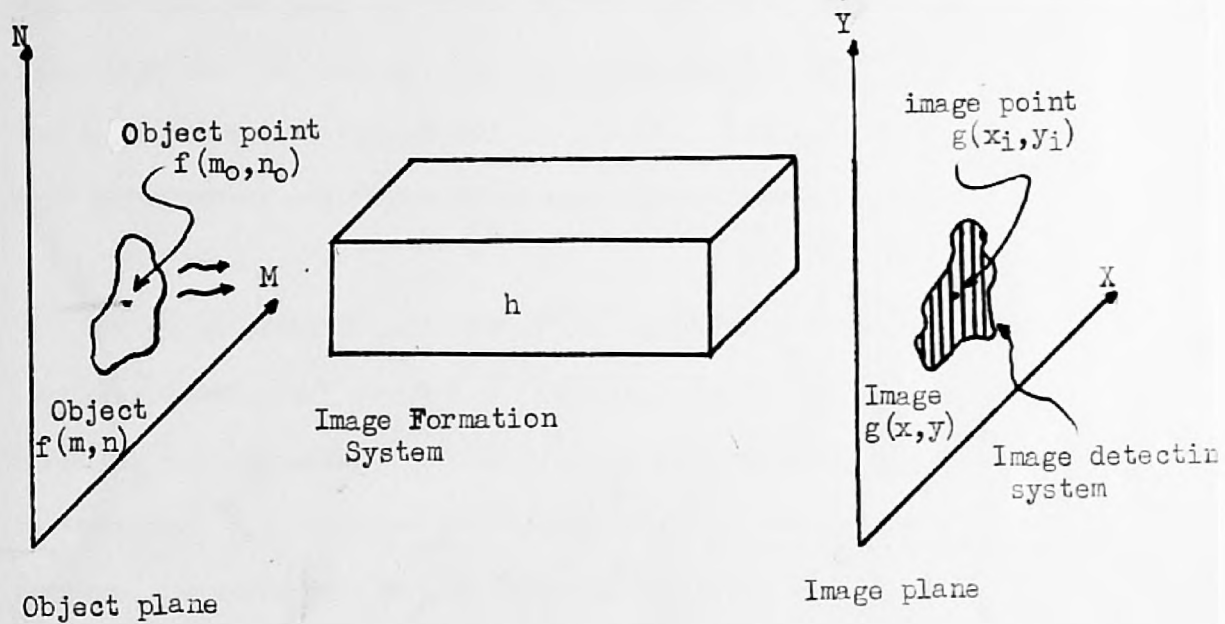


Figure 5.1
Image formation principle.

$$g(x,y) = \int_{-\infty}^{\infty} \int_{-\infty}^{\infty} (h(x,y,m,n) \cdot f(m,n) \cdot dm \cdot dn) + v(x,y) \quad 5.1$$

where, $g(x,y)$ is the image function, $f(m,n)$ is the object function, $h(x,y,m,n)$ is the 'image formation system' function and $v(x,y)$ is the noise function. It is observed that function h depends upon the four variables of the two coordinate systems. This function is called the the POINT SPREAD FUNCTION (PSF) of the image formation system and in its most general form varies with position in both the object and image planes.

If it is assumed (as justified experimentally to a good approximation), for practical reasons, that the point spread function is independent of position in the object plane, then h in equation 5.1 becomes a function of the relative displacement between the variables in the two coordinate systems.

Equation 5.1 can be now written as:

$$g(x,y) = \int_{-\infty}^{\infty} \int_{-\infty}^{\infty} (h(x-m,y-n) \cdot f(m,n) \cdot dm \cdot dn) + v(x,y) \quad 5.2$$

Again if it is assumed that both the image and the object are defined over finite spatial intervals and that the contribution of radiant energies to a point in the image is from a finite number of neighbourhood points around the corresponding object

point, then equation 5.2 can be written as:

$$g(x,y) = \int_1^x \int_1^y (h(x-m,y-n) \cdot f(m,n) dm dn) + v(x,y) \quad 5.3$$

The discrete approximation to 5.3 has the form:

$$g(x.\Delta x, y.\Delta y) \cong \sum_{m=1}^x \sum_{n=1}^y (h((x-m).\Delta x, (y-n).\Delta y) \cdot f(m.\Delta x, n.\Delta y)) + v(x.\Delta x, y.\Delta y) \quad 5.4$$

for $\Delta x = \Delta y = 1$

$$g(x,y) = \sum_{m=1}^x \sum_{n=1}^y (h(x-m,y-n) \cdot f(m,n)) + v(x,y) \quad 5.5$$

In equation 5.5 the operation between h and f in the space domain is the familiar circular convolution. Thus 5.5 can be expressed as:

$$g(x,y) = h(x,y) * f(x,y) + v(x,y) \quad 5.6$$

Chapter 5

where * is the sign of the convolution.

5.1.2 Radioactive source-Process of radioactive decay

Following the mathematical analysis of the image formation process, the physical processes in the radiation emitting sources and the fate of the radiation are examined next, to assist us in appreciating the special problems involved in emission computed tomography.

Radionuclides are widely used in Nuclear Medicine in examining the internal organs of the human body. There are two broad categories of radionuclides: those which emit single photons and those which emit positrons and photons. The isotopes used for this work belong to the first category and they are: Thallium-201 (^{201}Tl) and Technetium-99m ($^{99\text{m}}\text{Tc}$).

Thallium decays with the emission of photons in three distinct energies: 80 keV, 135 keV and 167 keV. Radionuclide Thallium has 120 neutrons and 81 protons in its atom. Non radioactive Thallium has 123 neutrons and 81 protons. In the atom of ^{201}Tl when the k-orbit electron comes near to the nucleus it interacts with a proton and creates another neutron. The loss of a proton from the nucleus transfers this atom into a

Chapter 5

Mercury (Hg) atom with its k-shell empty. When a free electron is captured in this shell a photon is released at 80 keV. A very small percentage of the Thallium-201 decay, about 8%, results in photons at 135 keV or 167 keV energies.

Technetium-99m arises from the decay of 99-Mo. This isotope is in a metastable state. When an electron is emitted by 99-Mo, its daughter nucleus 99m-Tc remains in an excited state emitting photons at 140 keV with a half-life of six hours.

Thallium-201 is used for routine clinical studies of the heart, because it distributes well around the muscle tissue of the myocardium. 99m-Tc does not possess this quality and it is used for other medical applications (e.g. determination of cardiac blood pool).

5.1.3 Image formation procedure

Figure 5.2 indicates a three-dimensional object emitting gamma radiation situated in a homogeneous medium. An Anger camera fitted with a multihole collimator is situated at a distance R from the centre of gravity of the object. Radiation is emitted by the object in all directions and the Anger camera receives only those gamma rays which fall perpendicularly to the surface of its collimators.

The object can be considered to consist of unit volume radioactive sources emitting gamma rays in all directions. If we consider a cylindrical ray of finite dimensions, intercepting the collimator plane perpendicularly, then we can define the projection ray sum as 'the total radioactivity emitted along the direction of the ray in a given time interval'. The Anger camera will record a finite number of projection ray sums from the object which will constitute the two-dimensional projection image of the three-dimensional object. This can be expressed as:

$$f(y,z) = \sum_{m=1}^{m_f} O(m,n,l) \quad 5.7$$

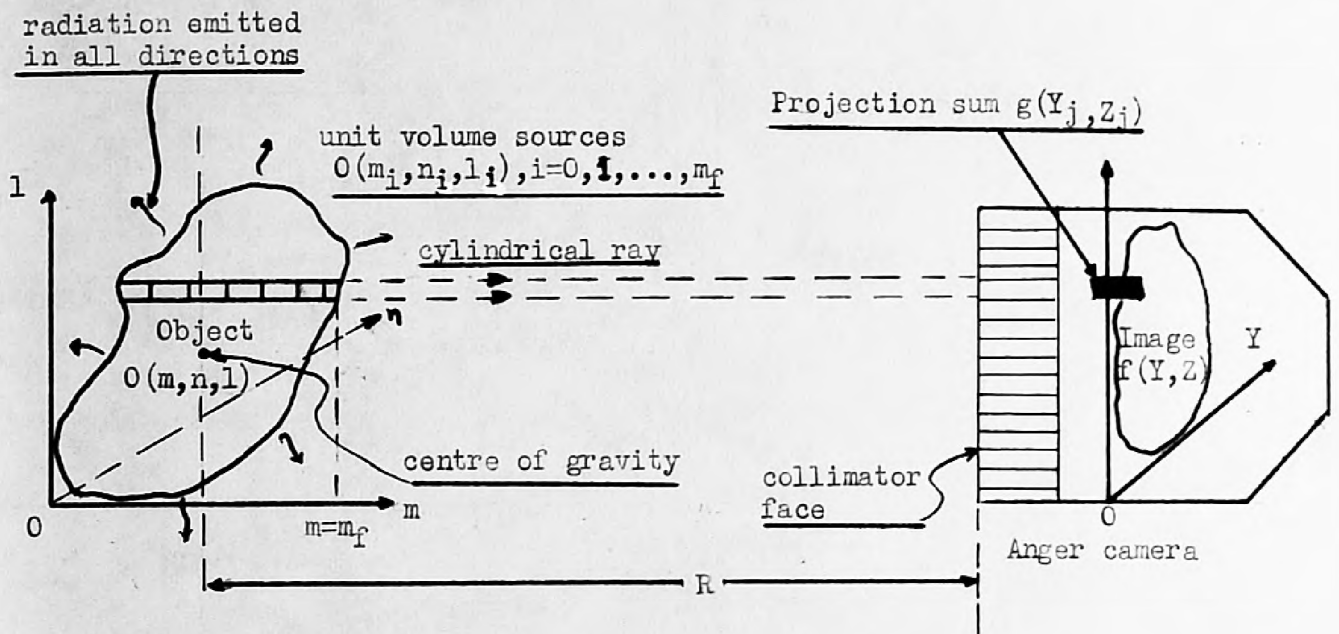


Figure 5.2

The two dimensional projected image $g(Y, Z)$ of the three dimension object $f(m, n, l)$ emitting gamma ray photons.

where $f(y,z)$ is a projection sum of a notional ray (or a resolution cell) in the two dimensional image, $O(m,n,l)$ is a unit volume in the three-dimensional object, m_f is the m -axis boundary coordinate, and the m -axis has been considered perpendicular to the camera plane.

It is noted here that, for simplicity, no mention was made in equation 5.7 of the PSF of the image formation system or of the effects of noise. If these were to be included, and taking into consideration equation 5.5, equation 5.7 would become:

$$g(y,z) = \sum_{n=1}^y \sum_{l=1}^z \{h(y-n,z-l) \cdot f(y,z)\} + v(y,z)$$

or

$$g(y,z) = \left\{ \sum_{n=1}^y \sum_{l=1}^z h(y-n,z-l) \cdot \sum_{m=1}^{m_f} O(m,n,l) \right\} + n(y,z) \quad 5.8$$

where the point spread function and the noise function have been assumed two-dimensional. This is an assumption which is justified in later chapters.

The multihole collimator of the Anger camera collects the projection ray sums and through electronic circuitry they are stored on magnetic tapes as 64X64 matrices. Typical images of the heart using Thallium-201 radionuclide can be seen in Figures

Chapter 5

6.3 of chapter 6. These images are plotted on a TK-screen using a half-tone plotting routine.

5.2 SOURCES OF DEGRADATION

In the image formation process two sources of image degradation have been mentioned so far, the point spread function of the image formation system and the noise function, $h(x,y)$ and $n(x,y)$ respectively, both included in equation 5.6. There are, for gamma ray images, two additional sources of image degradation, photon attenuation due to interaction with matter between the source of radiation and the collimator plane and photon scattering caused by the Anger camera detecting system.

These sources of image degradation cause serious distortions in the received images and a thorough examination of their nature is a necessary prerequisite to any attempt at their partial or total elimination.

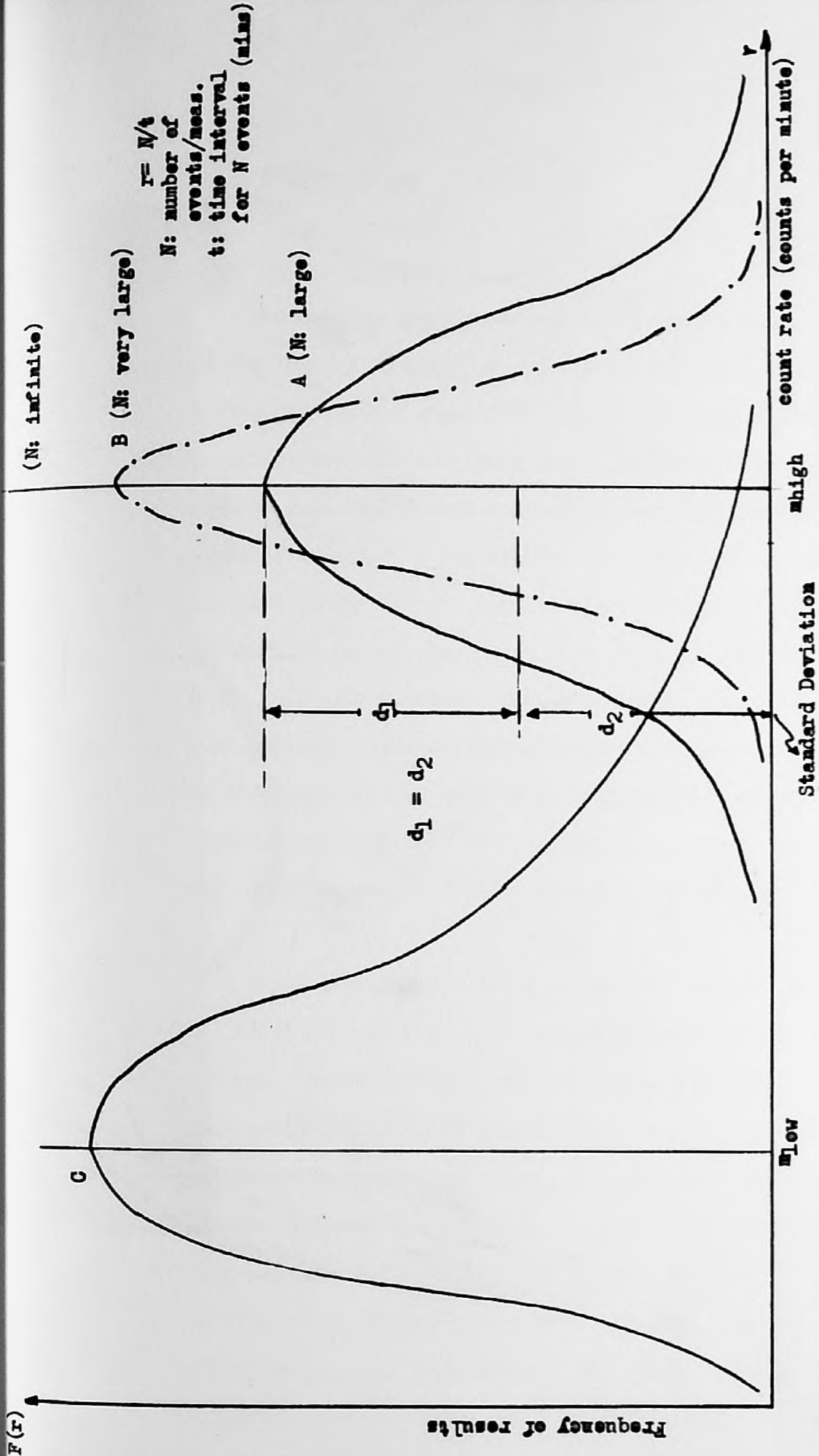


Figure 5.3
Poisson Distribution curves.

5.2.1 Poisson Noise

Radioactive decay is a completely random phenomenon subject to the laws of probability and statistics. Each radionuclide has a characteristic probability exponential decay curve, which gives an indication of the chance that a photon will be emitted during a given interval of time. A conventional way of expressing this probability for a particular isotope, is to measure its half-life, that is, the time interval required for half of its radioactive nuclei to decay. Evidently, for an isotope with short half-life a greater number of nuclei will decay, and thus more photons will be emitted in a given length of time than for an isotope with long half-life. The unit of measurement of the radioactive material is the curie, defined as $3.7 * 10^{10}$ disintegrations per second from 1gm of radioactive material[50].

The probabilistic nature of the radioactive decay introduces a statistical uncertainty to any measurement of emitted photons from an isotope source during a given time interval. The type and magnitude of this statistical error (or noise) can be estimated by examining the shape of the curve resulting if photons detected per minute are plotted against the frequency of occurrence of the results as shown in Figure 5.3. For each measurement a certain number N of counts is recorded and the count rate r is calculated from $r=N/t$, where t is the time interval required for N events to be detected. The bell shaped

Chapter 5

curve A attains its maximum value at the mean (true) value of the count rate m . This is the Poisson distribution curve and it approximates the normal distribution (Gaussian) for large values of m . If N were to be increased (m remaining the same) the shape of the Poisson curve becomes taller and slimmer (curve B). For infinite events per measurement ($N \rightarrow \infty$) the curve reduces to the ideal shape of an impulse, i.e. a straight line parallel to the Y-axis, and there is no statistical error or noise. For small m (curve C) the Poisson distribution curve becomes asymmetrical about m [50]. Thus the noise which is introduced by the radionuclide disintegration to the gamma image is Poisson noise.

The mathematical expression for the Poisson distribution is the following:

$$F(r) = \frac{m^r}{r!} \cdot e^{-m}$$

where,

$F(r)$: is the frequency of results

r : is the count rate, $r=N/t$

N : is the number of events recorded in time interval t .

m : is the mean value of r .

Chapter 5

The above equation expresses the probability that for a given m and N a count rate r will be obtained.

Any single measurement can fall at any point on the curve of Figure 5.3, but it has very little chance of falling at the maximum of the curve. It is most likely therefore that this measurement will be inaccurate.

However, an indication of the probable accuracy can be obtained by expressing this accuracy in terms of the deviation from the mean value (the peak of the curve) to a value at a point on the curve the height of which is half that of the maximum point. This deviation is called the standard deviation of the Poisson curve. It is a well known fact that the variance of the Poisson curve is equal to its mean value [24]. It is also known that the standard deviation is the square root of the variance. If it is now assumed that the observed count of the particular measurement is an estimate of the mean and variance, then the standard deviation is the square root of the recorded measurement. It is therefore proved that for large m the magnitude of the Poisson noise effect is small, however not negligible. It is also proved that the noise level is signal dependent, since it is the square root of the signal. Thus the Poisson noise effect can be considered as a two-dimensional process in the image plane contributing a small magnitude term in equation 5.8.

5.2.2 Scattering

The interaction of emitted gamma rays with matter is an important factor in the image formation process affecting considerably the clarity of the received images. One of the forms that this interaction takes is scattering.

A radioactive point source will emit gamma-ray photons in all possible directions. An Anger camera situated at distance R from this point source will record those photons which fall only at right angles to its plane of collimation. However, there are photons, which although they are emitted in a different direction, change their path through interaction with matter, fall on the collimator plane at right angles, and are recorded by the Anger camera. Thus, after a period of recording time the image of the point source would appear as a circular disc. This contributes to the point spread function of the image formation system, whose mathematical expression was considered previously in 5.11.

There is however an additional distortion of similar nature, introduced by the image detecting system, i.e. the Anger camera. This distortion is the combined effect of the geometric efficiency of the collimator, of the detection efficiency of the scintillator and of the background radiation, as described in

Chapter 5

chapter 4, and it defines the point spread function of the detecting system.

These two sources lumped together constitute the total scattering phenomenon, which is characterised by the system point spread function (PSF). The PSF of the system is then defined as 'the final image produced by a unit point radioactive source in the Anger camera detecting system.'

For practical Anger cameras the system PSF can be approximated by a two-dimensional Gaussian function [1,8]. An assessment of the spatial resolution (or PSF) of a particular system is obtained by measuring the full width at half maximum (FWHM) of this Gaussian function [25]. The system resolution deteriorates linearly with the distance of the source from the collimator head but is invariant across the image. Figure 5.4 shows the variation of the system resolution with distance from the collimator face. For an Anger camera fitted with a high resolution collimator the resolution obtainable at the face of the collimator is approximately 8 mm FWHM for 72 keV photon energies (^{201}Tl) and 5 mm FWHM for 140 keV energies ($^{99\text{m}}\text{Tc}$).

It is now possible to approximate the system PSF with a two-dimensional Gaussian function $h(y,z)$:

$$h(y,z) = \left\{ \frac{C_1}{\sqrt{2\pi} \cdot (K_1 R + K_2)^2} \right\} \cdot \exp \left\{ \frac{-(y^2 + z^2)}{2(K_1 R + K_2)^2} \right\} \quad 5.9$$

High Resolution
Collimator

72 kev

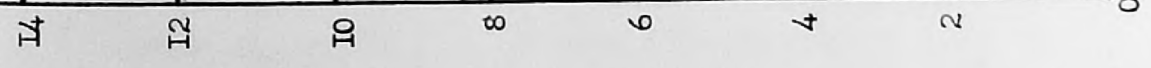
140 kev

System Resolution (FWHM) mm.

Distance from Collimator phase . cm.

Figure 5.4

Anger Camera
resolution variation
with distance from
collimator.



where C_1, K_1 and K_2 are constants and R is the separation between the camera and the source. If R remains constant the denominator of 5.9 becomes constant and 5.9 reduces to:

$$h(y,z) = \frac{C_2}{C_3} * \exp\left(-\frac{(y^2+z^2)}{2C_3}\right) \quad 5.10$$

where,

$$C_3 = K_1 R + K_2 \quad \text{and} \quad C_2 = C_1 / \sqrt{2\pi}$$

5.2.3 Attenuation

An other source of distortion in the images recorded by the Anger camera system is the attenuation of the gamma photons due to interaction with the matter between the source and the collimator's face. The absorption of photons by matter increases in an exponential manner with the distance between the source and the collimator. An assessment of the seriousness of photon attenuation can be obtained from Figure 5.5 where only about 48% of Technetium emitted photons or 40% of Thallium emitted photons are transmitted through 5cm of water (or human tissue).

If I_0 is the number of emitted photons in a given length of time from a point source S towards the collimator head of the Anger camera at distance R from the source, then the received number of photons I in the same time interval is given by:

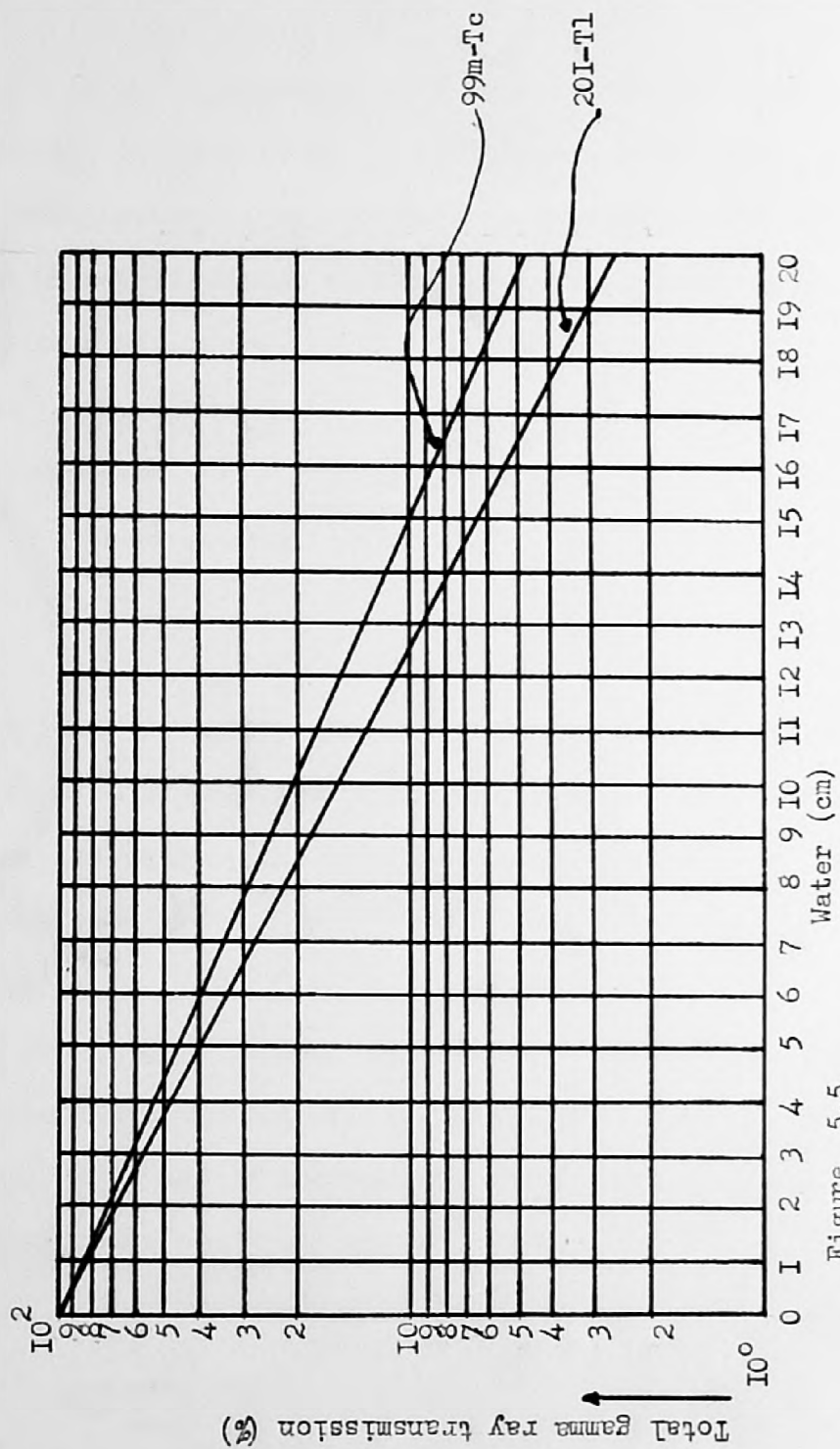


Figure 5.5

Attenuation of photons in water

$$I = I_0 \cdot e^{-\mu R} \quad 5.11$$

where μ is the attenuation coefficient of the surrounding medium. To obtain an estimate of the radioisotope concentration present in the point source, it is necessary to take under consideration the total number of photons emitted from the point source in all directions in space within the same length of time. Thus from 5.11:

$$I_d = \frac{I_t}{4\pi R^2} * e^{-\mu R} \quad 5.12$$

where I_t is the total number of photons emitted by the point source in the specified interval of time and I_d is the number of photons detected by the camera per unit area and per unit time interval.

If the space between the collimator head and the camera is considered to consist of n different media, each of thickness d_i ($i=1,2,\dots,n$) and of attenuation coefficient μ_i ($i=1,2,\dots,n$), then 5.12 becomes:

$$I_d = \frac{I_t}{4\pi R^2} * e^{-T} \quad 5.13$$

where

$$T = \sum_{i=1}^n \mu_i d_i \quad 5.14$$

If the point source attains finite dimensions and assuming for simplicity that the medium surrounding the body does not attenuate the emitted photons, then equation 5.7, which describes the formation of the projection image, can be modified to include the attenuation effect:

$$f(y, z) = \frac{1}{4\pi} \sum_{m=1}^{m_f} \frac{O(m, n, l)}{(m_f - m)^2} * \exp(-\mu(m_f - m)) \quad 5.15$$

where the three-dimensional object is considered to consist of finite volume radioactive sources $O(m, n, l)$ and the term $(m_f - m)$ indicates the distance between a unit volume source and the edge of the object., (see Figure 5.2).

If the point spread function of the system, as defined by equation 5.10, were to be included, then from 5.8 and 5.15:

$$g(y, z) = \frac{1}{4\pi} \sum_{n=1}^y \sum_{l=1}^z \exp(-C[(y-n)^2 + (z-l)^2]) * \sum_{m=1}^{m_f} \frac{O(m, n, l)}{(m_f - m)^2} * \exp(-\mu(m_f - m)) + n(y, z) \quad 5.16$$

Chapter 5

Equation 5.16 constitutes the complete mathematical description of the image formation process with noise, attenuation and scattering phenomena incorporated. Here the term 'image formation process' means the whole process of image formation and detection, with their corresponding degradations included in equation 5.16.

The image formation procedure is schematically represented in figure 5.6. This block diagram shows the structure of the image formation process and it helps the reader to visualize the whole process. The direction of photon emission is considered along the x -axis. A three-dimensional object $O(x,y,z)$ emits radiant energies which in their passage through the image formation system (IFS), are transformed into image radiant energies. In the IFS the object radiant energies are attenuated and convolved by the point spread function $h_i(y,z)$. Similarly the image radiant energies $g_i(y,z)$ in their passage through the image detecting system (IDS) are convolved with the detector's point spread function, $h_d(y,z)$. Finally, the intensities $g(y,z)$ are sensed by the detector after the Poisson noise process, $n(y,z)$, has been added.

It is necessary to point out here that the image recording system has not been included in the total process of image formation, because in the Anger camera recording system the oncoming photons produce an output signal which is directly proportional to the energy of the photons [18].

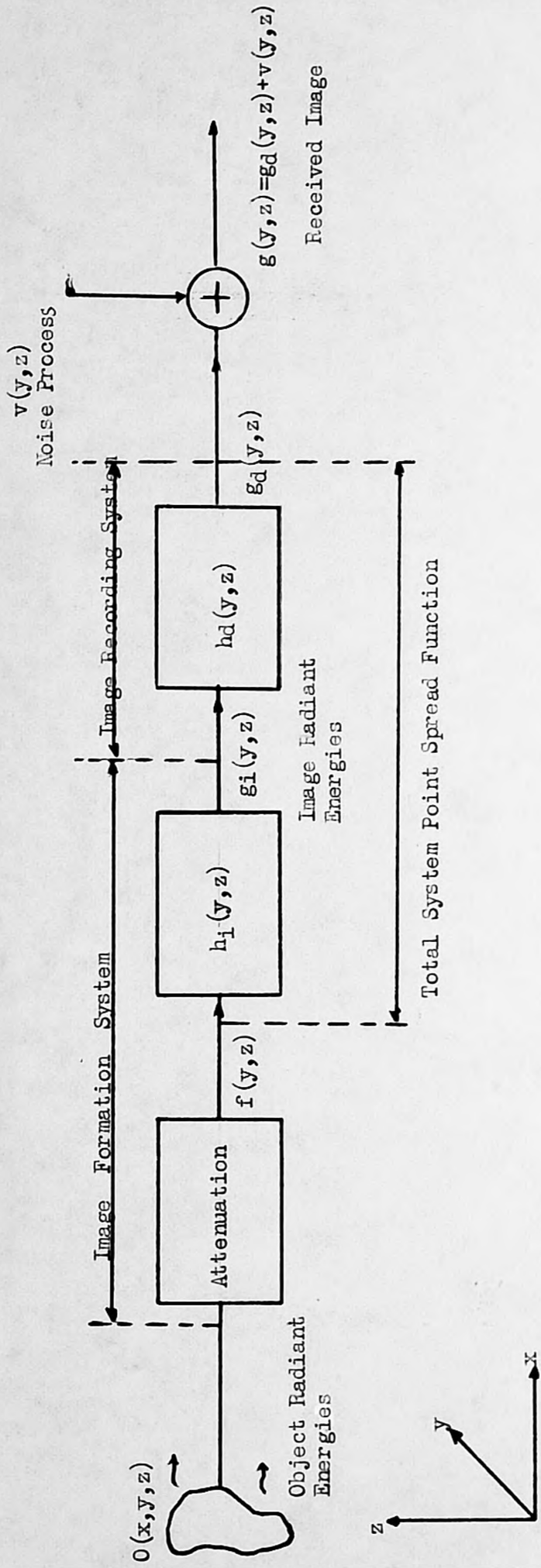


Figure 5.6

Block diagram of the Image Formation Process

6 PREPROCESSING ALGORITHMS

The purpose of this chapter is to describe the methods by which the effects of the different sources of degradation can be removed from the Anger camera images to prepare the restored images for insertion into the three-dimensional reconstruction algorithms. These preprocessing algorithms attempt to remove the effect of the scattering phenomena from the images, compensate for the attenuation phenomena and the Poisson noise effect and minimise distortion and corruption from the two-dimensional recorded images.

6.1 SCATTERING ELIMINATION

There are two basic reasons which necessitate the removal of the scattering effect or the system PSF from the gamma images, both closely linked with the performance of the reconstruction algorithms which are described in the next chapter.

First, the effect of photon scattering on the images is considerable loss of resolution. A lot of important information is thus obscured due to degradation in the sharpness and clarity of the images. Although camera technology has progressed immensely, poor image resolution is still a major problem. Obviously, poor resolution images would probably affect greatly the performance of the reconstruction algorithms.

Second, most researchers have tried to solve the three-dimensional reconstruction problem, by attempting to reconstruct two-dimensional slices of the object thus avoiding immense computer storage requirements involved otherwise. However, the transformation of the reconstruction problem from three to two dimensions -also applicable in this work- does not take into account that the projected images of two adjacent parallel slices, see Figure 6.1, overlap in the projection plane, due to the scattering effect. An error is thus introduced when attempting to reconstruct a slice of the object from a set of one-dimensional projections selected from the images.

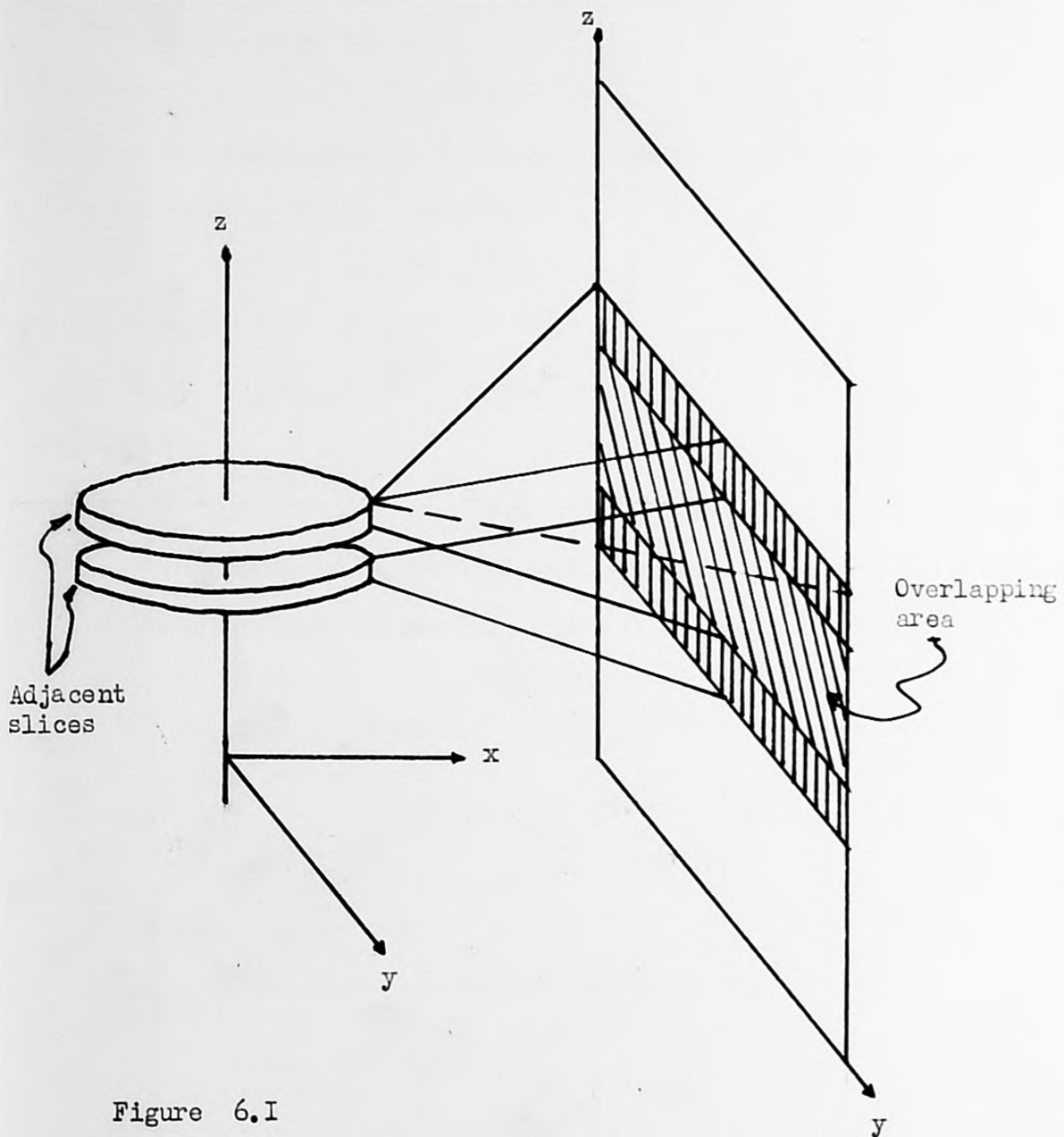


Figure 6.1

The emitted images of two adjacent parallel slices overlap

Chapter 6

Finally the removal of the scattering effect from the projected images improves the definition of the boundaries of the object image within the image matrix.

For those reasons it is important that the scattering effect is eliminated from the gamma images or at best minimised.

6.1.1 Assessing the restoration problem

The image formation process, mathematically described by equation 5.16, is rewritten here as follows:

$$g(y,z) = \sum_{n=1}^y \sum_{l=1}^z \{h(y-n, l-z) \cdot f(y,z)\} + v(y,z) \quad 6.1$$

where

$$h(y-n, l-z) = \frac{1}{4\sigma^2} \exp(-[(y-n)^2 + (z-l)^2])$$

is the system PSF

and

$$f(y,z) = \sum_{m=1}^{m_f} \frac{O(m,n,l)}{(m_f - m)^2} * \exp(-\mu(m_f - m))$$

is the original distribution of the object radiant intensities.

Image restoration will be defined as the process by which the intensity distribution $f(y,z)$ of an object is retrieved from its degraded image $g(y,z)$.

Before attempting to restore the gamma images, there are several factors which must be considered. First, in developing equation 6.1 both the image formation system and the image detection system in the image formation process were assumed to be linear. This assumption introduces an error, since the process of image formation by emission of gamma photons is known to be nonlinear [26]. Also the system point spread function is a function of the object radiant energy distribution as well. Thus:

$$\text{PSF} = h(y-n, l-n, f(y,z)) \quad 6.2$$

It can be proved however [12] that if $f(y,z)$ is varying slowly, then the system point spread function can be approximated by its form:

$$\text{PSF} = h(y-n, l-n) \quad 6.3$$

Chapter 6

In other words equation 6.3 is valid if $f(y,z)$ is expected to be smooth. This is a sound expectation particularly for the images considered here.

Second, the image is corrupted by Poisson noise, which is correlated with the object distribution $f(y,z)$. Although its contribution to the image was shown to be small, its effect cannot be exactly calculated or eliminated.

Finally, any image restoration method has to be seen in perspective with the reconstruction algorithm. It must be fast and simple, it must require small computer storage, and finally it must provide reasonable improvement in resolution. These requirements are mutually conflicting and thus the best compromise is required.

It has to be stressed that the objective of this restoration method is not to enhance the images alone, but to enhance them adequately well to improve the images resulting from the reconstruction algorithms.

The image formation process is a transformation in which radiant energies from the object are transformed into image radiant energies. If this transformation is signified by T , then the mapping of the function $f(y,z)$ in the object plane into a function $g(y,z)$ in the image plane can be expressed as:

$$T\{f(y,z)\} \rightarrow g(y,z) \quad 6.4$$

Chapter 6

The image restoration process can then be signified as the recovery of $f(y,z)$. This can be achieved only when the inverse transformation T^{-1} is possible. Then:

$$T^{-1}T \{f(y,z)\} \rightarrow T^{-1} \{g(y,z)\}$$

or

$$f(y,z) \rightarrow T^{-1}\{g(y,z)\} \quad 6.5$$

In case that the inverse transform does not exist the system will be considered to be singular. This is the case when in equation 6.1 the double summation term equals to zero:

$$\sum_{n=1}^y \sum_{l=1}^z h(y-n, l-z) \cdot f(y,z) = 0 \quad 6.6$$

The recovery of $f(x,y)$ is now impossible.

If the system is non-singular the recovery of the radiant energy distribution of the object $f(y,z)$ presented by equation 6.5 cannot be unique. This can be explained by examining equation 6.1. The Poisson noise contribution to the image formation process is a random process corrupting the image and it cannot be explicitly expressed. Thus there will be a number of solutions which will satisfy the relation 6.5.

These considerations are adequate to prove that the removal of the scattering phenomena from the images is a difficult task and that the original distribution $f(y,z)$ cannot be exactly recovered.

6.1.2 The Restoration

It was mentioned before, in equation 5.6, that the double summation of the system point spread function and the object energy distribution $f(y,z)$ is a convolution operation in the space domain. This leads to the realization that the restoration problem is a problem of deconvolving those two functions. It is well known [11] that the laborious mathematical operations involved in calculating the convolution of two functions in the space domain are significantly simplified when working in the spatial frequency domain. The transformation into the spatial frequency domain is in our case possible because the PSF is invariant (see chapter 5, page 4). Every signal defined in the space domain has an equivalent representation in the spatial frequency domain. Most important, in such a transformation all information is retained.

Chapter 6

This transformation is performed by the two-dimensional discrete Fourier Transform defined as:

$$G(u,v) = \sum_{y=1}^N \sum_{z=1}^N g(y,z) \cdot \exp\left[-2\pi j \frac{y}{N} \left(u + \frac{z}{N} v\right)\right] \quad 6.7$$

where u, v are the spatial frequencies of the image, and $j = \sqrt{-1}$

and where the image is considered as a square matrix $N \times N$ (64x64 in the case of the gamma images), and its inverse, that is the transformation from the spatial frequency domain to the space domain, is defined as:

$$g(y,z) = \frac{1}{N^2} \sum_{u=1}^N \sum_{v=1}^N G(u,v) \exp\left\{j 2\pi \left(\frac{y}{N} u + \frac{z}{N} v\right)\right\} \quad 6.8$$

It can be easily proved [11] that the circular convolution of two functions in the space domain is equivalent to their multiplication in the spatial frequency domain.

The Fourier Transform (FT) operating on equation 6.1 will transform it into its new form as:

$$G(u,v) = H(u,v) F(u,v) + N(u,v) \quad 6.9$$

where G, H, F, N are the FT's of g, h, f, v respectively. It is now obvious that if both sides of 6.9 are multiplied by the inverse of the FT of the point spread function, i.e $1/H(u,v)$ ($H(u,v)$ is frequently called the Modulation Transfer Function of the system) then:

$$\frac{G(u,v)}{H(u,v)} = F(u,v) + \frac{N(u,v)}{H(u,v)} \quad 6.10$$

It is necessary at this point to elaborate on equation 6.10 because it poses certain problems. It has been mentioned that the point spread function of the image formation system is Gaussian. It is trivial to prove here that its FT will also be Gaussian. In the high frequencies of the $u-v$ plane $H(u,v)$ will tend to zero, thus the quotient $N(u,v)/H(u,v)$ will attain large values. It is also known that noise is signal dependent and that the signal $f(y,z)$ is expected to be smooth. Thus the noise transform $N(u,v)$ will not drop rapidly with increasing frequencies in the $u-v$ plane. Consequently, as we get far from the origin of the $u-v$ plane the quotient $N(u,v)/H(u,v)$ will become very large, even larger than $F(u,v)$. Thus the inverse transform of $G(u,v)/H(u,v)$ will be strongly influenced by these large terms and will constitute an estimate bearing no relation to the original $f(y,z)$.

Chapter 6

These considerations indicate that $H(u,v)$ has to be modified properly so that noise will not dominate in the restoration procedure. This can be achieved by defining a new point spread function for the system:

$$h(y,z) = \begin{cases} h(y,z) & y^2+z^2 \leq D \\ P & y^2+z^2 > D \end{cases}$$

where P is the value of $h(y,z)$ at $y^2+z^2=D$. Consequently, since the system PSF is Gaussian, the System Modulation Transfer function will be defined as:

$$H(u,v) = \begin{cases} H(u,v) & u^2+v^2 \leq V \\ U & u^2+v^2 > V \end{cases}$$

where U is the value of $H(u,v)$ at $u^2+v^2=V$. Thus it can be assured that the noise contribution will be small and that the quotient $G(u,v)/H(u,v)$ will take realistic values. If the right hand side of equation 6.10 is represented by $\hat{F}(u,v)$ then equation 6.10 becomes:

$$\hat{F}(u,v) = \frac{G(u,v)}{H(u,v)} \tag{6.11}$$

It is now possible to obtain an estimate of $f(y,z)$ by inverse transforming 6.11:

$$\hat{f}(y,z) = \mathcal{F}^{-1} \hat{F}(u,v) = \mathcal{F}^{-1} \frac{G(u,v)}{H(u,v)} \quad 6.12$$

where \mathcal{F}^{-1} is the sign of the inverse Fourier transform.

This restoration method is called the INVERSE FILTER [12]. It has to be stressed here that $\hat{f}(y,z)$ is an approximation to the original energy distribution $f(y,z)$. An assessment of the approximation, although it cannot be exactly evaluated, it can however be estimated by considering two main factors. First, if the signal to noise ratio is big enough to allow for the implementation of this restoration procedure and second how well the newly defined point spread function will fit the real point spread function of the image formation system.

It has been shown that the Poisson noise contribution is the square root of the measurement (paragraph 5.2.1). The average measurement, in counts received per pixel cell in the matrix of an image, is about 1000 counts. Thus the signal to noise ratio is:

$$\frac{N}{\sqrt{N}} = \sqrt{N}$$

and expressed in decibels :

$$\text{SNR} = 10 \cdot \log(\sqrt{1000})^2 = 10 \cdot \log 1000 = 30\text{dB}.$$

This is a high SNR and it facilitates the implementation of this restoration method [27].

Unlike the noise level consideration, it is not possible to calculate or determine a number which will describe the approximation of the PSF to the real PSF of the system. This approximation, however, can be assessed by varying the different constants in equation 5.10, which describes the point spread function, and judging the quality of the enhanced image.

Equation 5.10 is repeated here for convenience:

$$h(y,z) = \frac{C_2}{C_3} * \exp\left(-\frac{y^2+z^2}{2C_3}\right) \quad 6.13$$

Quotient $\frac{C_2}{C_3}$ determines the amplitude of the function and describes its shape. To visualize the effect of the constants on the function we will consider the one dimensional case, thus:

$$h(x) = \frac{C_2}{C_3} * \exp\left(-\frac{x^2}{2C_3}\right) \text{ for } x^2 \leq D$$

and

$$h(x) = \frac{C_2}{C_3^2} * \exp\left(-\frac{D^2}{2C_3^2}\right) \text{ for } x^2 > D$$

Figure 6.2 shows a plot of the Gaussian shaped $h(x)$ versus x . The smaller the value of C_3 the sharper the descent of the curve.

The interactive facility of the Department's PDP-11/10 computer system has facilitated greatly the 'trial and error' method to determine values for C_2 , C_3 , and D (20., 1.5, 10. respectively) and thus enhance the images appropriately.

6.1.3 Practical Implementation

The original images were provided in 64X64 matrices. Their transformation into the spatial frequency domain and inversely into the space domain was achieved by the use of a Fast Fourier Transform algorithm. This is an algorithm which reduces considerably the amount of calculations that the direct Fourier Transform requires. There is an adequate documentation of the FFT algorithm in reference [15]. The computer program of the one dimensional radix-2 FFT which is given in this reference was employed, with a minor modification which proved beneficial in that it saved about 50% of the time which would have otherwise

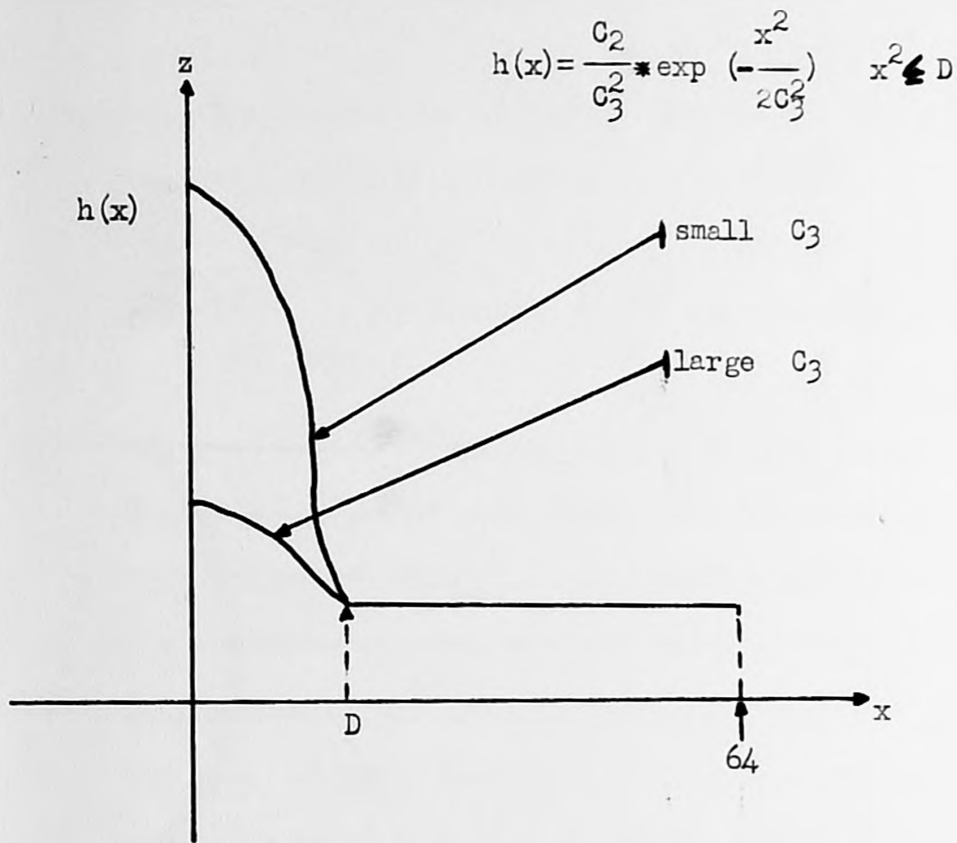


Figure 6.2

Plot of the one-dimensional point spread function

taken for the algorithm to transform the two-dimensional 64X64 image. This modification consisted of storing the sines and cosines in two vector arrays and using them as 'look up' tables during the operation of the algorithm.

The computation of the two-dimensional FFT was achieved as follows. Equation 6.7 can be rewritten as:

$$G(u,v) = \sum_{y=1}^N \sum_{z=1}^N g(y,z) \exp\left[-\frac{j2\pi}{N}yu\right] * \exp\left[-\frac{j2\pi}{N}zv\right] \quad 6.15$$

Equation 6.15 indicates that the two-dimensional FT can be computed as two sequential one-dimensional transforms, because the transform kernels are separate and symmetric. Thus the FT's of the rows of the image matrix were transformed first, and then the rows of the resulting matrix were transformed to give the composite two-dimensional FT of the image. The inverse FT was computed similarly. It takes about 50 seconds for the PDP-11/10 to transform a 64X64 image.

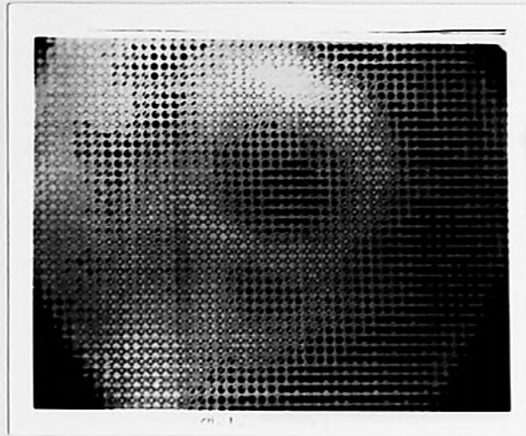
The dimensions of the image matrix made the implementation of the restoration algorithm difficult. The 24K storage capability of the PDP-11/10 system could not accommodate the two 64X64 complex arrays necessary to store the FT's of the image and the PSF. This problem was overcome by the usage of the floppy disc store facility. The FT of the PSF was precalculated and stored. That was a sound operation since, once the constants

Chapter 6

which characterize the PSF were determined for optimum image restoration, the FT of the PSF was unique for all gamma images. Then the division in the spatial domain, described by equation 6.11, was performed by reading a row at a time of the Modulation Transfer function from the floppy disc and processing it with the corresponding row of the image. Despite all these constraints the restoration algorithm worked satisfactorily consuming about four minutes for a complete 'deblurring' of a 64X64 image.

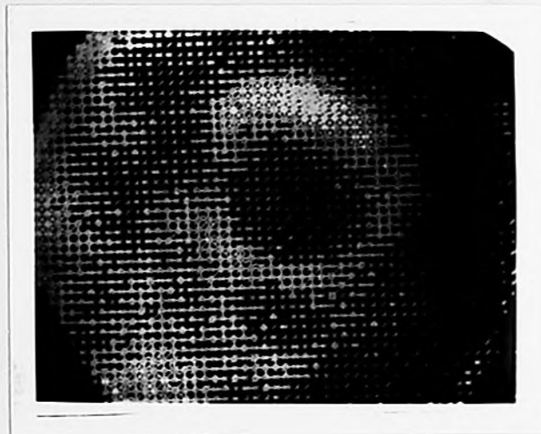
Figure 6.3(a) shows the Left Lateral Oblique (LAO) view of a gated heart image and Figure 6.3(b) shows its deblurred version. Notice how well the boundaries of the restored image appear. Clearly the enhanced images present a considerable improvement over the original images. Although this enhancement was previously anticipated by the analysis made in 6.1.2, however it was the subjective judgement of the author that determined the optimum solution to the restoration problem. Thus any objective judgement on the restored images will be postponed for later chapters when the deblurring effect will be examined in relation to the three-dimensional reconstruction problem.

Figure 6.3
Gated Image.



(a)

Original Image of gated Left Lateral view
of myocardium.



(b)

Restored image of the image above

Figure 6.3
Gated Image.

6.2 ATTENUATION ELIMINATION

The elimination of the attenuation phenomena is a process which is closely related to the geometry of the radioisotope distribution in the object which forms the images, to the matter existing between the source of photon emission and the detecting camera, and to the distance between the source of emission and the detector. Unlike the case of photon scattering elimination (where it was easy to form a distortion function (PSF) variable only across the image and thus eliminate the scattering effect), in this case the formation of a distortion function for the attenuation phenomena would presuppose a knowledge of the isotope distribution in the original object. This realization makes the elimination of the attenuation phenomena impossible at this stage of the report. However, the effect of the photon attenuation will be explicitly examined in the next chapter as part of the reconstruction algorithm where it will be eliminated adequately.

6.3 NOISE ELIMINATION

The Poisson noise contribution due to the random nature of the radioactive emission was adequately dealt with in the previous chapter. Two of its characteristic merits were stressed in particular: it is signal dependent and its magnitude is small. The latter was particularly emphasized by the good quality of the enhanced images in 6.1.3, where the restoration method did not attempt to compensate for the distortion due to Poisson noise.

In literature there is a filtering method [28] which attempts to eliminate the noise effect from gamma images with relative success. The large computer storage required and the time consumed by this method do not comply with the requirements and constraints of the present research.

However, the noise contribution is dealt with in the next chapter as part of the three-dimensional reconstruction process, where a more effective procedure is developed for its elimination.

6.4 BOUNDARY DETECTION AND IMAGE PREPARATION

The reconstruction algorithms, which are described in the next chapter, attempt to reconstruct slices of radioisotope density distribution of a three-dimensional object from a small number of projected images. This implies that the projection of the object within each of the received images has to be appropriately collected and then these extracted projections will have to be correlated. In this way each extracted image projection can be divided into thin parallel 'lanes', where each lane signifies the projected image of a slice of the three-dimensional object, and then the appropriate lanes from the different images, signifying the image projections at different angles of a particular slice of the object, can be collected for insertion into the reconstruction algorithm.

Each gamma image consists of the object-projection and the background image. The object-projection extraction can be considered as a problem of finding the boundaries between the object projection and the background. Boundaries therefore will be those regions in the gamma image which separate the object-projection from the background. Boundary detection will be the process of finding an ordered set of points S_1 , which is a subset of all the points in the image S , such that every element in S_1 has a certain property P which qualifies it as a boundary point. The most popular properties P , which have been used by many workers in the field of biomedical engineering in developing boundary detection methods, are the

following: (a) Image intensities near a boundary change faster than in other regions in the image, and (b) Boundaries are located between two regions of higher and lower intensities. In the first case boundaries can be determined by applying spatial differentiations, while in the second case thresholding techniques are more appropriate.

However, it is generally recognised that the boundary detection problem is one of the most difficult, since gamma images are, comparatively, highly degraded. There have been several attempts of boundary detection in radiographic images, with reasonable success, but they have proved uneconomic both in computer storage and time consumption. The complexity of the problem is such that it has been proved impossible, so far, to develop a general method of boundary detection which could be applied successfully to all radiographic images.

Hence, the development of a boundary detection technique, which would satisfy all the time and storage constraints imposed in this work, will have to incorporate as much a priori information as possible and probably the 'operator's intervention'. The development of such a technique is also a function of the clarity of the images. Thus a boundary detection method developed for the cone images would be inappropriate for detecting the boundaries of the heart images, since the resolution in the latter is much lower than in the former. The loss in generality of such a method is not of great concern, since the requirement is to examine the same object

Chapter 6

(i.e the heart) routinely. Even if small variations in the projected images occur in different myocardium studies, due to differences in the size of the heart between patients, then through the 'operator's intervention' the boundary detecting algorithm could easily be adjusted interactively to accomodate for these variations.

Two different boundary detection techniques were developed, one suitable for tracing the boundaries of the cone image and one for locating the myocardium image in the heart images. The cone-detection technique is described in chapter 8 and the myocardium-detecting technique is described in chapter 9. Both methods accomodated the correlation of the images received at different projection angles and for stacking together the relevant data prior to entering the reconstruction algorithm.

7 RECONSTRUCTION ALGORITHMS

This chapter describes two different versions of an algorithm, the Straight Pseudoinverse (SP) and the Minimum Least Square Estimate (MLSE), for reconstructing the radioisotope density distribution in a three-dimensional object from a small number of projected gamma images. A thick walled hollow cone constructed from perspex glass was used to assist in the development and practical implementation of the reconstruction methods. The walls of the cone were filled with a solution of radioactive Technetium-99m. Four cone-images were collected by an Anger camera with its collimators perpendicular to the axis of symmetry of the cone. For computational simplicity the cone will be assumed to be divided into slices perpendicular to its axis of symmetry and the radioisotope density distribution will be recovered by reconstructing each slice separately.

This procedure of 'transverse slice-reconstructions' has been adopted by most available reconstruction algorithms. As was shown in Chapter 6, it is now possible to apply this procedure, since the scattering effect has already been eliminated from the images.

Generally, every reconstruction algorithm is developed for a specific application. Most applications introduce certain conditions and constraints, which influence, sometimes seriously, the design and field of operation of the particular algorithm. In biomedical applications these limitations are introduced by the equipment employed

for imaging and processing, by the particular organ of the human body under examination, and by the procedure followed for patient examination. Certain researchers have attempted to overcome these limitations by the construction of sophisticated equipment for imaging and processing, with relative success, but their methods have proved expensive both in purchase and maintenance.

Likewise, the present application poses a number of limitations which will form the guidelines in the design of the software of this work. The algorithm that reconstructs the radioisotope density distribution in the heart muscle has to operate automatically with minimum intervention from the operator and has to be simple in its structure and implementation. It must compensate adequately for the serious degradations introduced by the physical processes in the gamma photon emission, and for attenuation and Poisson noise effects. The algorithm must ensure the good quality of the reconstructed images so that it can assist greatly in the diagnosis of defunct muscle. Obviously, the method has to improve drastically the diagnostic ability of the operator over the existing technique of evaluating lesions by working statistically on the 'raw' received images. The whole reconstruction procedure has to be fast to facilitate the routine patient examination. It takes about ten minutes for an Anger camera image to be recorded, thus the algorithm must require a small number of gamma images, preferably those views of the heart which are presently used for routine patient examination at Guys. Finally, the algorithm has to be compatible with the PDP-11/40 minicomputer system, which poses limitations in core storage (24K) and in processing speed.

Chapter 7

Unfortunately, the system does not incorporate 'floating point arithmetic' hardware, which would reduce the processing time considerably. Additionally, gating the Anger camera to the patient's heart beat, to remove image degradation due to heart motion, is undesirable. The time consumed to prepare the patient for gating and for proper images to be recorded, introduces a serious delay in the whole procedure of patient examination. It is also uncomfortable for the patient to remain motionless for long periods of time.

Thus, the particular application poses many limitations, some of them serious, rendering the reconstruction problem difficult. It is unavoidable that to tackle the problem efficiently and to overcome the difficulties it introduces, the algorithm will have to lose its generality (to reconstruct any organ in the human body) and be more specific in reconstructing the human heart, using as much apriori information as possible (e.g. geometry of heart etc.) Most of the existing reconstruction algorithms would be inapplicable in the present work.

7.1 DESCRIPTION

The method which is proposed in this section assumes that the scattering phenomena have been adequately eliminated and that the projected images are formed by parallel non-overlapping rays. It takes advantage of the symmetry of the object under consideration by assuming similarity in the projected images at different angles around its axis of symmetry. Indeed, a degree of similarity in the collected images can be achieved, when the Anger camera rotates in a plane which is perpendicular to the axis of symmetry of the cone and the camera is rotated at a constant distance from this axis. Any differences amongst the received images will be attributed to the Poisson noise effect.

Figure 7.1 shows a slice cut off the cone by a plane perpendicular to the cone's axis of symmetry. The slice is considered to consist of cells of equal finite magnitude. If the wall of the cone is filled with a solution of radioactive ^{99m}Tc , and considering the slice of Figure 7.2, each cell will contain an equal amount of radioisotope and thus emit an equal amount of radiation towards the x-direction in a given time interval. An Anger camera situated in the same direction, with its plane of collimators perpendicular to the emitted rays, will register the oncoming photons and thus form an image, which will correspond to the projection of the slice onto the plane of the collimators.

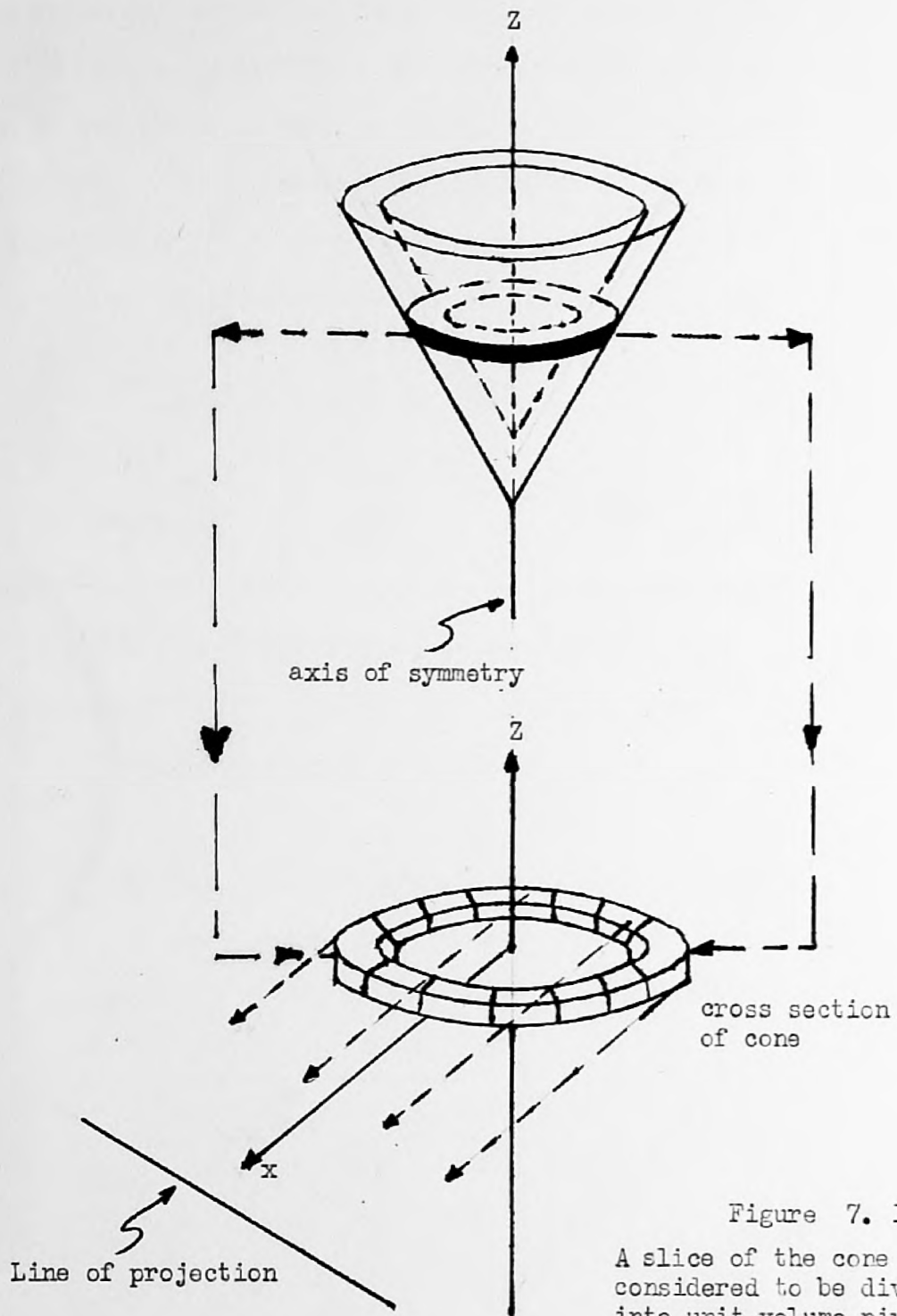


Figure 7. I

A slice of the cone is considered to be divided into unit volume pixels

Figure 7.2 shows the shape of the projection for parallel non-overlapping rays. This projection should be approximately the same in any direction due to symmetry. Any differences in the projections will be due to the Poisson effect. The projection sum of a particular ray K , signified by the amplitude of the projection curve at the 'foot' of the ray, is expressed as follows:

$$P_{k,\theta} = \left[\sum_{l \in \text{ray}[k,\theta]} A_{k,\theta,l} * I_l * C_{\theta,l} \right] + v_{k,\theta} \quad 7.1$$

where:

$P_{k,\theta}$ is the projection sum of the ray $[k,\theta]$ at a projection angle θ .

$A_{k,\theta,l}$ is the fractional area of the cell which is cut by the ray $[k,\theta]$

I_l is the radioisotope distribution in the cell

$C_{\theta,l}$ is the attenuation term which when expressed explicitly gives:

$$C_{\theta,l} = \frac{\exp\left(-\sum_{i=1}^N \mu_i d_i\right)}{4R^2}$$

and

$$R = \sum_{i=1}^N d_i$$

7.2

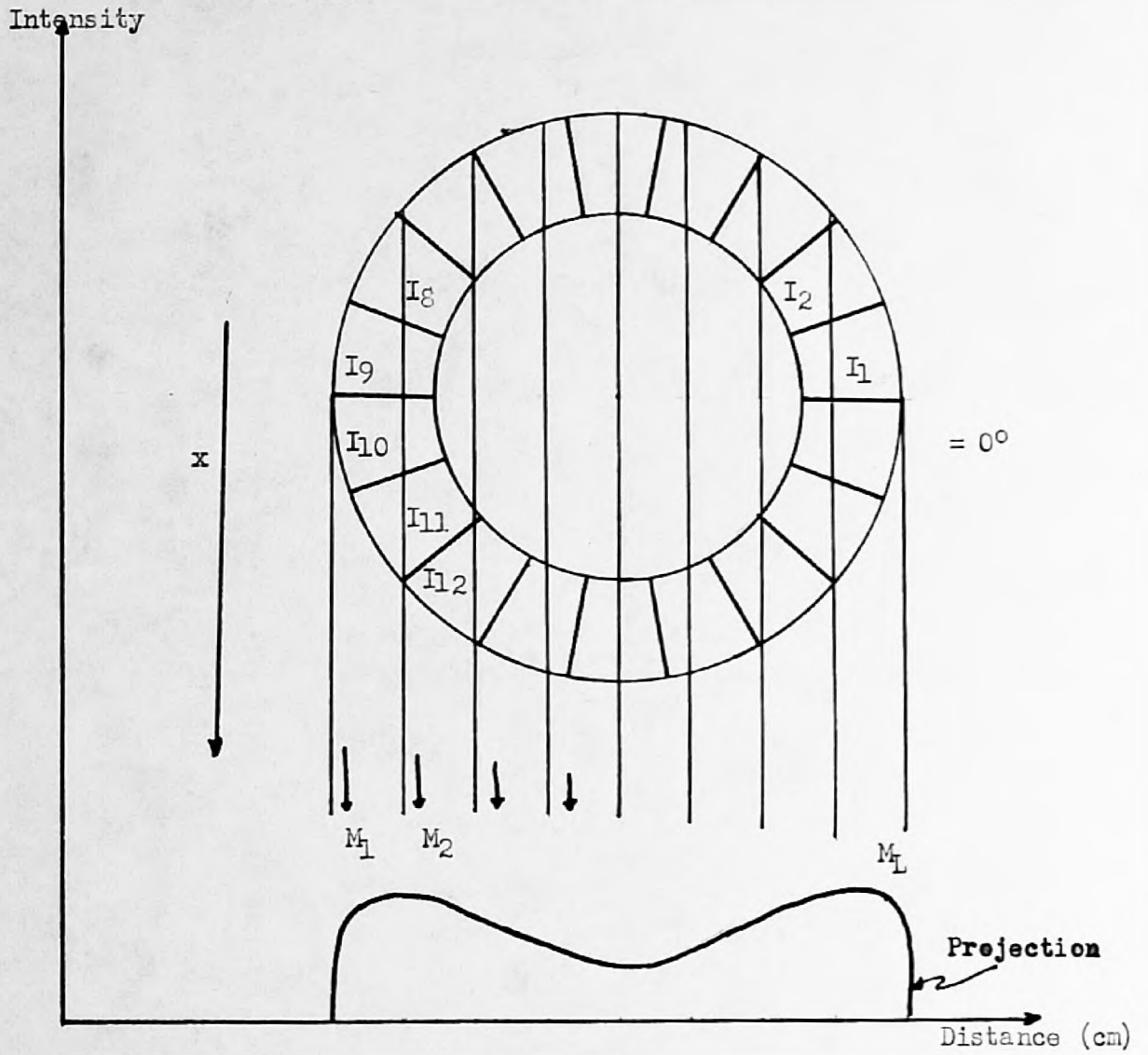


Figure 7.2
The process of image formation by projection

Chapter 7

where: R is the distance of the centre of the fractional area of the pixel from the collimator plane of the camera

μ_i are the attenuation coefficients in the different media

d_i are the distances travelled by the photons before reaching the collimator plane

v is the Poisson noise term.

k, θ

It is evident from equation 7.1 that a series of equations can be formed to describe the projected image of the slice in a particular direction :

$$P_{[1,\theta]} = \left[\sum_{1 \in [1,\theta]} A_{1,\theta,1} * I_1 * C_{\theta,1} \right] + v_{[1,\theta]}$$

$$P_{[2,\theta]} = \left[\sum_{1 \in [2,\theta]} A_{2,\theta,1} * I_1 * C_{\theta,1} \right] + v_{[2,\theta]}$$

⋮

$$P_{[n,\theta]} = \left[\sum_{1 \in [n,\theta]} A_{n,\theta,1} * I_1 * C_{\theta,1} \right] + v_{[n,\theta]}$$

7.3

For the particular application of Figure 7.2, the set of equations describing the projection of the slice at $\theta=0$ are as follows:

$$P_1 = C_{1,11} * A_{1,11} * I_{11} + C_{1,10} * A_{1,10} * I_{10} + C_{1,9} * A_{1,9} * I_9 + C_{1,8} * A_{1,8} * I_8 + v_1$$

⋮

$$P_n = C_{n,LL} * A_{n,LL} * I_{LL} + C_{n,L} * A_{n,L} * I_L + C_{n,1} * A_{n,1} * I_1 + C_{n,2} * A_{n,2} * I_2 + v_n$$

7.4

where, $LL=L-1$

From equations 7.4 and from Figure 7.2 it is evident that any attempt to recover the I's will be unsuccessful, since there are fewer equations than unknowns, rendering the system underdetermined.

If, however, three more projections are obtained by moving the Anger camera at 30,60,90, degrees from its first position and in the same horizontal plane, equations 7.4 now become:

$$\begin{bmatrix} P_1 \\ \vdots \\ P_k \\ \vdots \\ P_{4n} \end{bmatrix} = \begin{bmatrix} F_{1,1} & F_{1,2} & \cdots & F_{1,L} \\ \vdots & \vdots & & \vdots \\ F_{k,1} & F_{k,2} & \cdots & F_{k,L} \\ \vdots & \vdots & & \vdots \\ F_{4n,1} & F_{4n,2} & \cdots & F_{4n,L} \end{bmatrix} \begin{bmatrix} I_1 \\ \vdots \\ I_L \end{bmatrix} + \begin{bmatrix} v_1 \\ \vdots \\ v_k \\ \vdots \\ v_{4n} \end{bmatrix} \quad 7.5$$

where $F(i,j) = C(i,j) \cdot A(i,j)$ for $i=1,2,\dots,4n$ and $j=1,2,\dots,L$ or using matrix notation:

$$P = F \cdot I + NN \quad 7.6$$

where P is (NX1) matrix, and F(NXL), I(LX1), NN (NX1) and $N=4n$, $N > L$.

The main objective is to solve for I, the radioisotope distribution in the walls of the slice of the cone. Equation 7.6 is overdetermined but because of noise the system is not completely consistent. Thus a minimum squared error solution is required, which minimises this inconsistency, i.e. minimise $\{(P-FI)^2\}$ [53]. The solution is provided by the matrix pseudoinverse or generalised inverse technique, which is examined in the next sections of this chapter.

Chapter 7

Before attempting to solve for I , it is necessary to describe the method by which matrix F was calculated.

7.1.1 Practical Implementation

This algorithm calculates the fractional areas cut by each ray $A(i,j)$, calculates the attenuation factor for each fractional area $C(i,j)$, for four different angles of projection and for the slices of the cone. The rotation of the camera around the cone, when the data were recorded, was anti-clockwise in direction, at equal distances from the axis of symmetry of the cone and in a plane perpendicular to this axis. The algorithm assumes the camera fixed and the cone rotating at equal 30-degree intervals in a clockwise direction around its axis of symmetry. Clearly, this consideration is equivalent to the real case and it has been introduced for simplicity.

Analytically, the algorithm performs the following steps:

1. Reads from store the projection data corresponding to a particular slice. Four projections of the slice are read, which were previously selected and appropriately stacked together by the boundary detection routine.
2. It correlates the selected data to a slice along the axis of the cone, whose dimensions are known exactly. Thus, it calculates the radius of the slice (in centimetres) and divides its radioactive area in small pixels each of area 1 square centimetre.
3. For each pixel, finds the axes that cut through it and calculates the fractional areas $A(i,j)$ which belong to

Chapter 7

each ray. Two axes constitute one ray.

4. For each fractional area calculates the attenuation factors $C(i,j)$ by calling subroutine ATTEN, described later in this section.
5. Stores the result of $A(i,j)*C(i,j)$ in an array $F(NxL)$, where $N=4*$ the number of rays and $L=$ number of pixels.
6. Processes the next pixel through steps 3 to 6, until all pixels have been accounted for.
7. Rotates the slice around its axis through 30 degrees in a clockwise direction and repeats steps 3 to 7, until the slice is turned through 90 degrees.
8. Repeats steps 1 to 7 for all the slices and stores the results in a floppy disc.

Subroutine ATTEN was developed to determine the attenuation factors $C(i,j)$ for each fractional area. Figure 7.3 shows the path of a photon emitted from one such fractional area before reaching the face of the camera. Subroutine ATTEN performs the following steps:

1. Finds the coordinates of the centre of the fractional area.
2. Calculates the distance d from the camera's face.
3. Determines the distances travelled in radioisotope, perspex glass, and air d_1, d_2, d_3 respectively.
4. Computes the attenuation factor using equations 7.2

$$\text{i.e. } C_{i,j} = \frac{1}{4\pi d^2} * \exp(-(d_1 * ACW + d_2 * ACP + d_3 * ACA)) \quad 7.7$$

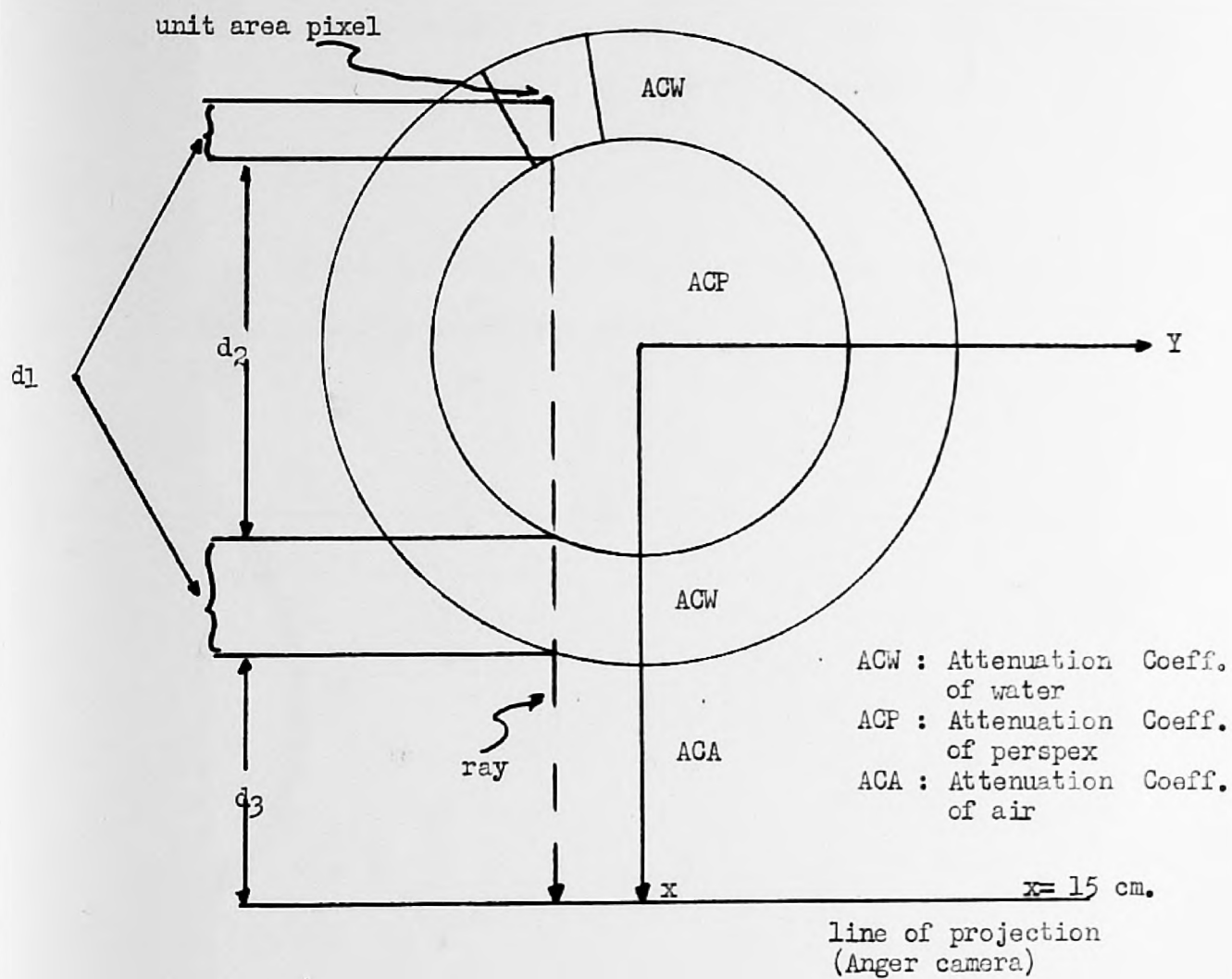


Figure 7.3

Calculation of distances travelled by a photon in different media before reaching the projection line.

Chapter 7

where $d=d_1+d_2+d_3$

and ACW, ACP, ACA are the attenuation coefficients for water, perspex glass, and air respectively ($ACW=0.15$, $ACP=0.15$, $ACA=0.13$ in $1/cm$ units for $99m-Tc$).

Figure 7.4 shows a flowchart of the algorithm which calculates the fractional areas.

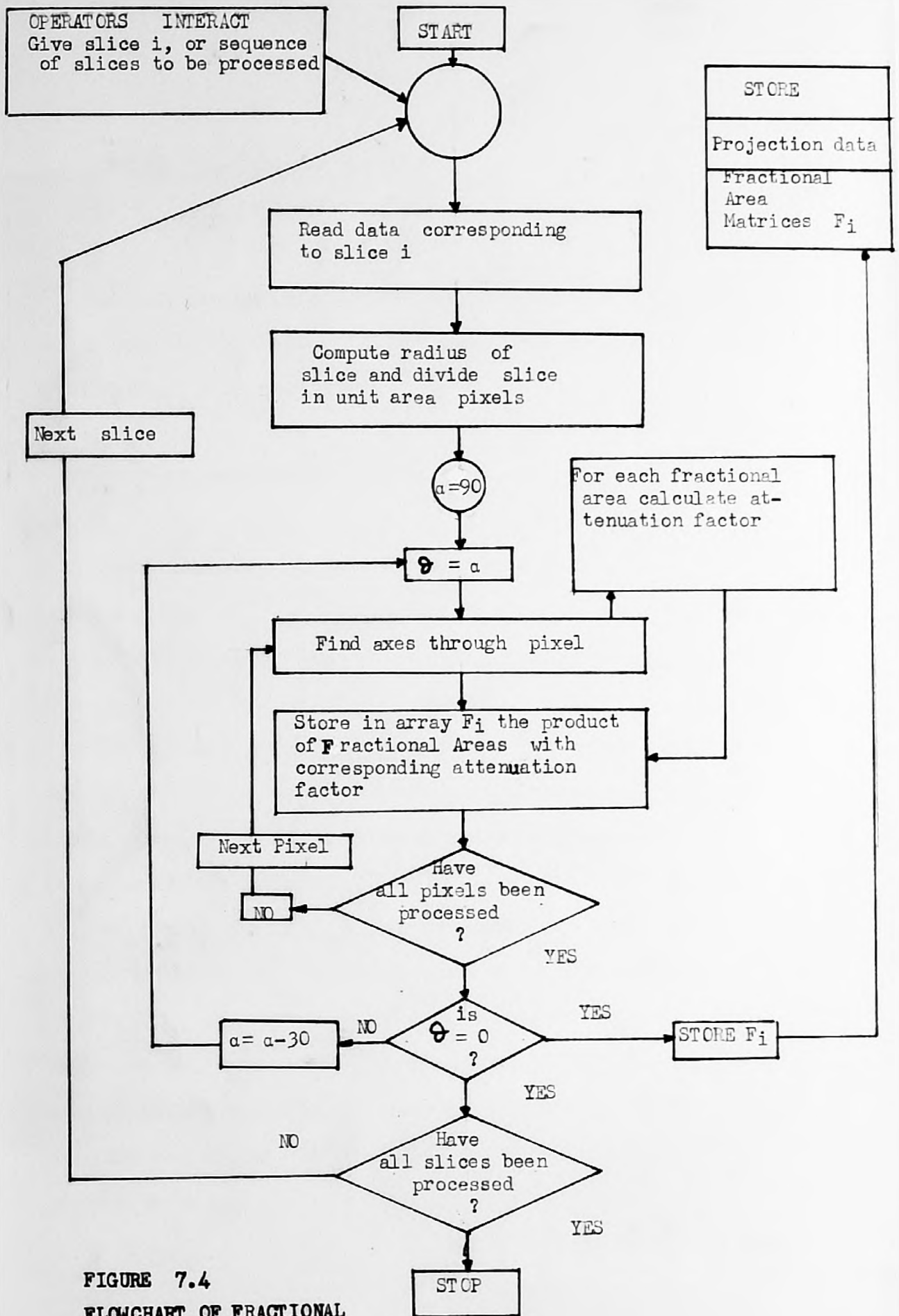


FIGURE 7.4
FLOWCHART OF FRACTIONAL
AREAS - ALGORITHM

7.2 STRAIGHT PSEUDOINVERSE METHOD

In this section an algorithm is developed that attempts to solve equation 7.6 w.r.t I, the radioisotope density distribution. From equation 7.6:

$$B = (P - NN) = FI \quad 7.8$$

The simple solution for 7.8 would have been:

$$I = F^{-1} B \quad 7.9$$

where B is a column matrix (Nx1) and F^{-1} is the inverse of F. But matrix F is not square (NxL, N>L) and its inverse does not exist. Even if the number of equations were to be chosen equal to the number of unknowns, i.e N=L, matrix F would still be irreversible or singular, since it is highly probable that the system equations are not independent and thus the determinant of F is zero [2]. Even if the inverse of the square matrix F could be computed, the uncertainty of the solution would increase, since a smaller number of projected images would have to be used. Thus, matrix F will be considered in its full dimensions (NxL, N>L) in any attempt to solve 7.8.

Chapter 7

7.2.1 The Generalized Inverse or Pseudoinverse

A square matrix A of dimensions $(n \times n)$ which is nonsingular has a unique inverse A^{-1} of dimensions $(n \times n)$ such that $AA^{-1} = A^{-1}A = I$, where I is the unit matrix. In general a matrix has no inverse if:

1. It is square $(n \times n)$ and its determinant is zero.
2. It is rectangular $(n \times m)$ with $n \neq m$.

In the physical systems, and in particular in the image formation systems, the nature of matrix F in the general equation $F\underline{x} = \underline{b}$ is usually singular. The seemingly intractable problem was adequately tackled by Penrose in 1954 [29], when he proved that for any matrix F of dimensions $(N \times L, N > L)$ there is a Generalised inverse Z which is unique and satisfies the following conditions:

Chapter 7

$$FZF=F$$

$$ZFZ=Z$$

$$(FZ)^T = FZ$$

$$(ZF)^T = ZF$$

7.10

where T denotes the transpose operation.

Penrose also proved [30] that if Z is the Generalised inverse of F then Zb gives the unique and best approximate solution to the inconsistent system $Fx=b$.

The calculation of matrix Z, given the matrix F, is achieved by decomposing matrix F into a product of matrices, using the singular value decomposition (SVD) method, and then using a suitable product combination of these matrices to calculate Z. Thus if $F=UTD^T$, the Generalised inverse is given by:

$$Z=DSU^T$$

7.11

where,

S: is (rXr) diagonal, r being the rank of F, with diagonal elements $1/v_1, 1/v_2, 1/v_3, \dots, 1/v_r$, where $v_1, v_2, v_3, \dots, v_r$, are the positive square roots of the eigenvalues of FF^T and $v_1 > v_2 > v_3 > \dots > v_r$.

D: is (lXr) consisting of the orthonormalised eigenvectors of $F^T F$.

U: is (NXr) consisting of the orthonormalised

Chapter 7

eigenvectors of FF^T .

Z: is (LxN) the Generalised inverse of F(LxN).

T: is (rxr) diagonal, with diagonal elements v_1, v_2, \dots, v_r .

Appendix {III} gives a full account of the singular value decomposition method and derives equation 7.11 from first principles as well as proves its uniqueness.

In the case of a non-singular square matrix A(nXn) matrices U and D are constructed by the eigenvectors of A and A^T respectively, the diagonal of matrix T consists of the \underline{n} eigenvalues of A, and Z is the inverse A^{-1} of A.

The Generalised inverse or pseudoinverse is a function of the geometry of the object under examination, of the imaging system, and of the photon attenuation.

7.2.2 Description of the SP-Algorithm

The decomposition of matrix F, in equation $B=FI$, into three submatrices as described in the previous paragraph, is best achieved by an efficient method due to Golub and Reinsch [16]. In short this method uses Householder transformations[31,16] to reduce F to bidiagonal form and then the QR algorithm [31] to find the singular values of the bidiagonal matrix. The

decomposition of F is obtained by the proper combination of these two phases. This is called the SVD method (Singular Value Decomposition). The SVD method gives the most reliable determination of the rank r of matrix F and computes the singular values with good accuracy. Fortunately, this type of decomposition is included in the NAG Subroutines Library. It was properly modified to reduce array storage, and then it was included in the reconstruction algorithms. The SVD subroutine on exit gives the matrices U and D^T , and the square roots of the non-negative eigenvalues (or singular values) of $F^T F$, $v_1, v_2, v_3, \dots, v_r$, and $v_{r+1} = v_{r+2} = \dots = v_L$. The eigenvalues, however, may not be ordered, as required by the inequality relation $v_1 > v_2 > \dots > v_r$. A sorting subroutine was constructed which orders the singular values and constructs the diagonal matrix S in equation 7.11. It also shuffles the relevant columns of the matrices U and D^T accordingly. The SVD routine performs its computations within a given tolerance, which is specified by the user and is a function of the machine precision. When some of the singular values become very small it is difficult to distinguish them from the zero singular values. Again some of the truly zero singular values may attain very small positive values. To overcome this problem, which may lead to serious errors, a routine was constructed to check the correctness of the SVD routine, which performs the following steps:

1. A threshold level is set to separate the positive from the zero singular values.
2. In the equation $B=FI$ a solution is assumed I and a

Chapter 7

new B' is calculated next.

3. The generalised inverse of F , Z , is next computed using the SVD method and the formulation of equation 7.11.
4. Using $ZB'=I'$ vector I' is computed.
5. If $I=I'$ the SVD method has worked satisfactorily.
6. If $I \neq I'$ the threshold level is lowered to the level of the next smallest singular value so that the rank \underline{r} is increased by one.
7. Repeats steps 2 to 7.

The application of this routine to a large number of matrices F , corresponding to the different slices of the cone, revealed that for threshold level of 10^{-6} the SVD method works satisfactorily.

When the correctness of the SVD is verified, the matrices U and D^T are transposed and the generalised inverse Z is computed from relation 7.11. The matrix product ZB is calculated next and the results are plotted on a Tektronix screen.

Summarising, the SP algorithm performs the following steps:

1. For a particular slice, indicated by the operator, reads F and B from a floppy disk.
2. Decomposes F using the SVD routine.
3. Orders the singular values in a descending order, forms diagonal matrix S in equation 7.11, and shuffles the

Chapter 7

columns of U and D^T accordingly.

4. Checks the correctness of the SVD routine.
5. Computes the generalised inverse Z from equation 7.11
6. Evaluates the product ZB .
7. Plots the result on the TK-screen by stacking the reconstructed slices together.
8. Repeats steps 1 to 8 until all slices are processed.

Figure 7.5 gives the flowchart of the Straight Pseudoinverse reconstruction algorithm.

7.2.3 Minimum Least Square Estimate method (MLSE)

It was shown in the previous paragraphs that ZB gives the best solution to the system of inconsistent equations $B=FI$, where Z is the generalised inverse of the matrix F . The inconsistency of the system is largely due to the Poisson noise contribution, and also due to errors arising from the imaging system, and from the inaccuracies involved in the assumptions made in the image restoration and reconstruction algorithms. If the system of equations is ill-conditioned its numerical solution becomes difficult, since small errors in B and F may lead to large errors in the solution of vector I .

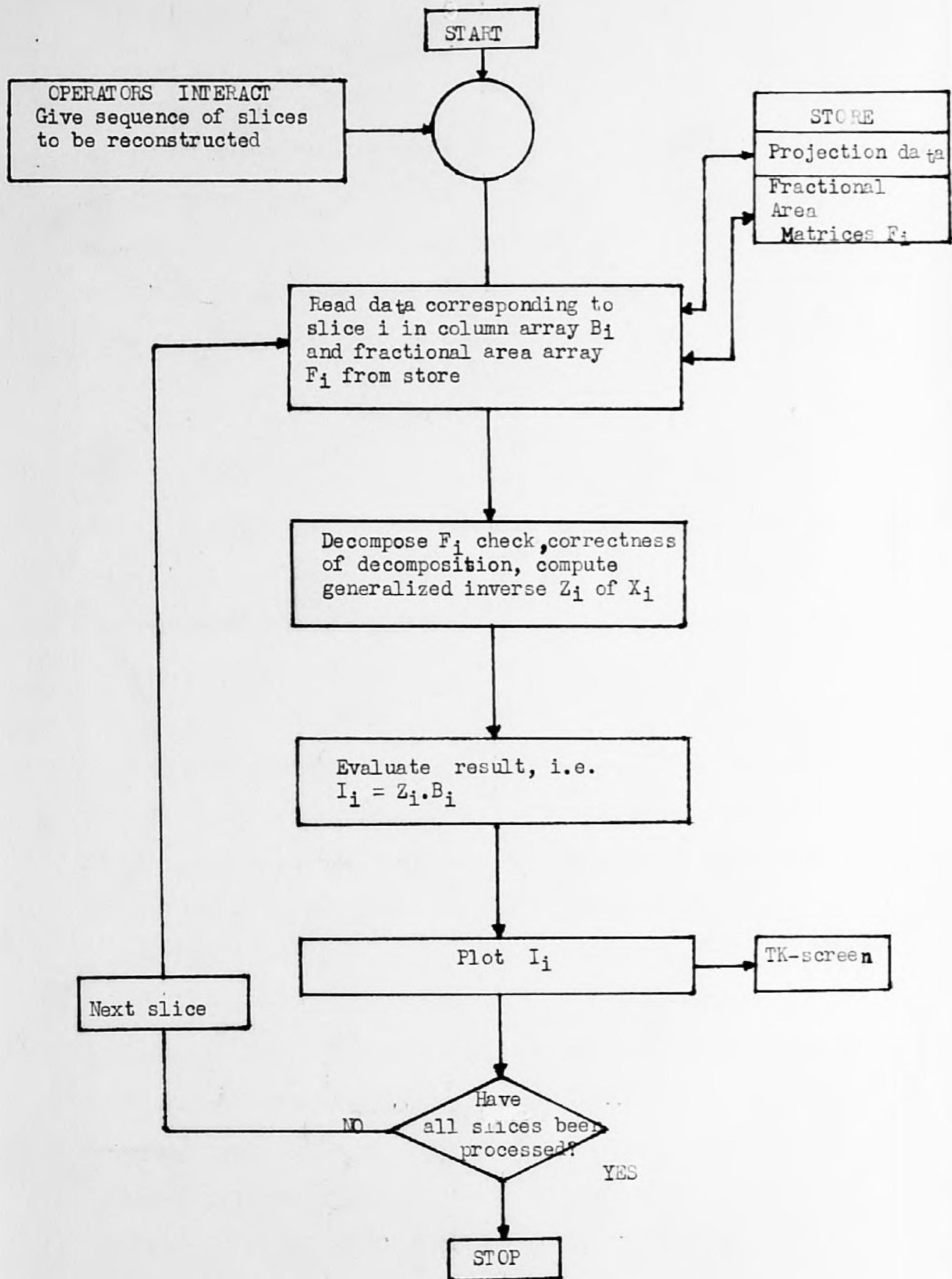


FIGURE 7.5
FLOWCHART OF THE SP- ALGORITHM

Thus, whether the system of equations is ill-conditioned or not, provision has to be taken to ensure, first a realizable solution and second an 'optimum' solution. This can be achieved by forming a criterion function and requiring the best solution I' to be a minimum to this function. The criterion function is:

$$S(I) = \sum_{i=1}^N \left[\frac{B_i \sum_{j=1}^L f_{i,j} * I_j}{B_i^{1/2}} \right]^2 \quad 7.12$$

where, $\sum_{j=1}^L f_{i,j} I_j$ represents the projection that would have been formed with attenuation effects incorporated in $f_{i,j}$, and B_i represents the measured projection after scattering has been removed.

If it is assumed that the predominant source of distortion, at this stage of the report, is the Poisson noise contribution, then the difference in the numerator of 7.12 represents the Poisson noise contribution for each measurement. It has been proved (see 5.2.1) that an estimate of the magnitude of the noise is the square root of the measurement B_i . The square of the quotient of these two terms will form the least square function of 7.12, which when minimised with respect to I , will reveal the 'optimum' best solution I' . Thus, the formulation of 7.12 eliminates the Poisson noise effect and provides a solution I' which is better than the solution suggested by $I=ZB$.

7.2.4 Mathematical derivation of the MLSE method

Using matrix notation equation 7.12 can be represented as:

$$S(I) = (B - FI)^T D (B - FI) \quad 7.13$$

where D is a diagonal matrix whose elements are $1/B_i$, $i=1,2,\dots,N$

If ∇_I is the matrix differential operator then

$$\nabla_I S(I)|_{I'} = 0 \quad 7.14$$

where I' is the estimate that minimises 7.13

from 7.13 and 7.14

$$\begin{aligned} \nabla_I (B^T D B - B^T D F I - I^T F^T D B + I^T F^T D F I) \Big|_{I'} &= 0 \\ - B^T D F - F^T D B + I^T F^T D F + F^T D F I \Big|_{I'} &= 0 \\ (- F^T D B + F^T D F I) + (- F^T D B + F^T D F I) \Big|_{I'} &= 0 \end{aligned}$$

$$\text{Thus} \quad - F^T D B + F^T D F I \Big|_{I'} = 0$$

$$I' = (F^T D F)^{-1} F^T D B$$

$$\text{if} \quad Z = (F^T D F)^{-1} \quad 7.15$$

$$\text{then} \quad I' = Z F^T D B \quad 7.16$$

where Z is the generalised inverse of $F^T D F$, F^T is an $(L \times N)$ matrix ($N > L$), D is an $N \times N$ diagonal matrix, B is $N \times 1$ matrix and Z is an $L \times L$ matrix considerably smaller than Z ($L \times N$) in $I = ZB$.

7.2.5 Description of the MLSE-Algorithm

The MLSE algorithm was designed in accordance with the expression for the optimum best estimate I' given by equation 7.16. Similarly to the SP algorithm provision will be taken to safeguard the correct calculation of the generalised inverse Z in equation 7.15. One encouraging fact is that here, the matrix to be pseudoinverted is square and dimensionally smaller than the corresponding matrix in the SP-algorithm, thus the time taken for the calculation of the pseudoinverse is reduced. The square property of the matrix does not insure its non-singularity (in which case the SVD routine converges rapidly) but on the contrary there is a big chance that the matrix would be singular. Thus, all the procedures for safeguarding the correct calculation of the generalised inverse are implemented in the MLSE-algorithm in exactly the same way that they were used for the SP-algorithm.

The MLSE-algorithm performs the following steps:

1. For a particular slice, indicated by the operator, reads matrices F and B , stored in the floppy disc.
2. Forms the diagonal matrix D , with diagonal elements the elements of the column matrix B , i.e $D=\{B_i, i=1,2,\dots,N\}$.
3. Computes matrix $X=F^T D F$
4. Decomposes matrix X and checks the correctness of the SVD routine by performing steps similar to 2,3,4 of the

Chapter 7

SP-algorithm.

5. Computes the generalised inverse Z of X from equation 7.11.
6. Evaluates the product $ZF^T DB$ to obtain the optimum best solution I' .
7. Plots the result on a TK-screen by stacking the reconstructed slices on top of each other.
8. Repeats steps 1 to 8 until all slices are processed.

Figure 7.6 gives a flowchart of the MLSE-algorithm.

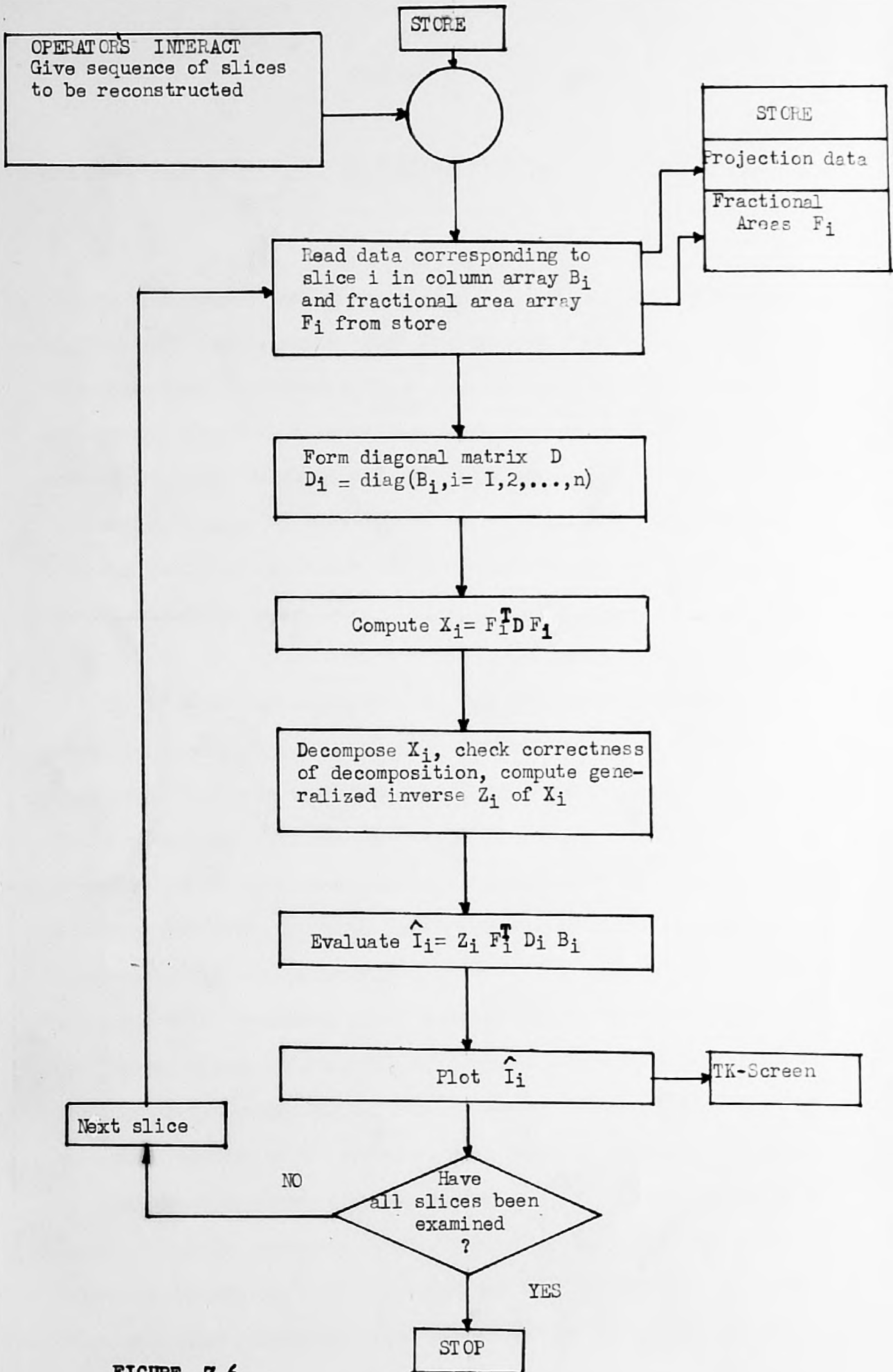


FIGURE 7.6
FLOWCHART OF THE MLSE - ALGORITHM

7.3 COMPARISON BETWEEN SP AND MLSE ALGORITHMS.

In this chapter two reconstruction algorithms were developed, the Straight Pseudoinverse and the Minimum Least Square Estimate. Both algorithms were designed to reconstruct a hollow symmetric object from four of its projected gamma images, and both algorithms used the singular value decomposition procedure in reconstructing consecutive slices of the object. Both algorithms compensated for photon attenuation, with the MLSE algorithm attempting to eliminate the Poisson noise as well.

The SP-algorithm is simpler in its structure but more time consuming, since it attempts to pseudoinvert larger matrices. Evidently, the SP-method requires larger core space, a crucial factor given the limited 24K core memory of the PDP-11/10. If the objective of the work is to repeat the reconstruction of the same object a multiple of times, each time following the same scanning and image collection procedures, then the SP-algorithm becomes fast and less core demanding. In this case the generalised inverse of each slice need be calculated only once and stored in a floppy disc. Thus the SP-algorithm reduces to a simple matrix multiplication procedure, whereby the generalised inverse Z of a particular slice is recalled from store to be multiplied by the corresponding data vector B , which contains the projected images of the slice at different directions, and thus reveal the reconstructed slice. Under the same objective, the MLSE-algorithm is at a disadvantage

Chapter 7

over the SP-algorithm, since the matrix to be pseudoinverted has to be computed each time a new set of images is collected.

The SP-algorithm provides a solution, which is the unique best approximate solution to the system of linear inconsistent equations $FI=B$. The MLSE-algorithm attempts to eliminate the inconsistency of the equations, largely due to Poisson noise, and gives the 'optimum' best solution to the linear system of equations. Evidently, it provides the best solution of the two algorithms and ensures a realizable answer under ill-conditioned circumstances.

Finally, in passing a judgement into the suitability of the two algorithms, the reconstruction problem has to be seen in perspective with its objective and constraints. For example, it has been proved that the Poisson noise contribution is small rendering the system of non-linear equations $FI=B$ mildly inconsistent. Under normal system behaviour (no ill-conditioning), and considering the objective-repetitive reconstruction of the same object from sets of images obtained by the same procedure- the SP-algorithm is more effective because it reconstructs quickly, requires low storage, and provides good reconstructed images. Obviously, the best way to compare the effectiveness of the two algorithms is to judge them on their results. Thus, a final judgement is postponed until the cone and the human heart are successfully reconstructed.

8 CONE PHANTOM RECONSTRUCTION EXPERIMENT

This Chapter discusses the first and necessary step for the validation of the reconstruction algorithms. The main objective of this step is to demonstrate the ability of the two reconstruction algorithms to recover the distribution of radioactive material in the walls of a cone phantom and compare their effectiveness when operating within the constraints imposed by routine application in medical diagnosis.

This experimental work will assist us to evaluate the quality of the reconstructed images produced by the two algorithms, will help provide an understanding of the nature of the system (e.g. is it ill-conditioned?), and finally will provide a starting point from which to tackle successfully the more difficult task of the reconstruction of the human heart.

This experiment will also help us to assess the extent of distortion that the attenuation, scattering and Poisson noise phenomena cause in the recorded gamma images, by examining the quality of the reconstructed images when some or all the distortions have been eliminated. At the same time the effectiveness of the algorithms in eliminating these distortions will be revealed.

Chapter 8

Additionally, this preliminary experimentation, by bridging the gap between the theoretical development and practical application of the two algorithms, will enable us to correct them adequately and shape them efficiently so that their operation will be optimised.

Finally, this work will help the author to attain adequate expertise in image handling and processing, a necessary tool before attempting to deal with human hearts.

For all these reasons it was thought necessary at the time to approximate the human heart by a thick walled hollow cone, simulate dead muscle tissue by a rubber wedge, which would be inserted at a known position in the walls of the cone, and attempt to reconstruct the radioisotope distribution in the walls of the cone so that the position of the rubber wedge would be clearly revealed in the reconstructed images.

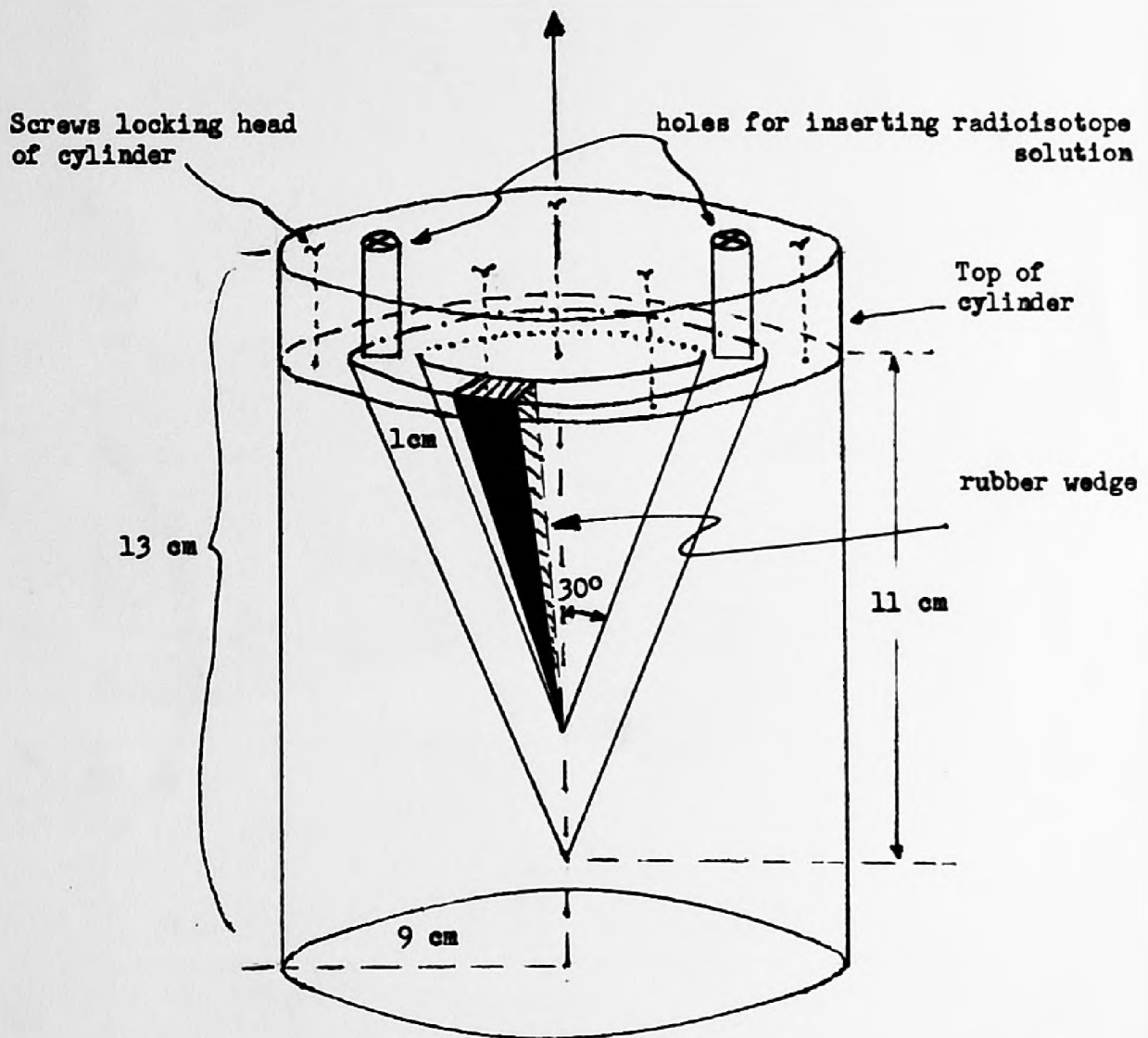


Figure 8.1
Conical cavity in cylindrical perspex block.



Figure 8.2
The cone phantom.

Chapter 8

8.1 THE CONE

For the experimental implementation of this work, a conical cavity was cut concentrically in a solid cylindrical block of perspex glass as shown in Figure 8.1. The cavity thickness was 1cm, the cone's altitude was 11cm, and the cone's angle was 30 degrees. The cylinder's height was 13.6cm and its radius 9cm. The top of the cylinder unscrews to allow access to the conical cavity so that a rubber wedge can be inserted at particular position to fit the cavity tightly, thus ensuring no accumulation of radioactive fluid in that area. Two diametrically opposite screws at the top of the cylinder would cover firmly two holes, which were drilled to allow the insertion of the radioactive solution in the conical cavity. Figure 8.2 shows the conical construction.

The conical cavity was filled with a solution of ^{99m}Tc and scanned at Guys Hospital. The Anger camera was situated at about 15cm from the central axis of the cone and recorded four images at 30 degrees angular intervals. The rotation of the Anger camera was in a plane perpendicular to the axis of symmetry of the cone and its distance from this axis was kept constant.

The images were first recorded on 9-track magnetic tape but were then punched on paper tape to be transferred to our Department's PDP-11 computer system. This was a cumbersome procedure, but the only one available at the time, since the magnetic tape peripheral

Chapter 8

of the Department's PDP-11 system could only manage 7-track tapes.

8.2 IMAGE HANDLING.

Each cone image was provided by Guy's in a 64X64 matrix, in which the actual cone image was contained approximately within a 30X32 dimensional submatrix. This suggested that for computational efficiency (e.g. for radix-2 FFT's to be applicable) a 32X32 submatrix containing the cone image could be selected from each of the 64X64 matrices. This reduced the storage requirements by a factor of four (4) and speeded up considerably the inverse filtering procedure.

For this purpose an algorithm was developed, which moved interactively a 32X32 square frame across the 64X64 image. Thus the best 32X32 submatrix containing the cone image could be located and stored in a floppy disc. Figure 8.3 shows the four cone images, which were collected by the above procedure and plotted on the Tk-screen. Following an S-shaped path and starting from the bottom left image the four cone images correspond to 0,30,60,90 degrees of Anger camera rotation.

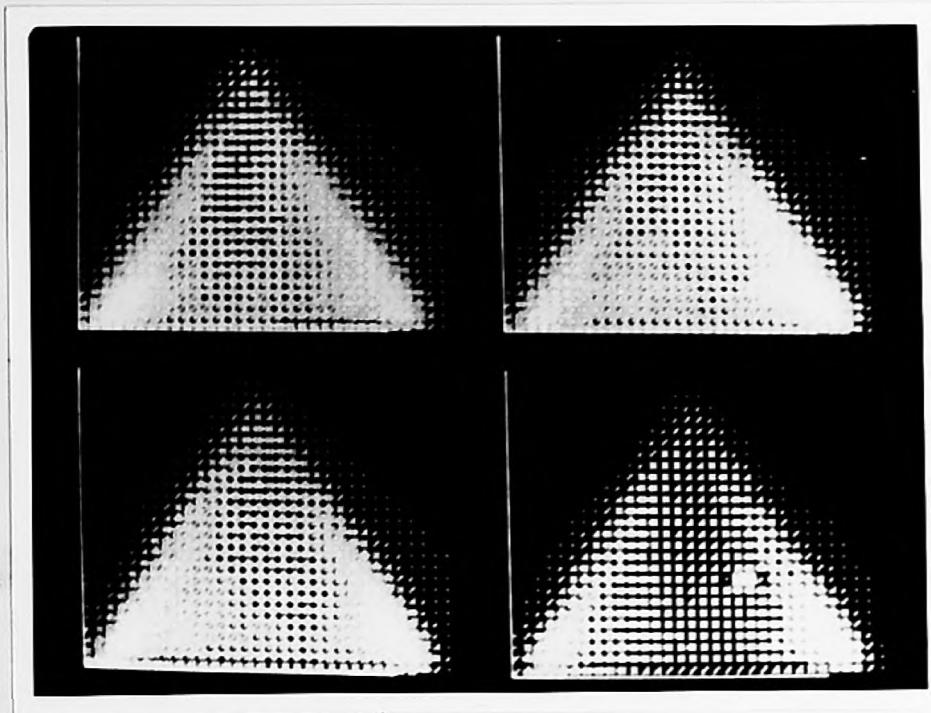


Figure 8.3

Cone phantom scintigrams.

8.2.1 Inverse Filtering

The inverse filtering algorithm was extensively described in Chapter 6. However its direct application to this case would be uneconomical, since there is a considerable reduction in the dimensionality of the arrays and the time consuming procedure of sequential reading from and writing to the floppy discs is unnecessary. The algorithm can be now modified so that the whole inverse filtering process can be contained in the same one filtering algorithm.

The inverse filtering algorithm performs the following steps.

1. Reads image matrix (32X32) from store and stores it in an array A(32X32).
2. Transforms A into the Fourier domain using 2-dimensional FFT and stores the results in a complex array CA(32X32).
3. Creates the Point Spread Function, as described by equation 6.13, transforms the result into the Fourier domain and stores the transformed matrix in complex array CS(32X32). If parameters C2, C3, and D in equation 6.13 are well established then this step can be replaced by simply reading from store complex array CS.
4. Performs the deconvolution in the spatial frequency domain by computing the quotient $CA(i,j) = CA(i,j) / CS(i,j)$, $i=1,2,\dots,32$, $j=1,2,\dots,32$.

Chapter 8

5. Transforms $CA(i,j)$ into the space domain using the 2-dimensional inverse FFT.
6. Stores in a floppy disc the result.
7. Plots on the Tk-screen the filtered image.

Figure 8.4 gives a flowchart of the inverse filtering algorithm.

The inverse filtering algorithm has worked satisfactorily, consuming about 1 minute of processing time per image. This time was recorded when in step 3 the FT of the PSF was read from the floppy disc. The constants C2, C3, and D, after the trial and error procedure had the same values as in chapter 6.

Figure 8.5 shows the four filtered versions of the cone images. Notably the blurring effect due to the imaging system's PSF has been adequately removed and the image boundaries are now well defined.

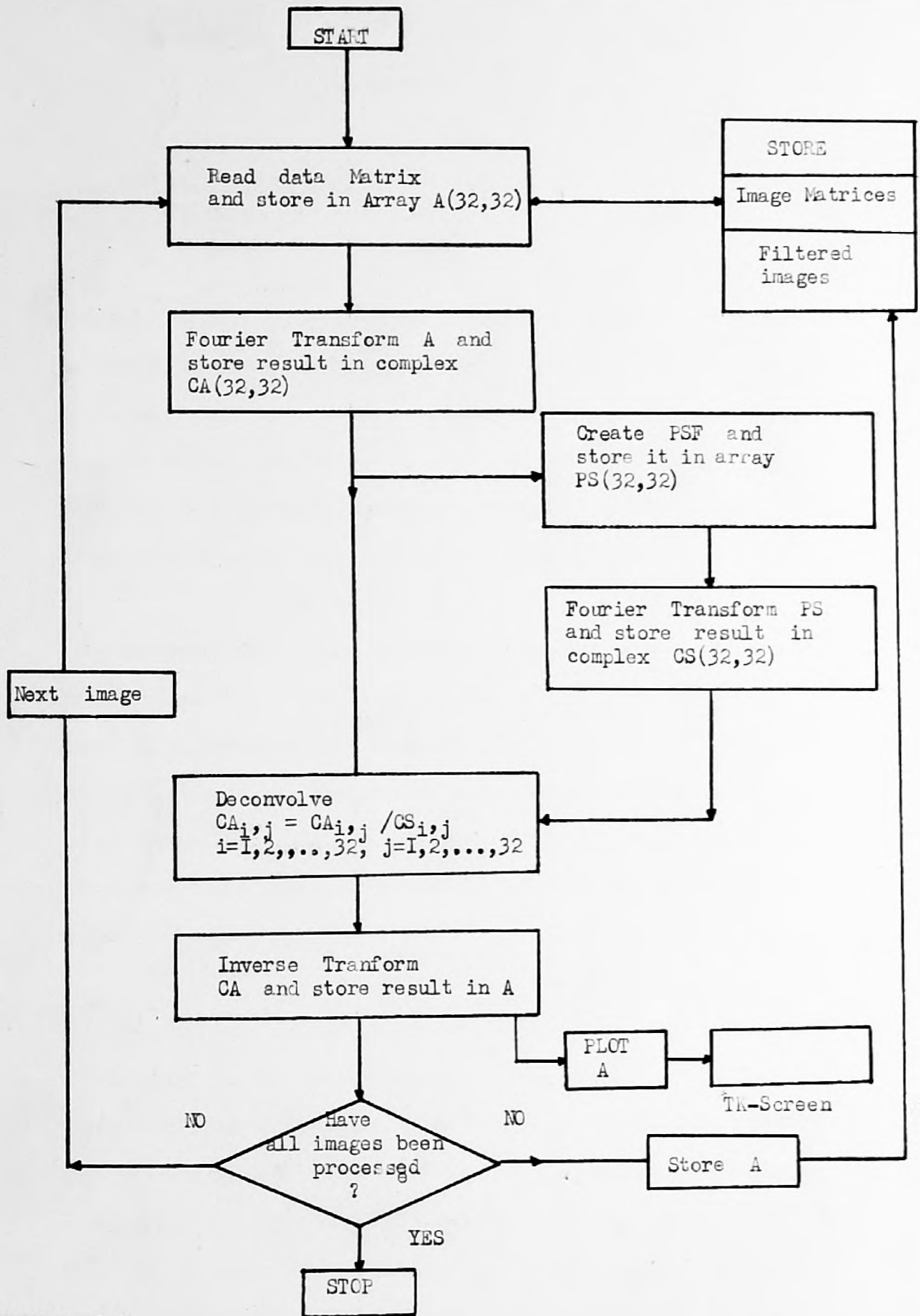


FIGURE 8.4
FLOWCHART OF INVERSE FILTERING ROUTINE

8.2.2 Boundary Detection

The boundary detection algorithm, which is developed in this paragraph, is based on the general principle that, in an image the intensities near a boundary change faster than in other regions. This principle is quite evident in the filtered images of Figure 5.8, where most of the background has been removed and the projected gamma image of the cone is well defined.

The main objectives of this algorithm are, first to correlate the four cone images as well as possible, second to construct a number of 'projection-sets', where each set contains the four images of a particular slice of the cone and where each 'slice-image' is suitably collected from its respective cone image, and third to estimate the edges or boundary points of each projection set.

The boundary detection problem was considerably simplified by ensuring, at the time of scanning, that the orientation of the collimator head of the Anger camera relative to the cone was such that the projected image of the axis of symmetry of the cone would coincide or be parallel to a column in the image matrix. Each row of the image matrix, or a set of rows, could now be easily interpreted as the image of the particular slice of the cone. Thus the first objectives of the boundary detection algorithm have already been met, since a careful observation of

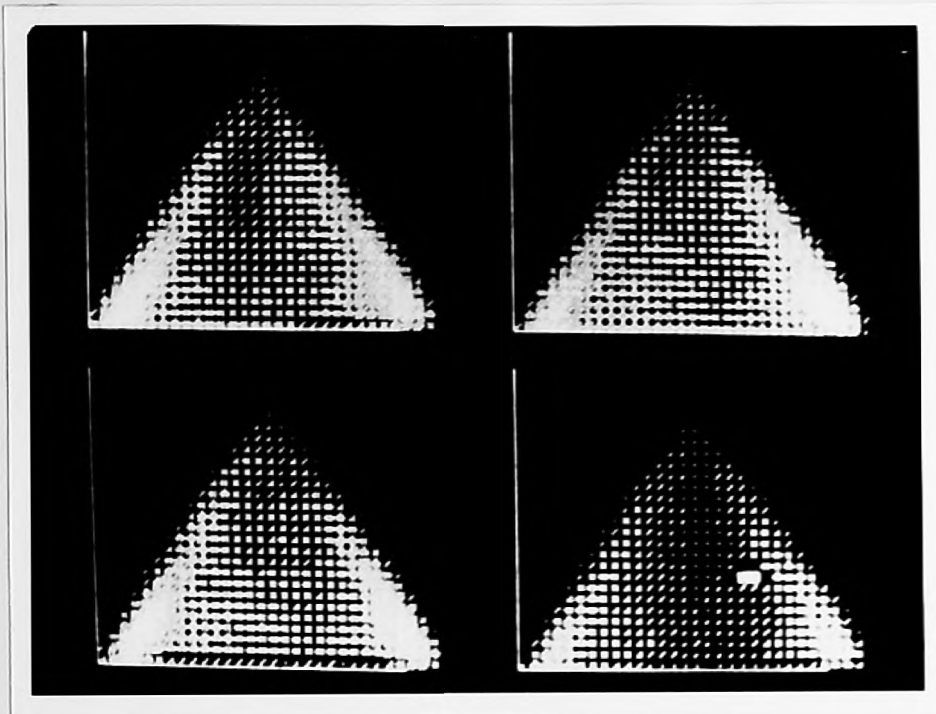


Figure 8.5 (a)
Filtered cone images.

the images of Figure 8.5 would reveal that, first the cone images are easily correlated (each consisting of 23 rows) and second the construction of the projection sets is a simple collection of relative rows from each image (e.g. set 10 would consist of the tenth row of each cone image).

To meet the third objective the following a priori information was taken under consideration. First, the slice images of each projection set should contain the same number of intensity elements or pixel cells, since the cone is symmetric and its images were collected with the Anger camera rotating in a plane perpendicular to its axis of symmetry. Second, the projection function has the general form indicated in Figure 8.5(b), where it is seen to peak near the boundary. This peaking may be approximated by a triangular function as indicated in Figure 8.5(b). Let us signify this feature as the edge behaviour. Finally, the boundary points should obey the boundary principle of steep intensity change in their vicinity and the image should be smooth. These principles will be applied by considering the spatial ratios of adjacent pixels at both ends of each slice-image and discarding those pixels whose ratio is larger than a set threshold value.

The algorithm will converge if all rows (slice-images) of each projection set contain the same number of elements (intensity-pixels). In case of non-convergence, four decision-criteria were used, which helped the algorithm to decide

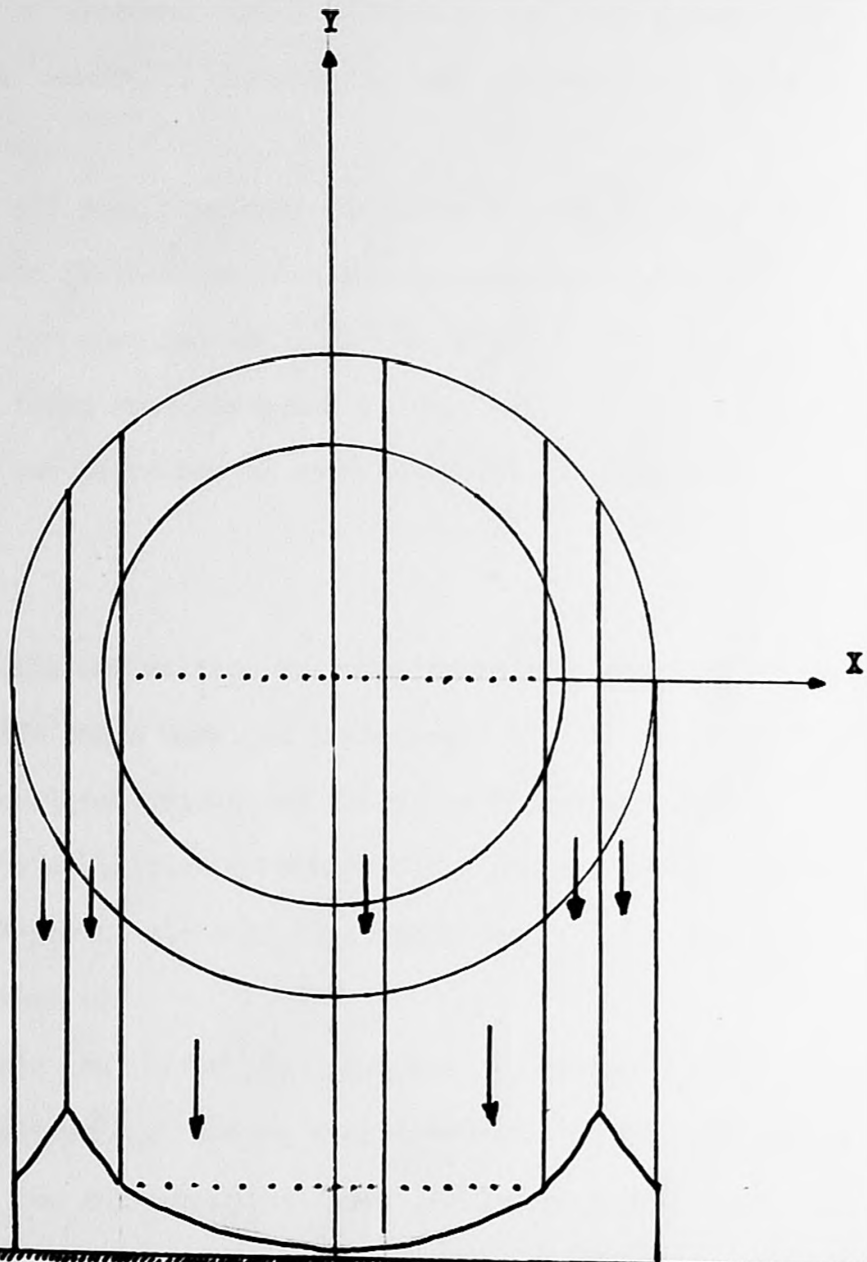


Figure 8.5(b)
Diagram indicating triangular
shape of projection at the
boundary.

on the number of elements that a particular set should have. Let k signify the number of elements in each row and K the decision number for a set.

1. If all four rows have different k , then K would take the value of that row with the intermediate value of k
2. If two rows had equal k , then $K=k$.
3. If three rows had equal k , then $K=k$.
4. If two pairs had k_1 and k_2 with $k_1 > k_2$, then $K=k_2$.

An algorithm was written which performs the following steps:

1. Reads image matrices from store.
2. Correlates images and forms the projection sets.
3. Sets an initial threshold value for the ratio between two adjacent elements in each row for a particular projection set.
4. Tests the ratios of adjacent elements against the threshold value, moving from both ends towards the centre of the row and stopping when ratios smaller than the threshold value appear first, thus defining new end elements for each row.
5. Tests the new edges for each row for edge-behaviour and stops when this appears.
6. If all rows have the same number of elements, the algorithm stores these rows and processes the next projection set repeating steps 3 to 6.
7. If the rows have different number of elements, the

threshold value is lowered by a constant factor and steps 3 to 7 are repeated, until a lower limit of threshold value is reached.

8. If there is no convergence, then a decision is made on the number of elements that the rows of the particular set should contain according to the four decision-criteria.

9. The algorithm adds an adequate number of elements to the rows that need modification, by choosing elements from both ends which have been previously discarded, or subtracts elements from them, so that each modified row correlates best to the 'correct' rows.

10. Stores projection set, and repeats steps 3 to 10 until all projection sets have been processed.

Figure 8.6 gives a flowchart of the boundary detection algorithm.

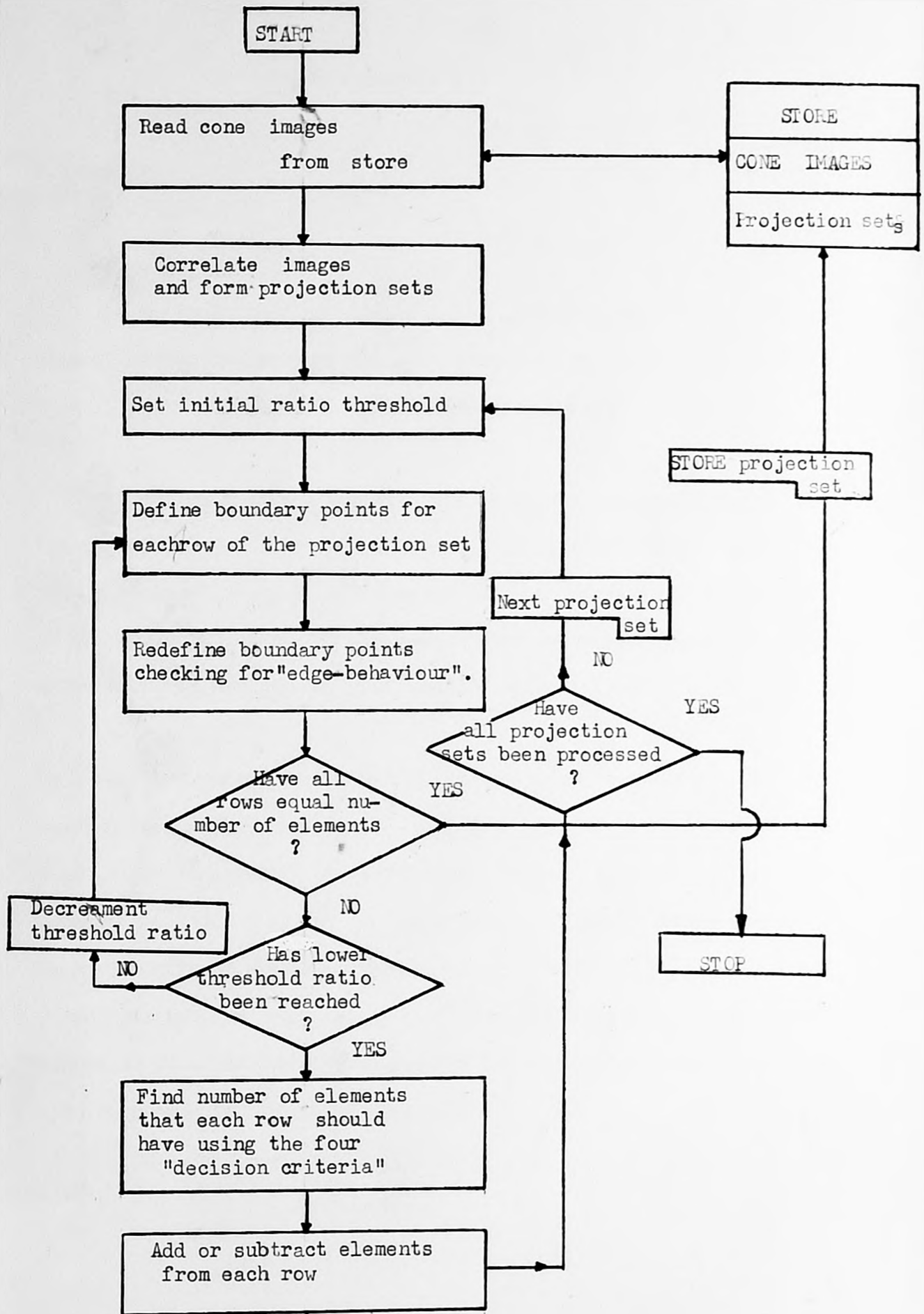


FIGURE 8.6
FLOWCHART OF THE BOUNDARY DETECTION METHOD

8.3 RESULTS

The manipulation of the cone's gamma images and their classification in projection sets according to cone slices, enable their direct insertion into the reconstruction algorithms.

The analysis of the results will be accomplished according to the objectives as stressed in the introduction of this chapter, so that a thorough insight in the properties of the imaging system can be obtained and necessary conclusions can be derived concerning the effects of the sources of image degradation.

For this purpose, the SP-algorithm will be employed first to examine the effectiveness in compensating for the scattering and attenuation phenomena. The MLSE-algorithm will be employed next to repeat the same series of experiments. These two series of three-dimensional reconstructions will facilitate a critical comparison between the two algorithms. The reconstructions will be displayed on a Tektronix 4006 storage display unit, using a halftone plot to obtain 25 levels of grey scale.

8.3.1 SP-Algorithm

Four reconstructions were produced using the SP-algorithm. Let us, for the sake of simplicity, denote by -PSF and +PSF that provision has been taken so that scattering phenomena have-not-been-eliminated and have-been-eliminated respectively in the reconstructed images. Similarly, let -ATT and +ATT denote that attenuation phenomena have-not-been-eliminated and have-been-eliminated respectively.

i) The effect of photon scattering.

Figure 8.7 shows the 3-dimensional reconstruction of the radioisotope distribution in the walls of the cone under -PSF and -ATT conditions. For this purpose, the original gamma images of Figure 8.3 were used by the boundary detection algorithm and then by the SP-algorithm. The reconstructed image represents the deployment of the radioisotope distribution in the cone's cavity onto a flat surface. It can be observed that the presence of the rubber wedge is non-existent in the resulting image or it could be argued optimistically that there is a faint suspicion of the wedge existing somewhere in the middle of the image. Under +PSF and -ATT conditions, where the filtered images of Figure 8.5 were used, the rubber wedge is clearly evident as seen in the reconstructed image of Figure 8.8. Comparing Figures 8.7 and 8.8 it is quite obvious that the quality of the reconstructed image

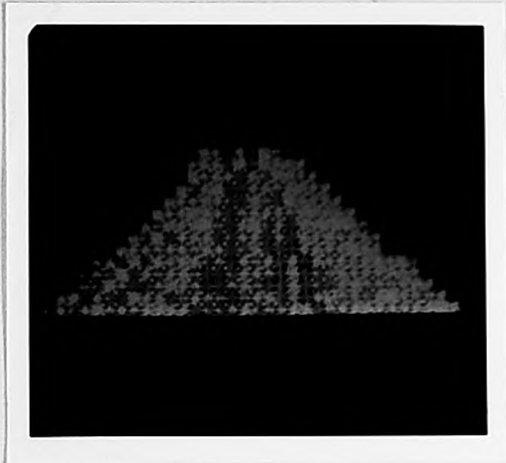


Figure 8.7
-PSF, -ATT

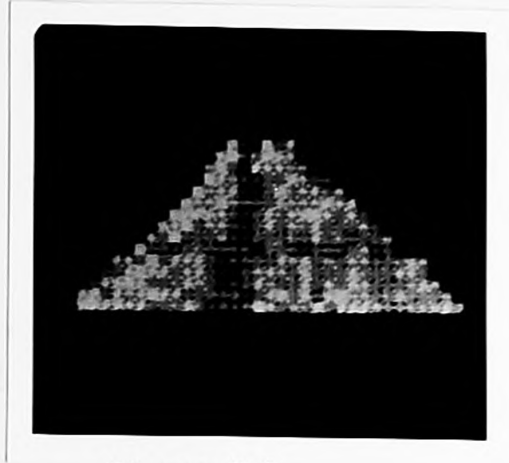


Figure 8.8
+PSF, -ATT

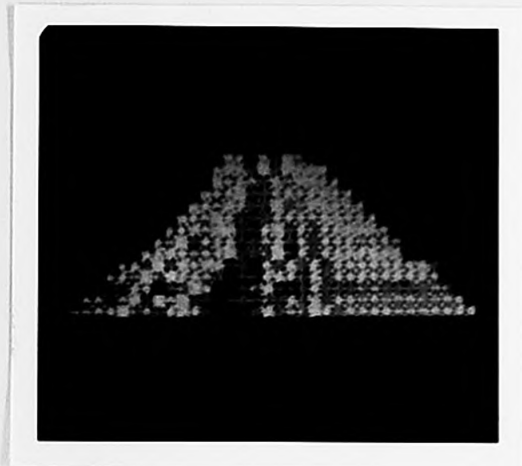


Figure 8.9
-PSF, +ATT

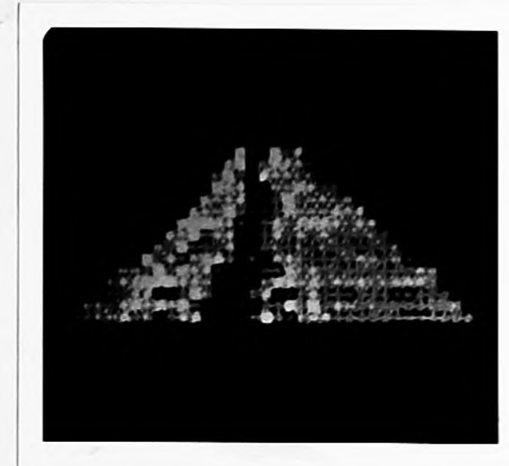


Figure 8.10
+PSF, +ATT

Figures 8.7-8.10

Cone reconstruction using the SP-algorithm.

PSF: signifies Point Spread Function

ATT: signifies Attenuation

+ : signifies elimination

- : signifies no correction

has been drastically improved by the use of the Inverse Filtering algorithm. This fact, that a 'faint suspicion' has turned into an 'absolute certainty' in determining the position of the rubber wedge, indicates clearly that the effect of photon scattering is a serious source of degradation and that the Inverse Filtering algorithm eliminates successfully and drastically the scattering effect. It must be mentioned here that the employment of a filtering technique prior to reconstruction has been disregarded by most researchers.

ii) The effect of photon attenuation.

To investigate the seriousness of the attenuation degradation a reconstruction was attempted under -PSF and +ATT conditions, shown in Figure 8.9.

A comparison between Figures (-PSF,-ATT) and 8.9 (-PSF,+ATT) clearly reveals that the degradation due to photon attenuation is again a serious source of distortion, since the existence of the wedge in the latter Figure is definitely observed.

Comparing Figures 8.8 (+PSF,-ATT) and 8.9 (-PSF,+ATT) it is evidently concluded, on the basis of wedge clarity, that photon scattering is a more serious source of degradation than photon attenuation (for the particular application) and that the elimination of the photon scattering alone (+PSF,-ATT) produces a better reconstruction than the elimination of the photon attenuation (-PSF,+ATT) alone.

iii) The combined effect of photon scattering
and
photon attenuation.

The last in the series of reconstructions, using the SP-algorithm, involved an attempt to reconstruct the radioisotope density distribution when both sources of image degradation were removed. Figure 8.10 represents the reconstruction under +PSF,+ATT conditions.

Evidently, the position of the rubber wedge is well defined and its clarity amplified. This is the best image obtained so far.

A number of conclusions can be formed in comparing this image with the rest. First, comparing it with Figure 8.7 (-PSF,-ATT) it is obvious that the effect of both sources of image distortion on the reconstructed image is devastating. Important detail is obscured rendering the reconstruction algorithm unreliable. It is thus necessary to consider both of the distortion eliminating routines as an integral part of the reconstruction algorithm. Second, comparing Figure 8.10 (+PSF,+ATT) with Figure 8.8 (+PSF,-ATT) it is realised that in Figure 8.8 there is an uncertainty in the definition of the boundaries of the wedge. If the dimensions of the wedge were small, it could easily create doubts in its identification. This fact is further stressed by the images of Figure 8.9 (-PSF,+ATT),

where the wedge boundaries are blurred. This image could easily obscure the existence of a dimensionally small wedge.

The above analysis highlights two important conclusions. The elimination of both photon attenuation and scattering is a necessary step for the successful operation of the reconstruction algorithm, and both algorithms of image distortion-elimination work satisfactorily in assisting the reconstruction algorithm to attain accuracy.

8.3.2 MLSE-Algorithm

The same series of experiments were repeated using the MLSE-algorithm. The reconstructed images are displayed in Figures 8.11-8.14. Using the same notation as in the previous paragraph Figure 8.11 is the reconstructed image by the MLSE-algorithm under -PSF,-ATT conditions, Figure 8.12 +PSF,-ATT, Figure 8.13 -PSF,+ATT, and Figure 8.14 +PSF,+ATT.

A careful examination of these images will reveal that exactly the same conclusions as in paragraph 8.3.1 can be derived when comparing these images amongst themselves. Again, it is shown that the attenuation and scattering phenomena cause serious degradations in the images and that their elimination constitutes a necessary step for a successful reconstruction by the

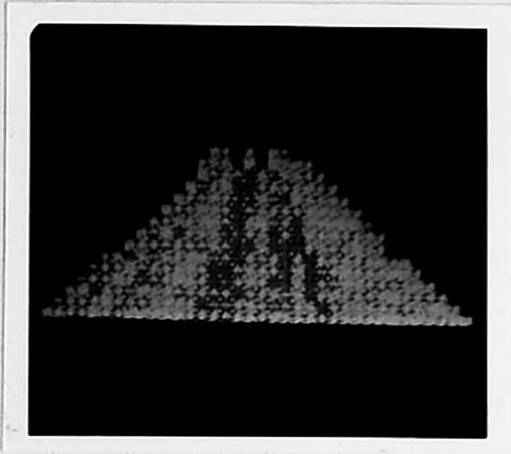


Figure 8.11
-PSF, -ATT

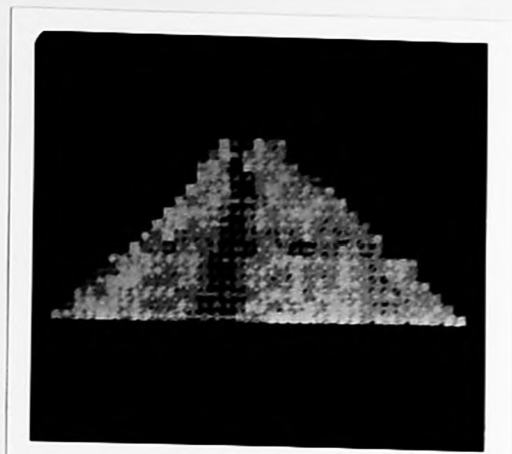


Figure 8.12
+PSF, -ATT

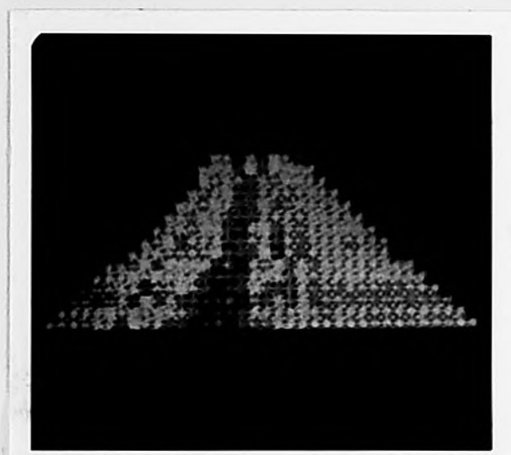


Figure 8.13
-PSF, +ATT

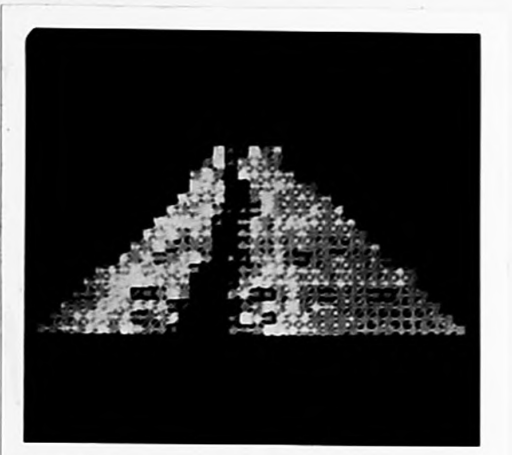


Figure 8.14
+PSF, +ATT

Figures 8.11-8.14

Cone reconstructions using the MLSE-algorithm.

PSF: signifies Point Spread Function

ATT: signifies Attenuation

+ : signifies elimination

- : signifies no correction

MLSE-algorithm.

8.4 CRITICAL COMPARISON

In this chapter two algorithms, the SP and MLSE, were described which reconstruct the radioisotope density distribution in the walls of the hollow cone from four gamma images projected at different angles. Both algorithms worked satisfactorily, revealing in the reconstructed images the position of the rubber wedge with certainty and precision (see Figures 8.10 and 8.14).

Both algorithms proved that photon attenuation and scattering introduce serious distortions in the received images and that they can effectively eliminate these distortions by the employment of two special routines -the Inverse Filtering and Attenuation eliminating routines- and thus reconstruct correctly the true radioisotope distribution.

Each algorithm was used to provide a series of reconstructed images under different conditions revealing similar images under each condition. This similarity is evident when the images of Figures 8.7-8.10 produced by the SP-algorithm are compared with the corresponding images of Figures 8.11-8.14 produced by the MLSE-algorithm. This similarity indicates that the nature of the imaging system is not ill-conditioned and verifies that the magnitude of the Poisson noise contribution is small, as it was estimated in paragraph 5.2.1. A closer comparison between the images of Figures 8.14 and 8.15, which represent the best

reconstructions obtained by the SP and MLSE algorithms respectively, will reveal that the MLSE method provides the best reconstructed image of the two, since in addition to displaying the wedge with clarity it produces a smoother solution in the rest of the reconstructed image. This realization is indicative of the fact that the MLSE-algorithm eliminates the uncertainty due to Poisson noise and thus produces an optimum best solution, as was claimed in section 7.4.

A straight comparison between the two algorithms reveals that, although the MLSE-method seems more powerful by producing a better image, it is the SP method that for our purpose -repetitive reconstruction of the same object following the image recording procedure- is the best compromise. It takes about forty five minutes for the MLSE-algorithm to reconstruct nineteen slices of the cone, while it takes about seven minutes for the SP-algorithm to perform the same reconstruction. This is because in the former case pseudoinverses have to be calculated every time a reconstruction of the same object takes place, while in the latter they are recalled from store. Additionally, the storage requirements for the SP-algorithm are not excessive, because the cone is a hollow object.

9 THREE-DIMENSIONAL HEART RECONSTRUCTION

This chapter describes the more powerful methods employed for the reconstruction of the Thallium-radioisotope density distribution in the left ventricle muscle tissue of the living heart. These were developed from algorithms originally devised for reconstructing cone phantoms, whose shape and location of the regions of inactivity were known exactly and which do not move.

The reconstruction of the living human heart presents many additional problems and our task is to extend the cone reconstruction algorithms to accommodate these, whilst remaining nevertheless within the time and storage constraints set by the Hospital. Introduction of some interaction into the reconstruction process is seen to be unavoidable.

Thus, our first target will be to manipulate the heart images appropriately prior to entering the reconstruction algorithm so that the heart reconstruction can be closely approximated to the cone reconstruction. Our second objective will be to evaluate the quality of the reconstructed images following a similar series of experimentations to the cone phantom reconstruction. Finally, the reconstruction algorithms will be tested on their ability to locate and identify heart muscle lesions in the myocardium. For this purpose, a healthy heart and an infarcted heart will be examined and the resulting reconstructed images will be compared.

9.1 DIFFICULTIES AND APPROXIMATIONS IN DATA ACQUISITION

AND 3-DIMENSIONAL RECONSTRUCTION

There are several problems arising in the acquisition of human heart images and the three-dimensional reconstruction of the heart. The human heart is an internal organ of the human body, which differs in size and orientation amongst humans. It is positioned at about 4cm inside the human chest and it performs a complicated periodic movement of translation and then rotation with subsequent change in its volume from diastole to systole. These characteristic peculiarities in the position and function of the human heart render the problem of image acquisition and three-dimensional reconstruction more difficult than the corresponding cone phantom experiment.

Efficient tackling of the problem, to comply with requirements of the reconstruction algorithms and the given constraints, involved a number of approximations, which naturally introduce errors in the whole process of reconstruction. First, the camera must record its image in a plane always parallel to the axis of symmetry of the heart. As this axis differs in direction amongst humans, its orientation has to be guessed, introducing a degree of uncertainty and a probable error. Second, the depth of the heart inside the chest cavity causes severe photon attenuation, thus necessitating, for reliable acquisition of good heart images, a close proximity of the Anger camera head to the chest wall. This and the physical

Chapter 9

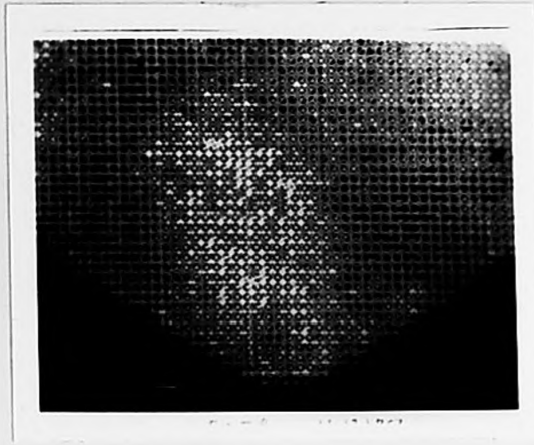
construction of the head of the Anger camera limit the arc of rotation of the camera in the required direction to forty degrees. Thus, only three images instead of four can be used for the heart reconstruction, taken at twenty degree intervals. Obviously, the limitation in the freedom of movement of the camera and in the number of images used for the reconstruction introduces an additional disadvantage in the 'reconstructing-ability' of the two algorithms. Third, the existence of the right ventricle, although relatively small in Thallium take-up, adds another distortion in the received gamma images. Fourth, the continuous movement of the heart and the spontaneous movement of the patient, who is constrained to about 30 minutes of motionless rest, result in a blurring of significant detail in the images. Fifth, significant Thallium take-up from other organs or flesh tissue in the human body contribute a background radiation-image in the received images. Finally, the position of the heart's projected image within the Anger camera image cannot be controlled very tightly, so the reconstruction package must be provided with algorithms to locate and orient the images automatically. This incorporates grid-rotation operations in the matrix-image, which involve interpolatory procedures introducing an additional factor of error.

Clearly, for all those reasons, it is unreasonable to hope for a reconstruction of the heart's left ventricle of the same quality and accuracy as in the cone experiment. It can however be stressed with certainty, as it is explained in the following paragraphs, that several problems can be solved, others can be evaluated so that it

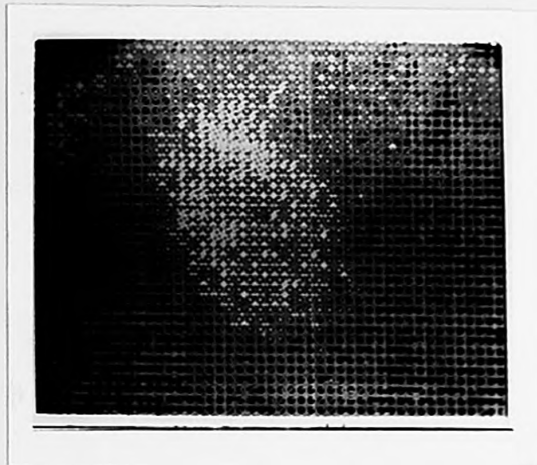
Chapter 9

can be finally claimed that a good reconstruction has been achieved, which satisfies all the constraints and is not greatly inferior to the quality of the cone reconstruction.

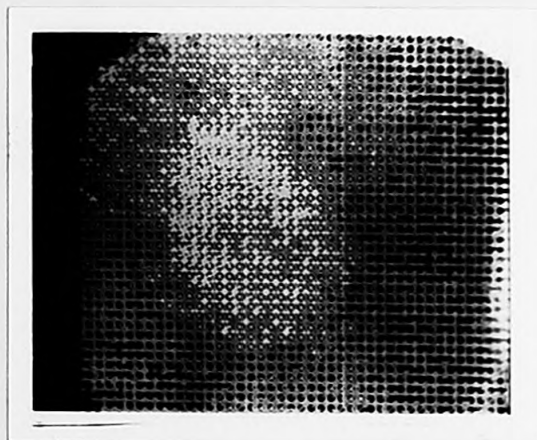
The three heart images shown in Figure 9.1 represent the Anterior, Middle, and Lateral views of the heart. They were obtained at Guy's and transferred in the Department's PDP-11 computer system, following the same procedure as in the cone experiment.



Anterior



Middle



Lateral

Figure 9.1
Healthy heart images.

9.2 IMAGE HANDLING

Some useful information regarding processing requirements can be obtained from a close visual examination of the three heart images of Figure 9.1. This will determine the sequence in which operations must be performed in the image handling procedure. Obviously, due to differences between the heart and cone images in clarity, orientation etc., the path to be followed in this case will be different from that followed for the cone images, i.e. Image Location, Filtering, Image Correlation, Boundary Detection.

It is first noted that the heart images are highly blurred and contain a considerable amount of background radiation which in some parts of the image attains intensity values similar to those of the heart image. For safety reasons, the location of the heart image and its extraction from the overall image matrix will be attempted after the images have been filtered so as to provide better definition of the boundaries of the heart.

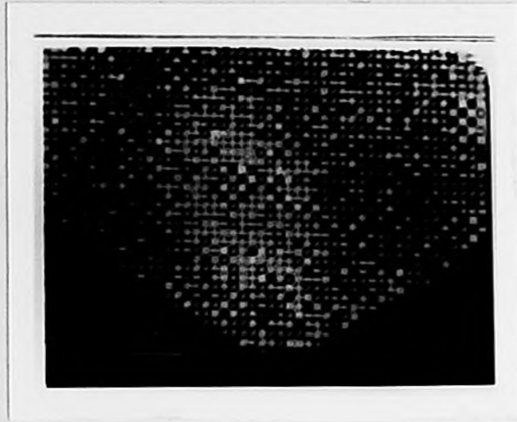
Next, it can be easily observed that the orientation of the heart image within each image matrix is different. This necessitates the development of an algorithm, which in addition to detecting the heart's boundaries will correlate these images best.

The image handling process prior to reconstruction will thus follow the steps: Filtering, Image Location and Extraction, Boundary Detection, Image Correlation.

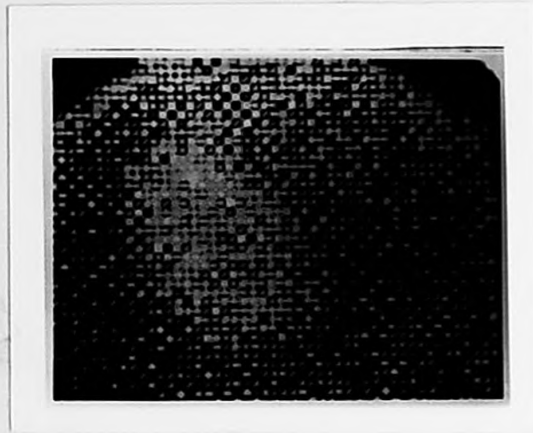
9.2.1 Filtering

The restoration of the heart images of Figure 9.1, which were registered with the Anger camera recording during the whole heart cycle, is a more difficult task due to their highly distorted nature. A careful examination of a heart image would easily reveal a sharp variation in its intensity as we move across the image. This observation is good enough to suggest that the restoration algorithm, which so drastically improved the clarity of the gated heart images, would be unsuccessful in restoring the heart images of Figure 9.1, because the SNR is low (see paragraph 6.1.2). This is demonstrated in the images of Figure 9.2, which result from the application of the Inverse Filtering algorithm, 64X64 version, on the images of Figure 9.1. Similar results were obtained, for low SNR, by Andrews and Hunt [12].

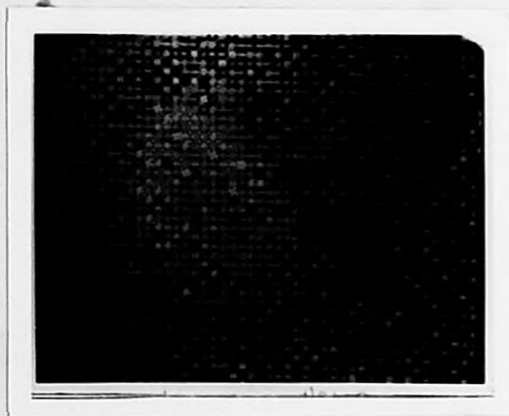
The low SNR in the images of Figure 9.1 is the result of the complex movement of the heart during a heart cycle -rotation and transition- interlinked with the Poisson noise contribution. This can be demonstrated by comparing the filtered version of the



Anterior



Middle



Lateral

Figure 9.2
Inverse Filtering working on healthy heart images.

motion free heart image of Figure 6.3 with the artifacts of Figure 9.2. Obviously, the latter cannot be used for further processing or reconstruction.

The reader is reminded that, in searching for an answer to the above obstacle, the objective is to make maximum usage of the image processing algorithms developed for the cone experiment. Seeking alternative methods of image restoration would prove inefficient and time consuming. The problem was solved by, first employing a two-dimensional smoothing filter to remove a considerable amount of noise from the images, and then, using the Inverse Filtering algorithm to restore the resulting images.

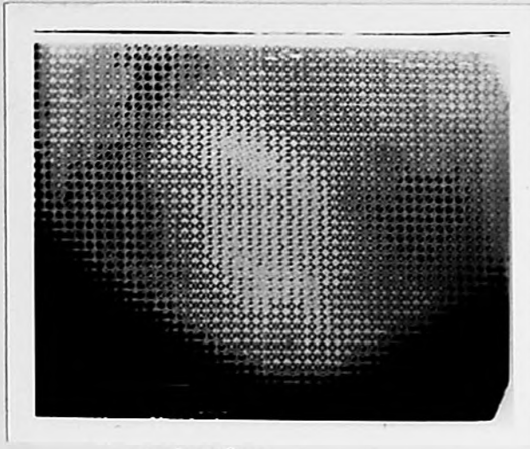
The smoothing filter ensured an improvement in the signal to noise ratio and revealed images 'whose intensity varied slowly across the image'. In other words, this pre-filtering algorithm transformed the images of Figure 9.1 into images suitable for the Inverse Filtering algorithm.

The smoothing algorithm operated first on the rows of the image matrix and then on the columns of the resulting matrix. For each row or column vector of the image matrix, each element, except for the first and the last, was replaced with an average value, obtained by adding a set of consecutive elements (the first element being the current element) and dividing the sum by the number of the elements of the set. The number of elements that each set should contain could be changed interactively: the

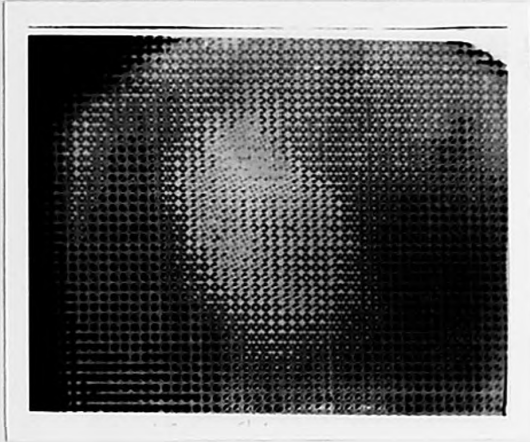
larger the number of elements in a 'smoothing' set the more severe the smoothing of the images. In this way the number of elements per 'smoothing' set, which would produce an 'optimum' smoothing in the images, was found- 3 elements per set- subject to the ability of the author to recognise the 'optimum'. The resulting images had to be smooth enough to guarantee small variations in image intensity, but clear enough -since smoothing causes blurring- to ensure well contrasted images from the inverse filtering algorithm.

Figure 9.3 shows the heart images after smoothing, Figure 9.4 shows the same images after inverse filtering, and Figure 9.5 demonstrates the inverse-filtered version of the Anterior view, which was previously smoothed using 5 elements per set.

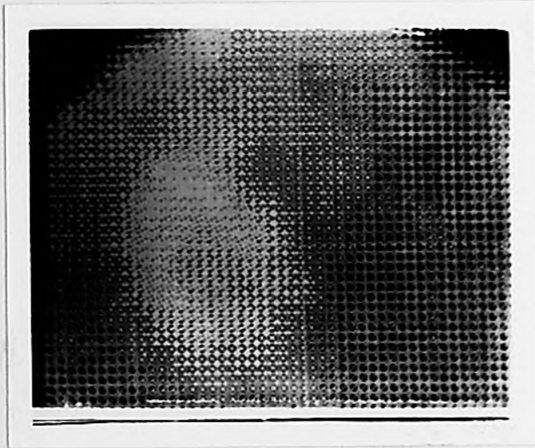
Several conclusions can be drawn from these results. In comparing Figure 9.1 with Figure 9.4 it is observed that the smooth-inverse filtering combination has worked satisfactorily, producing images with good contrast, low SNR, and with locally smooth variation of intensity. Most of the background radiation has been removed, the orientation of the heart within the image matrix is more evident, and the boundaries of each image are now easy to track. This ensures first, that the location of the heart image within the overall image is evident and its subsequent extraction appears possible, and second, that a boundary detection technique can now be developed and successfully implemented. In comparing Figure 9.4(a) with Figure



Anterior

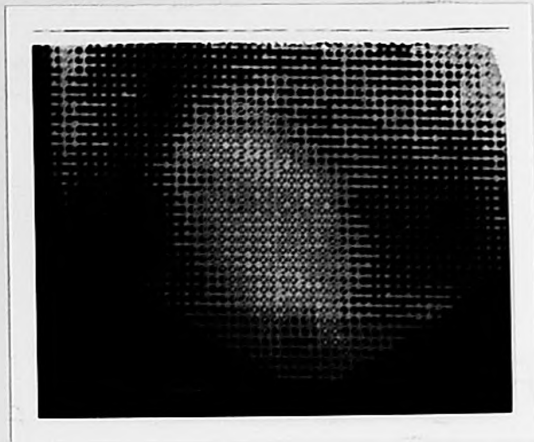


Middle



Lateral

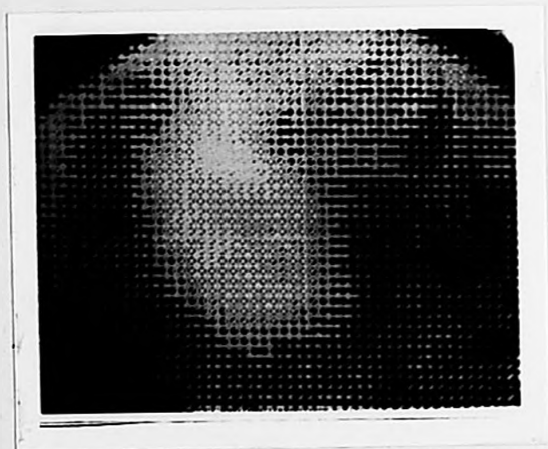
Figure 9.3
Smoothed healthy-heart images, with 3-point smoothing.



Anterior



Middle



Lateral

Figure 9.4

'Smooth-Inverse' filtered healthy heart images.

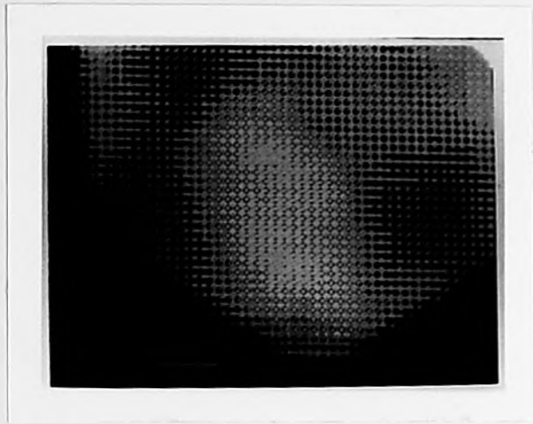


Figure 9.5

**Anterior view of heart 'Smooth-Inverse' filtered
with 5-point smoothing.**

9.5, it is concluded that most of these qualities can be lost if higher order smoothing is used. Evidently, image 9.5 is blurred and its exact boundaries are difficult to follow. Additionally, background radiation still resides on the image. Finally, the smooth-inverse filtering combination was easily implemented in the original filtering algorithm, with no additional storage requirements and with short extra time consumption. It satisfied the limitations and constraints of this research and made efficient use, without alterations, of the existing restoration algorithm. The images of Figure 9.4 can now constitute a starting point for our first attempt to reconstruct the human heart beat.

9.2.2 Heart Motion

Heart images are degraded by an additional point spread function due to the continuous movement of the heart. The result is image blurring in all areas of the image, which could cause the loss of important detail (e.g. small lesions) in the images and consequently degrade the effectiveness of the reconstruction algorithm.

Deconvolving the images for the motion point spread function is not an easy task, since it is difficult to express mathematically the complex periodic movement of the heart.

Several attempts have been made by different workers to overcome this problem. An impressive result is demonstrated in the work of R.C.Mead [32], where the frequency spectrum of the motion point spread function is synthesised using the interactive facility of the computer and the frequency spectrum of a known phantom. Unfortunately, Meade's results cannot be implemented in this work, because they require the operator's intervention in the design of a different motion-PSF for each view, which will violate the time and storage constraints.

The most popular method is the use of an electrocardiographic signal to drive the gamma camera so that photons are registered only during a certain period of the cardiac cycle and thus produce static images [33]. Again, this method is undesirable, because it lengthens considerably the time needed for a complete study of the heart. However, an important remark is made in that paper. An ordinary heart image appears smaller than the end-diastolic and larger than the end-systolic gated images and for an ordinary heart beat at 60 beats per minute, the image corresponds most closely to the end diastolic gated image, because the heart spends about 50% of its cycle in diastole at a motion free state. Therefore, ordinary heart images are influenced, to a certain extent, by the static state

of the cardiac cycle, which implies that the effect of image degradation due to heart movement alone would not hinder the detection of reasonable lesions in the reconstructed images.

It can be concluded that cardiac motion has a mildly degrading effect on the images and this should not discourage the use of these images in the reconstruction algorithms.

9.2.3 Boundary Detection

In developing a boundary tracing routine the target will be to design an efficient algorithm, which will satisfy the time and storage constraints and will produce reliable boundaries. For this, a priori information concerning the shape of the heart image, its orientation within the image matrix, and a degree of mild similarity amongst the projection images, will be taken into account. Naturally, the use of much a priori information limits the generality of such a boundary detecting technique to heart images alone.

Close observation of the filtered heart images of Figure 9.4 has led the author to the realization that a parabola would fit best the boundaries of the heart images. Multiple experimentation on the images has verified the parabolic behaviour of the heart boundaries. It has also revealed that the

Chapter 9

same parabola would fit, to the best visual approximation, all three images. The boundary similarity can be also verified by the reader when he considers the images of Figure 9.6(c), where the same parabola has been superimposed on the images of Figure 9.4. It is also observed, that images differ in orientation within the image matrix. In this way the heart is modelled as a three-dimensional, thick walled, hollow paraboloid, whose cross section is circular.

The parabola was shaped according to the equation:

$$y=A.x^2 \qquad 9.1$$

where constant A could be changed interactively to accomodate changes in the shape of the parabola. The axis of symmetry of the parabola was to fall on the axis of symmetry of the heart image, thus provision was made to change its orientation interactively. The third parameter, interactively modifyable, was the location of the apex of the heart.

Next, suitable data had to be collected from within each section of the heart images, which were bounded by the parabola, to constitute the projected images, in the three different directions, of consecutive slices through the heart muscle. This was achieved by drawing lines at right angles to the axis of each parabola, which were separated by a pixel-sized length along the parabola's axis as shown in Figure 9.6(a), and segmenting each line section bounded by the curve, each segment having the size of a pixel (15 units on the TK-screen). Each selected point on

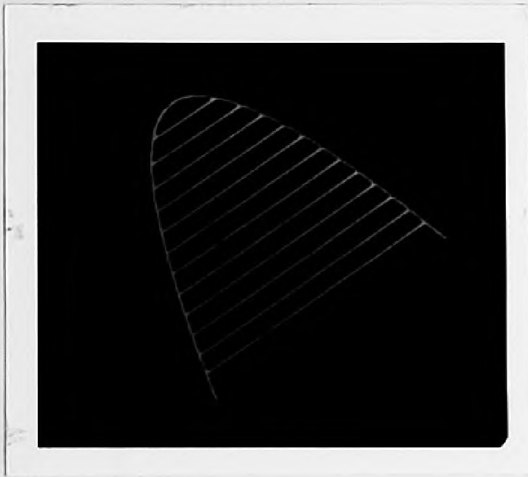


Figure 9.6(a)
Parabola as used for Boundary Detection algorithm.

the line section does not necessarily fall on a matrix grid point. It was thus necessary to interpolate each point's intensity from the intensities of the nearest four grid points in an inverse proportional manner to its distances from these grid points. Figure 9.6(b) shows how an off-grid point P was constituted from its nearest four grid points according to the equation:

$$R=R_1(1-d_3)+R_2(1-d_4) \quad 9.2$$

where,

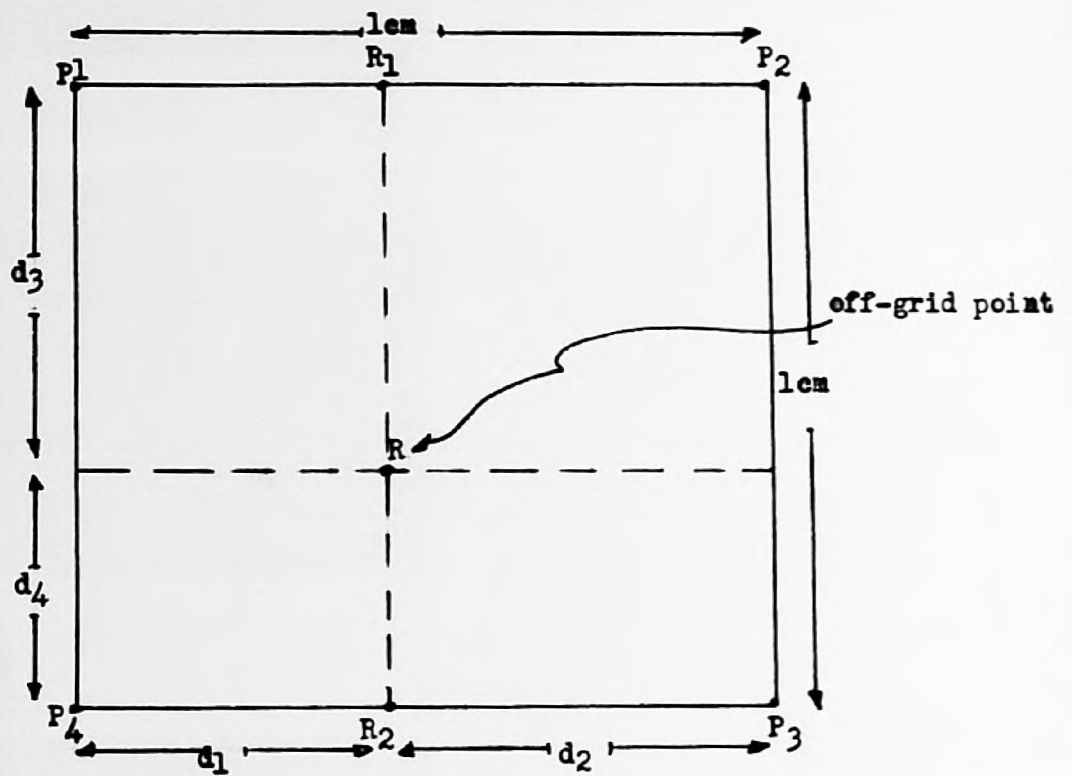
$$R_1=P_1(1-d_1)+P_2(1-d_2)$$

$$R_2=P_4(1-d_1)+P_3(1-d_2)$$

and $d_1+d_2=d_3+d_4=1$

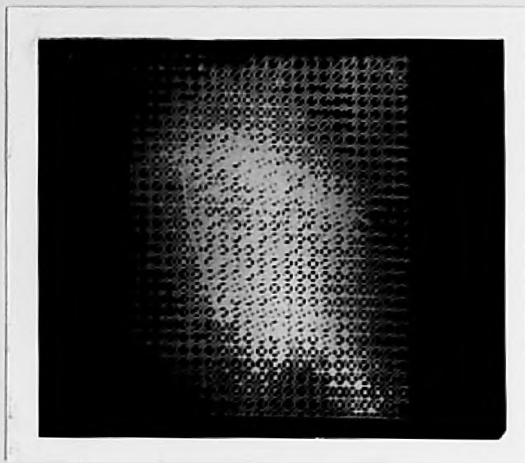
where, P_1, P_2, P_3, P_4 are the intensities of the nearest grid points, d_1, d_2, d_3, d_4 are the distances as indicated in Figure 9.6(b), and R is the intensity of the off-grid point. It is easily verified that if the off-grid point falls on a grid point, e.g. P_1 , then $R=P_1$ and $d_1=d_3=0, d_2=d_4=1$.

The similarity of the parabolas renders the problem of image correlation an easy task, ofcourse subject to the operator's ability to determine with accuracy the apex and orientation of the heart image. From each image, data vectors of corresponding slice-images are collected and stored together, ready for insertion into the reconstruction algorithm. An important asset of this technique is that for each slice there are three corresponding vectors with the same number of data. Thus the cumbersome calculations, involved in the cone's case in

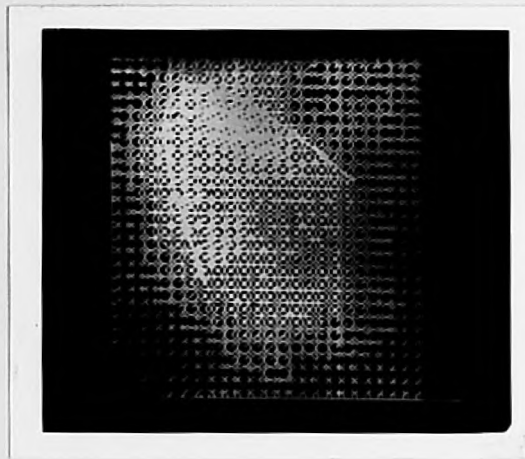


$$R = R_1(1-d_3) + R_2(1-d_4)$$

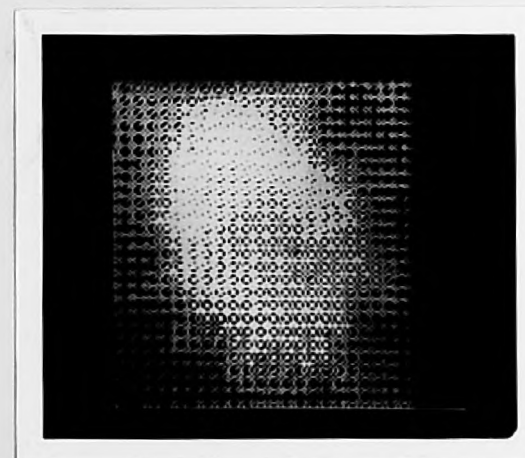
Figure 9.6(b)
Calculation of the intensity of an off-grid point.



Anterior



Middle



Lateral

Figure 9.6 (c).

Parabola superimposed on healthy-heart images.

Chapter 9

equalising the number of data per selected vector, is avoided with considerable economy in computer time.

Concluding, an efficient method of boundary detection has been developed, which with minimum operator's intervention can overcome successfully the seemingly difficult problem of boundary detection in gamma images. It is fast, requires low storage, and is simple in its structure and implementation with impressive results.

Overall, the boundary detection algorithm performs the following steps:

1. Reads image from store and plots it on the TK-screen.
2. Requests coordinates of heart's apex point, angle of heart's axis orientation, and parameter A of parabola.
3. Draws parabola over the heart images on TK-screen.
4. Segments the parabola, drawing line sections perpendicular to the axis of symmetry as shown in Figure 9.6(a).
5. For each line section calculates new off-grid points and stores them in a vector array.
6. Repeats steps 1 to 6 until all images have been accounted for.
7. Correlates vectors, stacks them together, and stores them in a floppy disc.

Chapter 9

Figure 9.6(d) shows a flowchart of the boundary detection routine.

9.2.4 Modifications in the Reconstruction Algorithms

The reconstruction of the left ventricle of the human heart from three of its projected gamma images implied certain modifications in the reconstruction algorithms.

Modelling the heart as a three-dimensional, thick walled, hollow paraboloid, whose dimensions could be altered between different studies due to changes in the actual dimensions of the heart, necessitated the development of a different approach for the calculation of the dimensions of the heart model (e.g. radius of each slice), which would accommodate automatically to these changes. Therefore, unlike the case of the cone experiment, the dimensions of the parabolic model of the heart will be subject to modification, at this part of the report, according to the result of the boundary detection algorithm. The outer diameter of each slice was calculated from the length of the corresponding line-section bounded by the parabola, see Figure 9.6(a), with a suitable transformation in length units, from TK-screen units to centimetres, and ensuring wall thickness of 1cm for each slice. This transformation revealed realistic dimensions for the heart model similar to those of a typical left

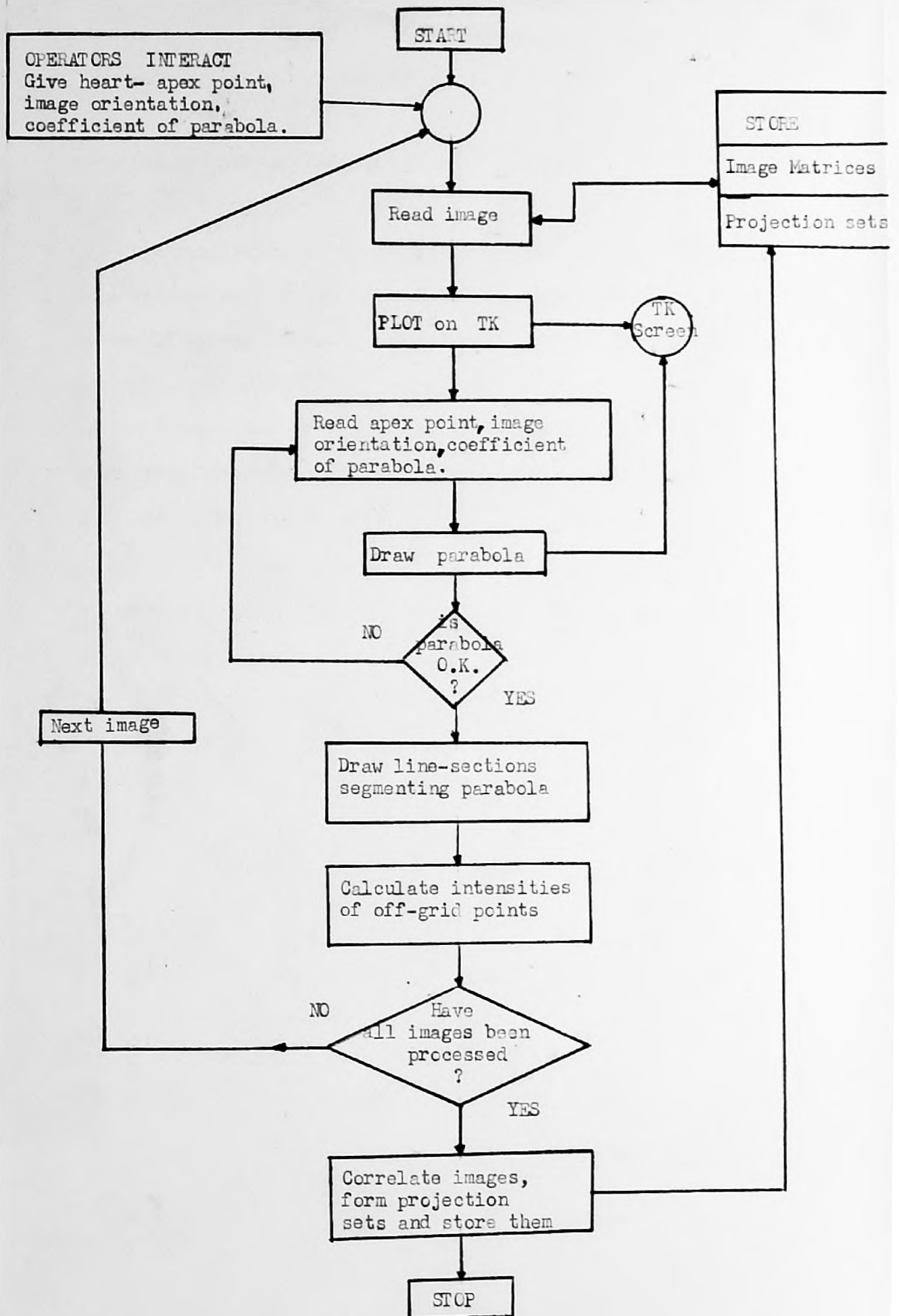


FIGURE 9.6(d)
FLOWCHART OF THE BOUNDARY DETECTION ALGORITHM

Chapter 9

ventricular phantom provided by Guy's Hospital.

The dimensions of the arrays of the reconstruction algorithm were reduced suitably to accommodate for the reduction in the number of gamma images, from four to three. This reduced the storage requirements of the reconstruction algorithm and speeded up the reconstruction procedure considerably, thus bringing the algorithms operating point well inside the space defined by the time and storage constraints.

9.3 RECONSTRUCTION OF A HEALTHY HEART

The manipulation of the original heart images of Figure 9.1 through the filtering, boundary detection, and data arrangement in projection sets, procedures enables their direct insertion into the reconstruction algorithms.

In this section most of our attention will be concentrated on the elaboration of the resulting images rather than on the effects of the sources of image degradation on the reconstructed images. Filtering was shown to be a decisive factor for the further processing of the heart images, thus the reconstruction algorithms will operate on the filtered images. However, mention will be made on the effect of the photon attenuation on the resulting images, to test the correctness of the alterations made in the attenuation routine.

The reconstructed images will represent, as in the cone experiment, the deployment onto a flat surface of the Thallium density distribution in the muscle tissue of the heart's left ventricle (LV). The thickness of the muscle tissue around the walls of the LV is variable, while its mathematical model was considered constant at 1cm. This, however, will not constitute a discrepancy, since we are reconstructing radioisotope density distribution, and any differences in wall thickness between the LV and the model will appear as regions of lower or higher activity, which in turn will

Chapter 9

indicate the variations in thickness of the muscle tissue around the walls of the LV, confirming that the mapping of the left ventricular muscle tissue has been realistic.

The experimental procedure to be followed in this section will consist of, first employing the SP-algorithm to reconstruct the Thallium distribution in the walls of the LV, and second repeating the same three-dimension reconstructional experiments using the MLSE-algorithm. This series of experiments will assist us in judging the truthfulness of the reconstructions, as a first indicator in our attempt to estimate the quality of the results, since similarity amongst corresponding reconstructions from two different algorithms guarantees realistic results.

It is necessary to point out here, that when the heart images of Figure 9.1 were recorded it was not known whether lesions were present to be detected, but it was agreed to compare the results of our reconstruction algorithms with the findings of the investigation at Guy's Hospital and thus draw the necessary conclusions on the effectiveness of our method.

9.3.1 SP-Algorithm

Two reconstructions were produced using the SP-algorithm. Again, -ATT and +ATT, will denote the non-elimination and the elimination of the attenuation phenomena respectively. Figure 9.7 provides the reconstruction of the Thallium density distribution under -ATT and Figure 9.8 under +ATT. In comparing Figure 9.7 and 9.8 it can be concluded that, while the effect of the photon-attenuation elimination may not be as evident as in the cone's case, where visual comparison was greatly assisted by the existence of the rubber wedge, a careful examination reveals that areas of higher or lower activity are contrasted best in Figure 9.8 (+ATT). This observation coincides well with reality, since, as mentioned before, the thickness of muscle tissue around the LV walls is variable, and this is highlighted best in Figure 9.8, where the sectional areas of higher and lower activity find a better definition (see Figure 9.18 for LV-wall thickness variation).

Clearly, lesions or damaged muscle tissues are absent. The confidence of this diagnosis emanates from the fact that successful filtering of the original images and contrast enhancement of the reconstructed images by attenuation elimination, procedures which have been proved effective in locating with accuracy the areas of inactivity in the cone, have not revealed similar discontinuities in the reconstructed heart images. This will also be verified when the MLSE-algorithm attempts the reconstruction.

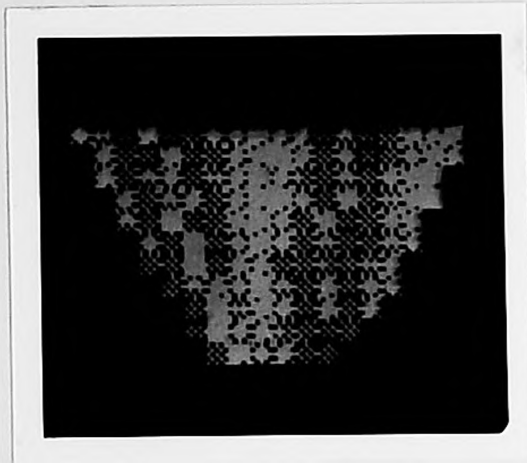


Figure 9.7
SP-reconstruction,
no attenuation correction.

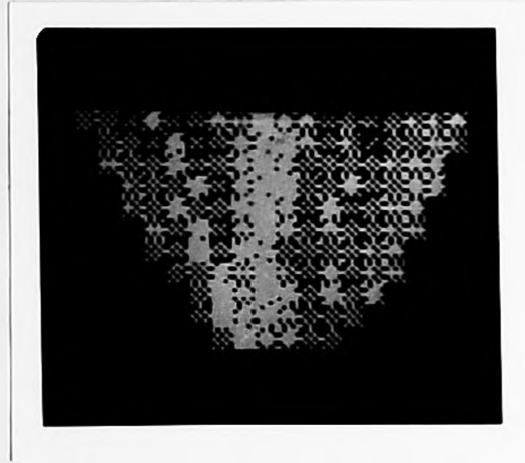


Figure 9.8
SP-reconstruction,
attenuation eliminated.

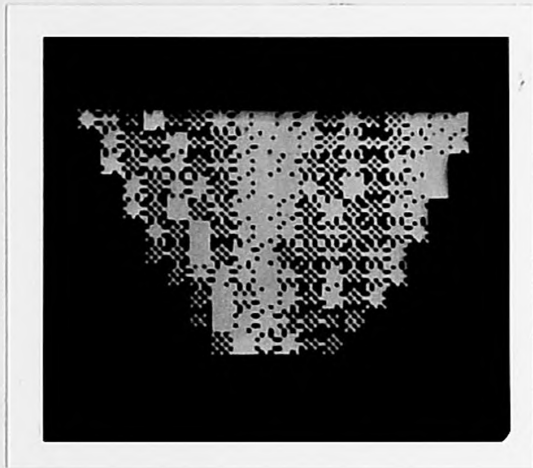


Figure 9.9
MLSE-reconstruction,
no attenuation correction.

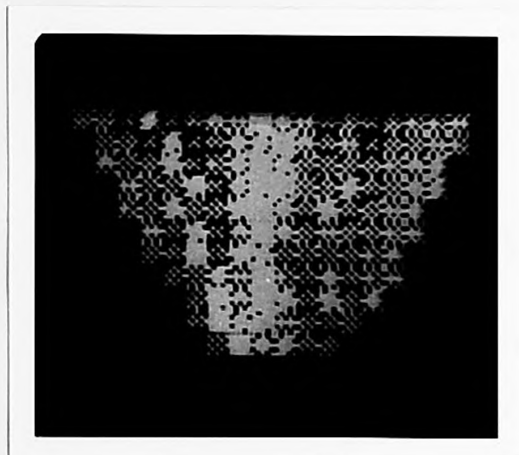


Figure 9.10
MLSE-reconstruction,
attenuation eliminated.

Figures 9.7-9.10
Healthy heart reconstructions.

Chapter 9

An additional indication of the correctness of the reconstructions is the fact that, although each slice has been reconstructed separately, there is however an apparent consistency in the position of higher and lower activity in each slice's reconstructed image, which is indicated best when all slices are stacked together to reveal continuous regions of higher or lower activity. Such description fits closely to the variation of muscle tissue thickness around the walls of the LV (see section 9.4.4.)

9.3.2 MLSE-Algorithm

Similar reconstructions were performed using the MLSE-algorithm. Figure 9.9 shows the reconstruction under -ATT conditions and Figure 9.10 under +ATT conditions.

In comparing Figure 9.9 with Figure 9.10 similar conclusions can be derived. Again, attenuation-elimination improves contrast and definition in the variation of activity across the resulting image, lesions are absent, and the variation of intensity across the image fits closely to the anatomical description of the LV wall.

9.3.3 Comparison-Conclusions

This section describes a first attempt to reconstruct the Thallium density distribution in the left ventricular wall of the living human heart from three of its projected gamma images. Both algorithms, The SP and the MLSE, were employed to perform the reconstructions on the filtered versions of the gamma images, revealing satisfactory results, which would approximate closely to the anatomical structure of the left ventricle. The effect of photon attenuation was examined by contrasting the images produced under -ATT and +ATT conditions by both algorithms, and it was shown that its elimination improved the quality of the reconstructions, which in turn verified the correctness of the modifications made in the attenuation correcting routine. Additionally, the comparison of the reconstructions by both algorithms under similar attenuating conditions (i.e. -ATT or +ATT) revealed reasonable similarity, which is indicative of the faultless of the results.

Of the two techniques, the MLSE-algorithm provided fractionally better images, which verifies, once again, the fact that the Poisson noise contribution is small in magnitude but not negligible. But to compare the performance of each algorithm, the algorithm's efficiency has to be examined in accordance with the overall objective, that is the best balance between the satisfaction of the time and storage constraints and the quality

of the reconstructed images. If it is assumed, at least for this part of the report, that the shape of the parabola in the boundary detection routine changes between different heart studies, then the parameters of the mathematical model of the heart will change, and the MLSE-algorithm will provide the best solution. However, it is noted that the overall process of filtering, boundary detection, and reconstruction for the heart is faster and less core demanding than for the cone (smaller image-matrices, fewer views). This renders the reconstruction problem plausible, since it takes about 20mins for the MLSE-algorithm to reconstruct 11 slices of the heart, after filtering.

Finally, one question, which still remains unanswered, is whether the effect of heart motion hides important information, which prevents the appearance of probable lesions in the reconstructed images. This question was partly answered when our results and those from Guy's confirmed the non-existence of lesions in the particular study. Further clarification to the above question will be derived in the next section, where the reconstruction of a defective heart will be attempted.

9.4 RECONSTRUCTION OF A DEFECTIVE HEART

The next target of the research is the reconstruction of a defective heart from three gamma images. This attempt constitutes the crucial step in our work, for the ability of the reconstruction algorithms in providing the existence of lesions with accuracy and clarity is to be tested. Additionally, this attempt will assist towards obtaining a better estimation of the effects of the Poisson noise and photon attenuation on the images and will help to evaluate the ability of the algorithms in removing those sources of degradation and in providing good reconstructions, since judgement will be now based on two criteria, first clarity and accuracy of lesion definition and second realistic recovery of Thallium density distribution. Further, a good reconstruction with accurate location of lesions when combined with the successful reconstruction of the normal heart and then contrasted against the exact reconstruction of the cone, is a good enough proof of the validity of our methods, the correctness of the algorithms, the truthfulness of the results, and the success of our task.

The set of three 'defective heart' gamma images, for the second attempt to reconstruct the heart, was chosen to be different from the first set in the angle interval between the different views, after consultations with Guy's. The objective was to 'push' the imaging demands of our method close to the heart-imaging procedures used for routine patient examination at Guy's and other hospitals.

Chapter 9

Detailed examination of heart models and considerations in the probable orientation of the heart in the human body revealed that, first two common views of the heart, the Anterior (ANT) and the Left Lateral (LL), satisfied to a good approximation the image recording conditions of our algorithm, which requires the axis of symmetry of the heart to be at right angles to the direction of image recording, and second the uncertainty, which prevailed in the orientation of the heart axis in the human body during the recording of the 'healthy-heart' images (Figure 9.1), matches the uncertainty prevailing during the recording of the ANT and LL images.

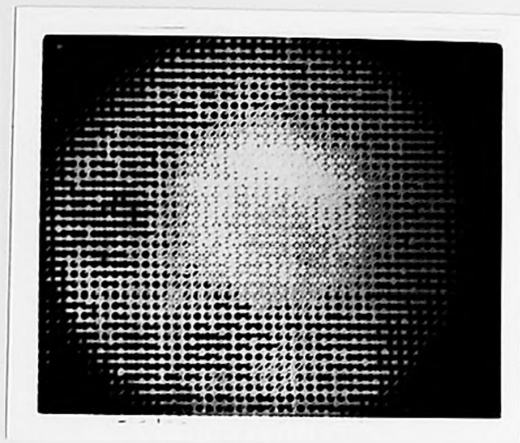
The latter images correspond to a 90 degrees camera rotation, allowing for a third view to be easily recorded at the intermediate 45 degrees position, which we shall name Middle view (MID). These images have several advantages over the 'healthy-heart' images. First, they span a larger arc of 90 degrees compared to 40 degrees used previously, thus improving the reconstructional accuracy of the algorithms, second, they are easy to obtain, since cumbersome adjustment of the head of the Anger camera and movement of the patient's bed to achieve the required image recording direction is avoided, and third, their recording does not upset the image recording procedure at Guy's, thus rendering the parallel patient examination by our method and that at Guy's possible. Finally, the reconstruction of the heart from a new set of different heart views is an advantage, since a correct reconstruction will prove that our methods and algorithms are flexible enough to accommodate changes in the heart imaging procedure.

Chapter 9

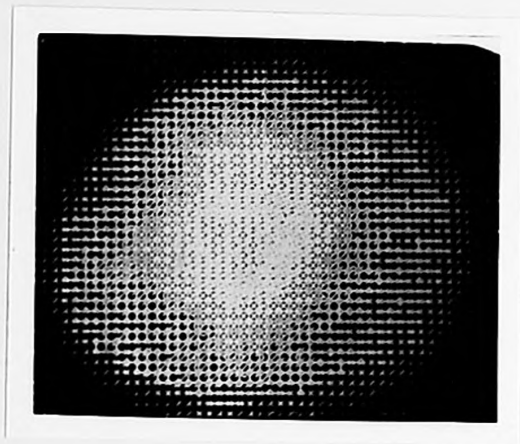
Figure 9.11 shows the three images of the defective heart. Image handling and three-dimension reconstructional procedures will be exactly the same as in the 'healthy-heart' reconstruction. In this case it is known that there are lesions, which can be observed by a careful examination of the images of Figure 9.11, but this will not alter the methods or procedures used for the reconstruction.

9.4.1 Image Handling and Boundary Detection

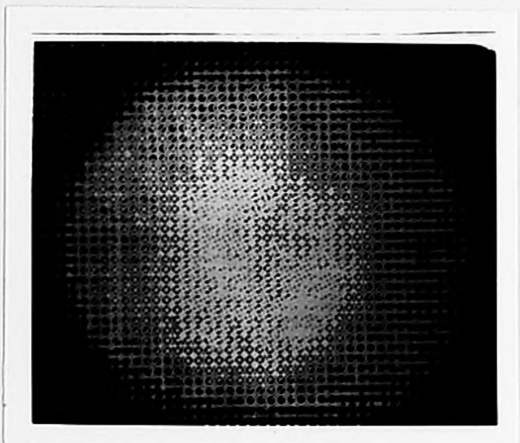
The images of Figure 9.11 were first filtered, using the dual filtering procedure of smooth-inverse filtering, and next extracted from the 64X64 image matrices to form the images of Figure 9.12. Smoothing and inverse filtering coefficients, vital factors in determining the extent of image filtering, were kept similar to those used for the 'healthy-heart' study. Finally, the boundary detection routine operated on the filtered images, with the same parabola providing a satisfactory fit to the boundaries of all three views as shown in Figure 9.13 and stacking together correlated vector data selected from each image to form the projection sets, corresponding to the slices through the left ventricle of the heart. This parabola differs from that of the healthy heart study (compare Figures 9.13 and 9.7)



Anterior

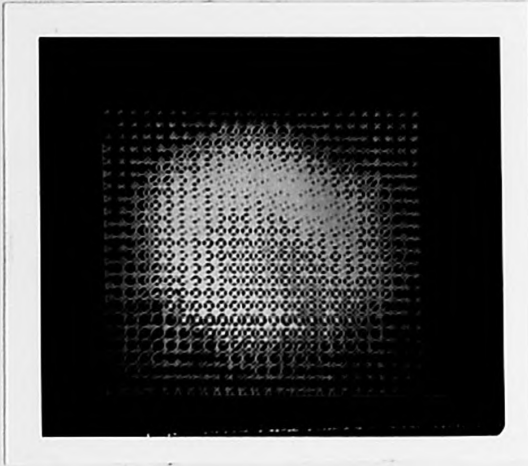


Middle

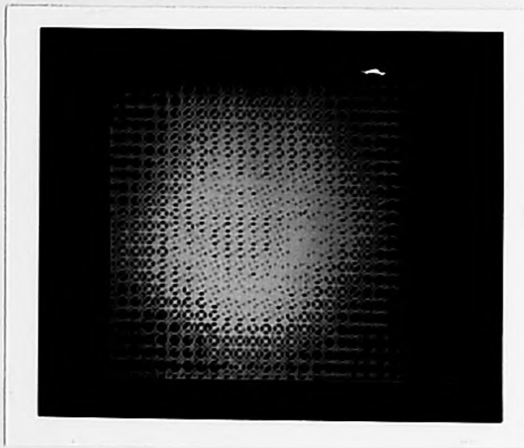


Lateral

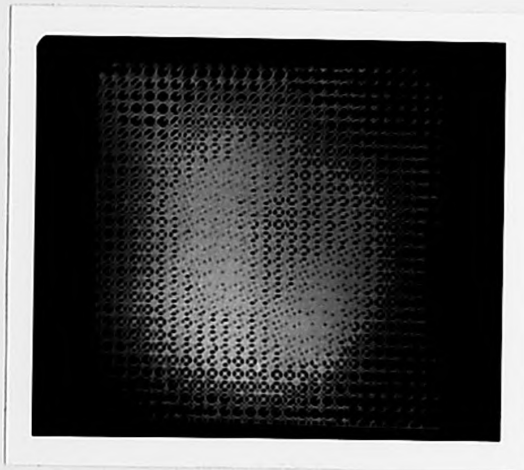
Figure 9.11
Original defective heart images.



Anterior

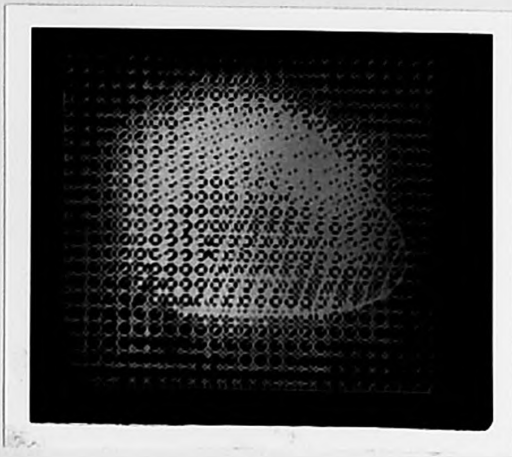


Middle

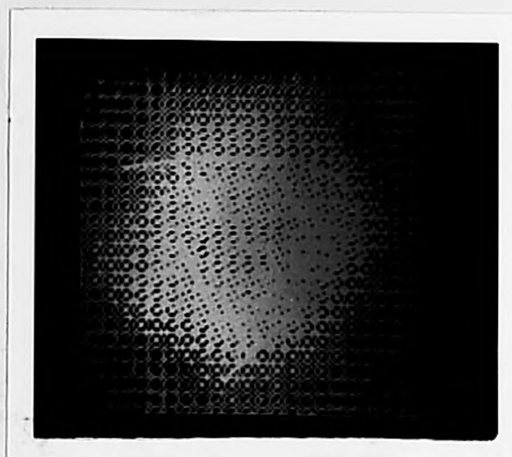


Lateral

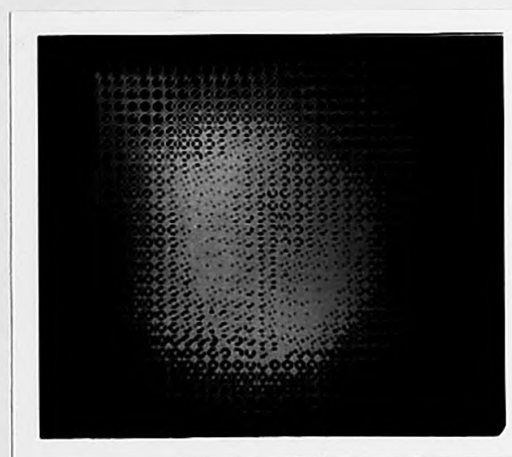
Figure 9.12
Heart images contained in 32x32 frame matrices.



Anterior



Middle



Lateral

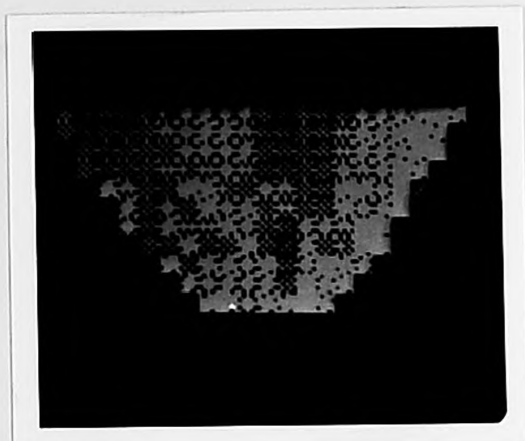
Figure 9.13
Parabola tracing edges of defective heart images.

9.4.2 SP-algorithm

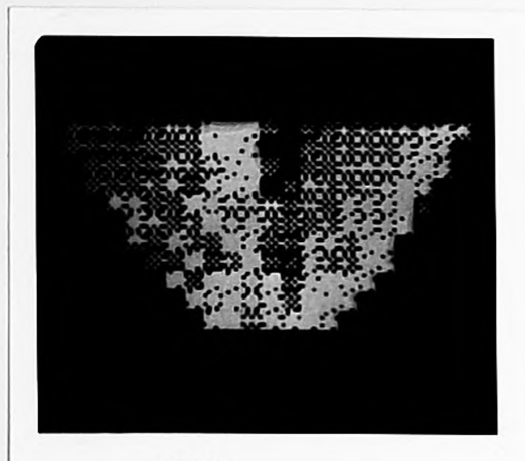
Two reconstructions were performed employing the SP-algorithm. Firstly, the Thallium density distribution in the LV was recovered without compensation for the attenuation phenomena, i.e. under -ATT conditions, as shown in Figure 9.14. Then the SP-algorithm compensated for photon attenuation (+ATT) revealing the reconstructed image shown in Figure 9.15.

Examining Figure 9.14 it is noted that the image consists of regions of higher and lower intensity corresponding to the variation in thickness of muscle tissue around the walls of the LV. This can be verified when the image is compared with that of Figure 9.7, which shows the SP-reconstruction under similar conditions (-ATT) for the healthy heart, their similarity in the layout of higher and lower intensity is apparent. At most this observation can constitute a promising indication for the correctness of the reconstruction of Figure 9.14.

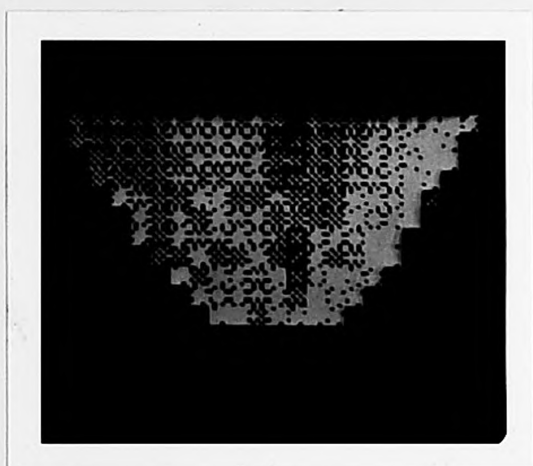
The existence of lesions is a bit problematic, since although their evidence is not apparent in Figure 9.14, there is however a faint suspicion of their location in the middle region of the image. This suspicion is proved beyond doubt true in the image of Figure 9.15 (+ATT), where the elimination of the photon attenuation effect has revealed with clarity the position of the defective muscle tissue.



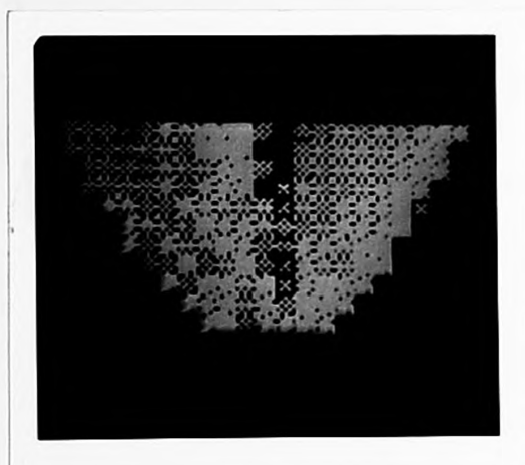
9.14
SP-reconstruction,
no attenuation correction.



9.15
SP-reconstruction,
attenuation eliminated.



9.16
MLSE-reconstruction,
no attenuation correction.



9.17
MLSE-reconstruction,
attenuation eliminated.

Figures 9.14-9.17

Reconstruction of a defective heart

It can now be claimed with confidence that the removal of photon attenuation has been accomplished successfully and that its elimination is as important as our certainty in determining the location and extent of dead muscle tissue in the reconstructed images.

In comparing Figures 9.14 and 9.15 it is again observed that the distribution of regions of higher or lower intensities is similar in both images, with Figure 9.15 providing a better and sharper region definition. This eliminates any doubts of a possible artifact-reconstruction in Figure 9.15, since the area of non-activity (lesions) is clearly evident and the remaining area in the image bears a close similarity to the corresponding regions in Figure 9.14 (-ATT) or Figure 9.7 (-ATT, healthy heart).

9.4.3 MLSE-algorithm

Two similar reconstructions were produced using the MLSE-algorithm. Figure 9.16 presents the MLSE-reconstruction under -ATT conditions and Figure 9.17 gives the MLSE-reconstruction after the removal of the attenuation effect (+ATT).

Chapter 9

Conclusions similar to those derived in the previous paragraph (9.4.2) can easily be derived too, signifying the improvement in lesion definition and clarity after the elimination of the attenuation phenomena, and stressing the truthfulness of the reconstructed regions of intensity after contrasting these two images.

9.4.4 Comparison-Conclusions

In this section the reconstruction of a defective heart was attempted from a set of three images recorded at 45 degrees intervals. The heart images used were the two standard views, the Anterior and the Left Lateral, which are widely used in Nuclear Medicine for routine patient examination and a third non-standard view at the 45 degrees intermediate interval. Both algorithms, the SP and the MLSE, worked satisfactorily well, recovering the Thallium density distribution in the walls of the left ventricle successfully enough to reveal the location of the lesions with accuracy and clarity. Lesions became evident when the photon attenuation effect was removed, proving once again the importance of such a measure.

Chapter 9

Similarity in the reconstructed images, both in the position and extent of the region of inactivity (lesions) as well as in the rest of the image, verified the truthfulness of the reconstructions. The latter is particularly highlighted when the 'defective-heart' reconstructions are contrasted to the 'healthy-heart' reconstructions. Overall, the heart reconstructions correspond with reasonable accuracy to the anatomical model of the left ventricle. This can be proved by considering the real slice through the LV and examining the correspondence between the variation in thickness of the LV wall and the variation in intensity of the reconstructed image. Figure 9.18 shows a typical slice through the left ventricle where H and L signify the thick and thin regions of muscle tissue respectively. Below is the image resulting after several slices have been reconstructed. Image deployment onto a flat surface starts from pixel 1 and follows an anti-clockwise direction. Thus, regions of high and low intensity are mapped on the reconstructed image, resulting in a L-H-L-H sequence. Similar regional sequence is observed in the reconstructions for both the healthy and defective hearts. The correctness of the reconstructions is therefore proved beyond doubt.

The Poisson noise effect can be assessed in comparing images 9.15 (SP-reconstruction) and 9.17 (MLSE-reconstruction). The latter gives a better lesion definition, both in clarity and extent, and produces a smoother image signifying the removal of the Poisson noise effect. Overall, the MLSE-algorithm provides

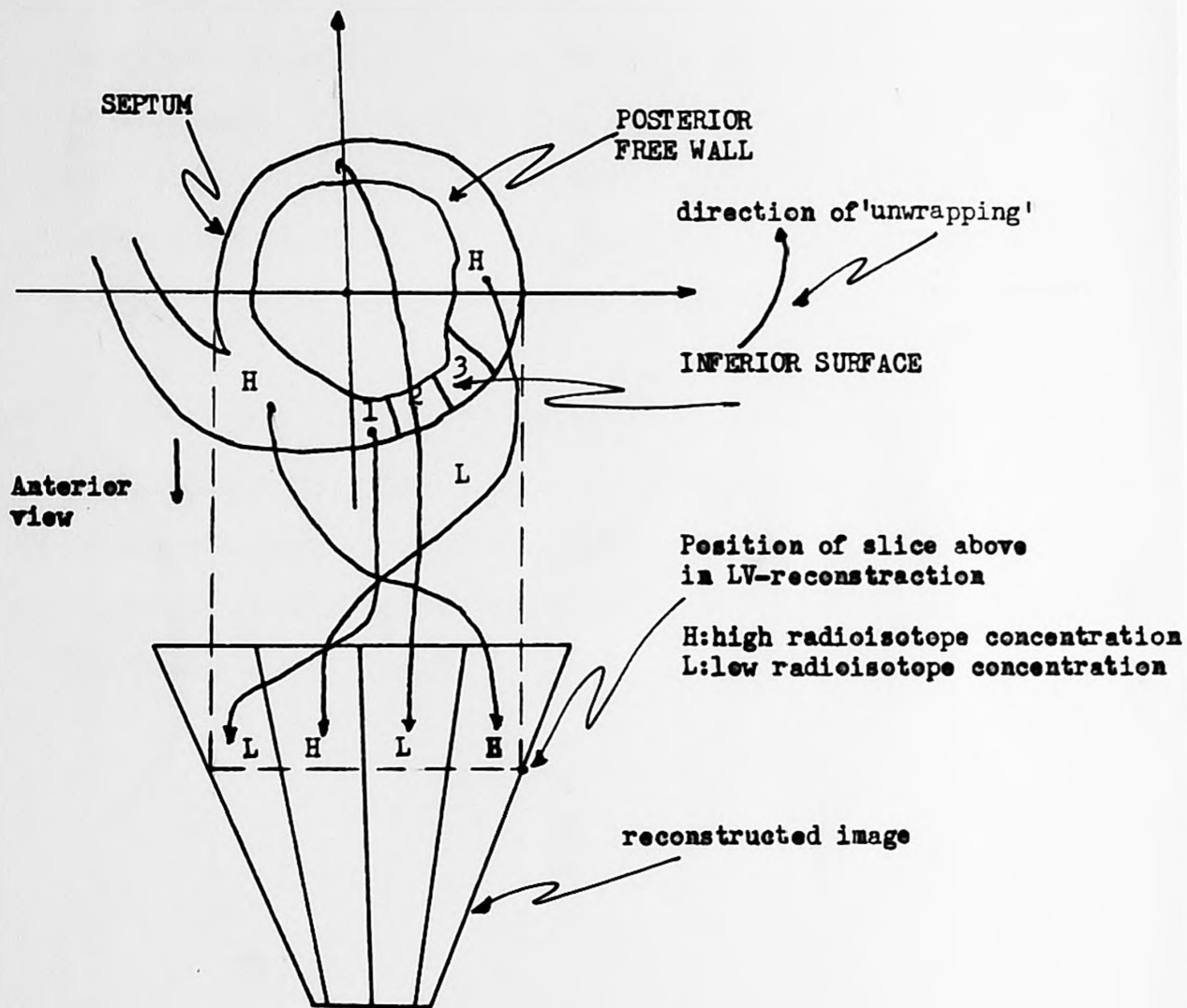


Figure 9.18

Typical slice through Left Ventricle.
Muscle thickness variation as
depicted on the reconstructed
LV-radioisotope concentration.

Chapter 9

the best reconstruction.

Heart motion does not hinder the detection of lesions, but its effect is evident on the reconstructed images producing a certain amount of blurring, which distorts the accurate definition of the lesions. Comparing image 9.17 with image 8.14 (MLSE-reconstruction of the cone) the difference in sharpness and clarity in the regions of inactivity is evident.

Concluding, it can be claimed that the difficult problem of reconstructing the human heart within the given time and storage constraints found a promising solution which enables the determination of the location and extent of infarcts in the left ventricular muscle tissue.

10 DISCUSSION

This final chapter reviews the work that has been accomplished, provides a critical comparison of methods and results, suggests the procedure for the clinical application of this work, and finally proposes future directions for increasing the efficiency and accuracy of the whole tomographic procedure.

10.1 CRITICAL REVIEW-CONCLUSIONS

This research was initiated by the need in Nuclear Medicine to examine the internal organs of the human body atraumatically, exploiting the unique properties of Emission Imagery. The work was directed towards the most vulnerable but most difficult to examine organ of the human body, the heart, and its objective was the determination of the location and extent of damaged myocardium tissue following a heart attack. The problem was complicated because in addition to the problematic nature of gamma-imaging the heart, serious constraints were introduced by the available machinery and clinical requirements.

To overcome the difficulties of Emission Imagery in general and in particular those arising in this application and at the same time safeguard against violations of the constraints, a methodology was developed that eventually led to the satisfaction of all requirements and objectives. Accordingly, a theoretical background was built, which analysed the processes involved in Emission Imagery and assisted in the linear formulation of the image formation process. This expression (equation 5.16) was a function of the radioisotope distribution in the left ventricle, the Poisson noise, the photon scattering, the photon attenuation, and the motion of the heart. Photon attenuation and radioisotope distribution were also functions of the anatomic structure of the left ventricle. The retrieval of the radioisotope distribution required explicit

mathematical expressions for most of the constituents of the image formation formula and a reconstruction method, which simulated in the computer the 'reversal' of the image formation process and thus reconstituted the radioisotope distribution from a small number of gamma images. Three images of the heart at different angles were found sufficient for reasonable reconstructions, but two images were found not to be adequate.

In particular, the methods employed in each step of the overall 'image processing-heart reconstruction' procedure and their corresponding achievements are listed below. Presentation follows the pattern of 'necessity-method-achievement' for each step of the procedure.

1. Elimination of photon scattering

Photon scattering induced the system's point spread function on the images. Its elimination was a necessary measure taken to insure image formation by straight, parallel, non-overlapping rays and allow the practical implementation of slicing the three-dimensional radioisotope distribution into a set of two-dimensional planes. It also increased image contrast, thus assisting in the detection of image boundaries.

Chapter 10

A two dimensional smoothing filter was used first to remove most of the noise residing on the heart images, as a result of the cardiac motion and the statistical uncertainty of the radioisotope decay. Next, the imaging system's PSF was assumed Gaussian and was suitably designed using the interactive facility of the computer. The Inverse Filter was then employed to deconvolve selectively in the frequency domain the PSF from the image.

The design of the system's PSF and of the 'smooth-inverse' filter was achieved by modifying interactively certain parameters and judging subjectively the quality of the resulting images. Multiple experimentation led to the evaluation of optimal values for those parameters, which proved suitable for all gamma images.

The 'smooth-inverse' image restoration algorithm proved an efficient method in improving the quality of the cardiac images and enhancing their contrast. It solved the difficult problem of restoring the highly degraded gamma images of the heart employing simple methods, requiring the least a priori information, demanding relatively small computer core, and consuming only 1 minute of computer time for a complete restoration of a 32X32 image. But its effect was not confined to image enhancement. The filter's contribution to the overall 'image processing-reconstruction' procedure was invaluable, since it facilitated the comfortable tracing of the heart's boundaries and rendered the reconstruction process valid. The latter was particularly demonstrated when filtering was proved to be a decisive factor in locating areas of

inactivity in the reconstructed images.

2. Development of Mathematical Model for the Left Ventricle.

The development of a mathematical model for the LV was a necessary step taken to provide a mathematical expression for the anatomic structure of the LV, which is involved in the formulation of the image formation process.

The choice of the three-dimensional, thick-walled, hollow paraboloid to represent the anatomic structure of the LV, was the result of a careful examination, which took into consideration the LV-structure in different cardiac phantoms, the shape of its boundaries in many filtered gamma images, and the correspondence between geometrical structure and projected image.

The implementation of the mathematical model in the image formation process reduced drastically computer time consumption, since iterative procedures to determine the shape of the radioisotope distribution were avoided, and economised in computer core, since advantage was taken of the structural features (thick-walled, hollow) of the LV. Most important, the mathematical model facilitated the effective elimination of the attenuation phenomena, since distances travelled by gamma photons could be readily calculated. It was thus possible, to overcome the disadvantages of the pseudoinverse reconstruction method (time consuming and core demanding) and make full use of its advantages

(accuracy, small number of images). Finally, it was proved that suitable adoption of a priori information constitutes a powerful tool in overcoming the problematic application of Emission Imagery in medicine.

3. Boundary Detection

The purpose of the boundary detection algorithm was to extract from the gamma images the image of the LV, correlate the extracted images, segment each image into parallel regions corresponding to slices through the LV, select corresponding regions from each image, and store selected regions together, ready for insertion into the reconstruction algorithms.

The multiple tasks of this algorithm could only be achieved, if a priori information, concerning the shape of the projected LV-image and the structure of the left ventricle, was used to establish the parabolic behaviour of the LV-boundaries; experimentation was performed on a satisfactory number of filtered images of the heart. It was found that the same parabola would fit the boundaries of the LV in each of the three projected views of the heart. Differences in the orientation of the LV-images demanded the structure of a grid-rotation routine, which involved interpolatory procedures in reconstituting each 'new-grid' intensity point from four of its nearest 'old-grid' points. Image correlation, segmentation, and appropriate 'slice-region' selection was an easy task, since parabolas were identical. Operator's interact was

restricted to locating the heart apex in the images, and determining the parabola and its orientation.

Boundary detection in gamma images is generally considered a very difficult problem, due to the highly distorted nature of the images. A few algorithms have been proposed by a number of workers, which, however, lack the efficiency required by this work; time consumption, laborious statistical calculations, and excessive storage requirements being their principal shortcomings. The principal contribution of this algorithm is that with minimum operator's intervention several tasks were performed, and minimum time consumption and low storage requirements were secured. Additionally, the algorithm is simple in its structure and implementation with impressive results. Appropriate use of a priori information helped to overcome most of the difficulties. Loss of generality is compensated for, if suitable modifications are made to accommodate for imaging other internal organs of the human body.

4. Elimination of Photon Attenuation.

A serious source of image degradation is photon attenuation. A large percentage of the emitted gamma photons from the myocardium never reach the camera because they are absorbed by the matter existing between the area of emission and the camera. Gamma images, constituting two-dimensional projections of the three-dimensional myocardium, do not represent true projections of the myocardium, since of all the photons recorded by the Anger camera only a small

Chapter 10

fraction originated from the 'back-side' of the myocardium. Evidently, any reconstruction attempt would fail to produce accurate results.

The development of the mathematical model of the LV and the arrangement of the images into sets of image-regions corresponding to consecutive slices through the LV, made possible the calculation of the distances between the unit areas of photon emission and the camera for each slice, and thus secured efficient and accurate compensation for photon attenuation.

The main achievement of this algorithm is that the difficult problem of compensating for photon attenuation has been solved in the most efficient manner, requiring minimum computer time and store and being structurally simple. But these advantages were secured by the development of the mathematical model and the boundary detection algorithm. Several workers have used time consuming iterative techniques, involving repetitive 'reconstruction-attenuation' compensating procedures, simply because the capabilities of a priori information were not fully exploited. The effect of photon-attenuation compensation was extensively demonstrated in this work, as infarct definition depended decisively on attenuation elimination.

5. Reconstruction Algorithms.

The reconstruction algorithm is one of the most advanced image processing techniques, because it can reconstitute a three-dimensional source-object from a number of its projected two-dimensional images. It is the back-bone of this research providing the clinician with valuable information, concerning the internal structure of an organ, that other image processing techniques fail to reveal.

Two algorithms were developed, the Straight Pseudoinverse (SP) and the Minimum Least Square Estimate (MLSE), both employing the generalised inverse (pseudoinverse) technique to simulate in the computer the 'reversal' of the image formation process, and thus reconstruct the three-dimensional radioisotope distribution in the LV from three two-dimensional gamma images recorded at different positions around the chest wall. Both algorithms reconstructed consecutive slices of the distribution in the LV, both compensated for photon attenuation, but only the MLSE-algorithm compensated for the Poisson noise. None of the algorithms compensated for the heart motion.

The principle achievement of these algorithms is that they produce accurate reconstructions requiring only three gamma images for each study. This important feature is better realised, if it is considered that it takes about ten minutes of continuous imaging to record a gamma image, a fact that renders most reconstruction

Chapter 10

methods, which require a large number of images, inapplicable for routine patient examination under similar image-collection procedures. Suitable exploitation of a priori information, concerning the anatomy of the LV, has reduced considerably computation and computer core, bringing the operation of both algorithms well within the capabilities of the PDP-11 computer system and the requirements of the particular medical application.

The ability of both methods to reconstruct the radioisotope distribution and determine the location and extent of areas of inactivity was first tested on a conical phantom, then on a healthy human heart, and finally on an infarcted heart. The phantom experiment diluted any doubts of possible artifact reconstructions, since a known area of inactivity was reproduced accurately in location and extent, and this was confirmed by the successful reconstructions of the healthy and infarcted hearts. The major contribution of both algorithms was that they managed to display with accuracy and clarity the location and extent of cardiac infarcts and the muscular texture of the functioning areas of the LV.

Contrasting the two algorithms on their results, the MLSE-algorithm by reducing the Poisson noise effect, produced better reconstructions, as areas of inactivity appeared sharper and areas of activity smoother.

Comparing the algorithms on their operational efficiency, the SP-algorithm is simpler in its structure but more time consuming and core demanding, since it attempts to 'pseudoinvert' larger matrices. But in its clinical implementation, as it is explained in the next section, these matrices need only be inverted once, in which case the SP-algorithm becomes fast and effective.

Concluding it can be claimed with confidence that this work has provided efficient solutions to the difficult problems involved in Emission Imagery. It has demonstrated that the reconstruction problem can be solved successfully using a small number of routinely taken views, without any gating of the Anger camera, without any expensive additional equipment, and in short processing time. It has also proved that efficient use of a priori information, concerning the anatomic structure of the heart and the shape of its projected images, is a necessary provision that guarantees efficient image processing and effective tackling of image degradations involved in Emission Imagery. Consequently, if the achievements of this work are looked at within the perspective of the constraints and limitations imposed, then its uniqueness is apparent.

10.2 CLINICAL IMPLEMENTATION

The algorithms developed in this thesis constitute a logical sequence of operations, which manipulate suitably the cardiac images and eventually reconstruct the radioisotope density distribution in the left ventricular wall. Each algorithm was developed individually but not independently from the others, since its design was influenced by the preceding results, its objective and the overall aim of the research. Hence, each algorithm operated by accepting suitable data from the preceding and providing compatible data to the following algorithm. Employing such methodology of design and writing all programs in FORTRAN IV, it is now possible to consider all algorithms as a compact system or package, in which the overall objective is achieved by the consecutive execution of the local tasks.

This section specifies several conditions necessary for optimum system operation and provides the procedure for package construction and clinical implementation.

(i) Conditions

1. Three images of the heart must be collected, the Anterior and Left-Lateral conventional views and the Middle view at the 45-degree intermediate position, using the existing imaging equipment at Guy's. Images must be stored as 64 by 64 matrices, so that the region of interest (the LV-image)

Chapter 10

can be selected in a 32 by 32 square matrix. Skillful camera positioning can secure automatic selection of the latter matrices.

2. The Modulation Transfer Function (MTF, the Fourier Transform of the system's PSF) must be stored on disc. (Its creation is adequately explained in the relevant chapter).

3. Five different parabolas must be determined using the boundary detection algorithm on cardiac images from different studies. These parabolas must span the range of boundaries from the smallest to the largest possible heart. Then, the generalized inverse of the fractional area matrices (matrix Z in equation $ZB=I$) should be computed and stored for 11 slices and for all five parabolas. Thus, the SP-algorithm can use the 'pseudoinverses' of the parabola which is 'closer' to the boundary parabola of a particular study. It is the belief of the author that such measure does not distort the resulting reconstructions, because the image of the LV occupies a relatively small area in the image matrix and the span of the parabolas does not change significantly (compared to pixel size) at least for the first 8 slices where most infarcts occur. The big advantage of such measure is the enormous reduction in computer time consumption.

4. Operator's interact is restricted to boundary detection procedures- apex of heart, orientation, and 'span' of parabola.

(ii) Reconstruction Package

The Reconstruction Package provides the following facilities:

- a) Fast reconstruction of 11 slices by the SP-method
- b) Provision for examining a small area of interest in the reconstructed image using the superior MLSE-algorithm.
- c) Provision for determining a new boundary parabola, if so desired, computing new fractional-area matrices, and using MLSE-algorithm to reconstruct a selected area of interest.

Figure 10.1 provides a flowchart of the package. Programs are connected by the CHAIN library routine. Analytically, the reconstruction package performs the following tasks:

1. Reads image-matrices (64X64) from store.
2. Selects LV-images in (32X32) matrices from (64X64) image matrices. Each matrix is selected automatically around the centre of the (64X64) matrix. Selection is not critical, since the actual LV-image is usually smaller than the (32X32) size of the selected matrices.
3. Selected images are filtered -smoothing operations are conducted on the images first, and the resulting images are then deconvolved in the Fourier domain from the system's MTF, which is read from store- and stored on disc.
4. The boundaries of the LV are tracked in the following procedure. Each image is plotted on the storage tube screen and the operator determines the coordinates of the LV-apex

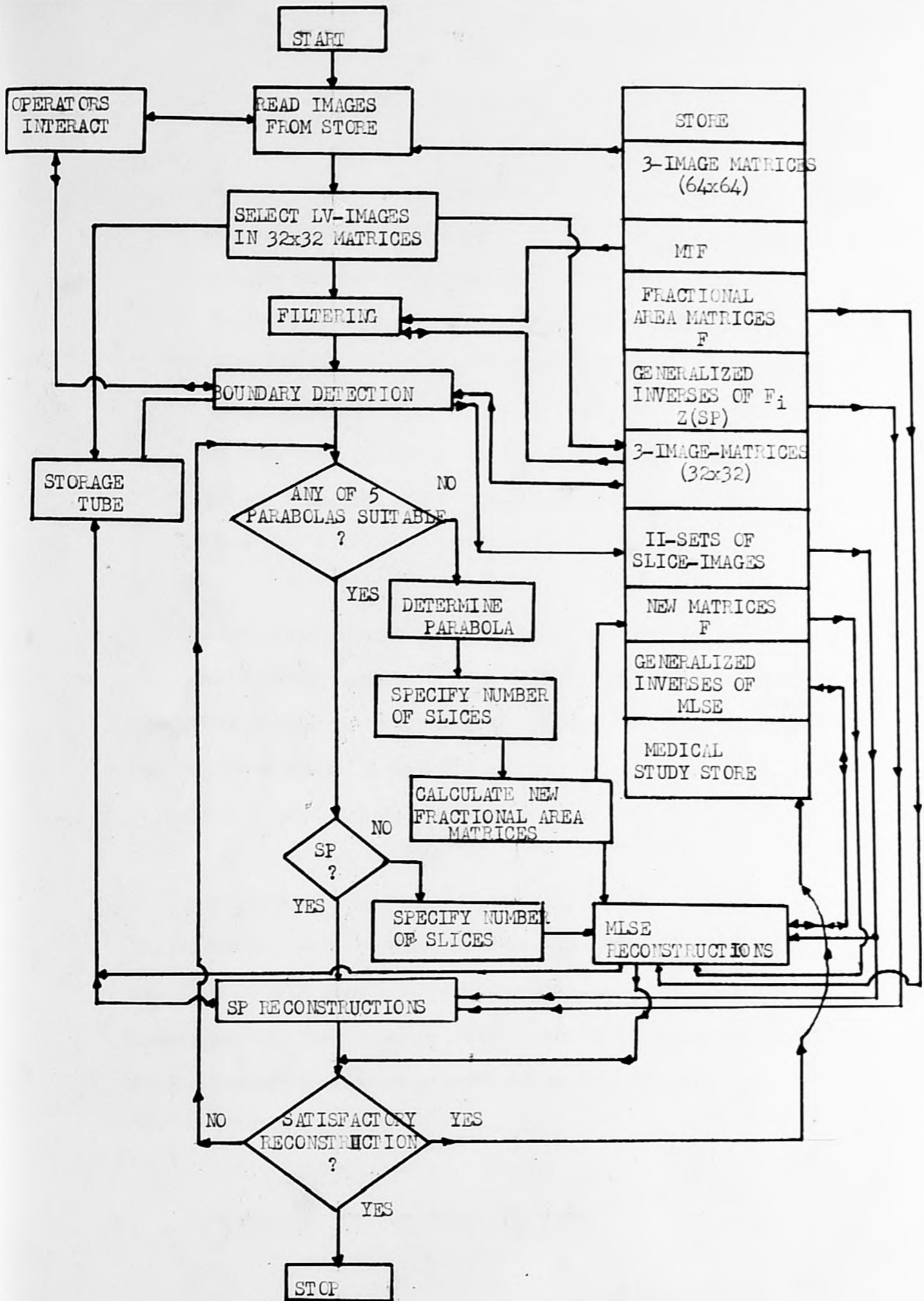


FIGURE 10-1
RECONSTRUCTION PACKAGE

and the parabola orientation. Five parabolas are plotted automatically on top of the first image and the operator chooses the one that fits the LV-boundaries best. The chosen parabola is then plotted on top of the other two images. The algorithm's output is stored on disc as 11 sets of slice-images.

5. The SP-algorithm is used to reconstruct consecutive slices. Results are plotted on the storage tube and stored on disc.

The operator has the facility of re-examining a small area of the reconstructed image by the employment of the MLSE-algorithm. The specific area is determined by the operator, by specifying the desired consecutive slices, and the MLSE-algorithm is then used to reconstruct these slices.

The operator can also determine a new boundary parabola (different to the 5 conventional parabolas), specify the position and magnitude of the area that he wants to reconstruct and employ the MLSE-algorithm (the fastest and most accurate method under these circumstances) to reproduce the radioisotope distribution.

(iii) Storage and Time Specifications

Chapter 10

Specifications concerning storage requirements and execution times are given in table I. Store is divided into Permanent, where programs (in .SAV form) and data are stored, and Scratch, used for temporary data storage. Execution times are given for optimum package operation (5-parabolas technique for boundary detection and SP-reconstructions). For MLSE-algorithm operation about 3.5 minutes per slice are consumed on average. Package operation consumes about 15 minutes for 11 slice-reconstructions and requires 668 blocks of storage on cartridge disc (4800 blocks per cartridge disc). Time consumed for image plotting has not been included, since the storage display unit at Guy's plots images instantaneously.

Chapter 10

PERMANENT STORE

PROGRAMS (.SAV) mode	SPACE (in blocks)	EXECUTION TIME (mins.)
Image selection	62	1
Filtering	32	4
Boundary detection	39	5
SP-algorithm	67	5
MLSE-algorithm	60	
Fract. area matrices progr.	57	

DATA

Three (64x64) images	99	
(32x32) MFT	17	
Fract. area matrices	56	
Pseudoinverses	56	
TOTAL	545	15

SCRATCH STORE

Three (32x32) images	27	
11-slices data	56	
MLSE-Pseudoinverses	29	
TOTAL	123	
OVERALL STORE	668	

Table I

Storage and execution times
for Reconstruction Package on the PDP-11/10.

10.3 FUTURE WORK

The performance of the present reconstruction package can be drastically improved by the inclusion of an algorithm to remove digitally the cardiac motion from the gamma images. This will reduce the number of images required by the package to two, with subsequent reduction in time consumption and storage requirements. It will also improve the accuracy of the reconstructed image, since the images will be now formed by the projection of parallel non-overlapping rays. The author's attempt to obtain good reconstructions employing two gamma images has been proved unsuccessful, after all possible combinations of two images, from the set of three, were tested.

Perhaps, from the different ways that future workers can approach the problem, the most prevailing, to the author's opinion, is the design of a series of MTF's for cardiac motion from measurements on gated and ordinary images of the heart. A probable procedure of tackling the problem may be the following:

(a) For each view of the same heart obtain the gated and ordinary images.

(b) Determine the boundary-parabola from the gated images and apply it on the ordinary images. Deconvolve in the Fourier domain the image sections included in the parabola and thus obtain the MTF corresponding to this parabola and to the particular view.

Chapter 10

(c) Repeat (a) and (b) for hearts of different magnitudes to determine a set of five MTF's for each view, corresponding to the five parabolas of the boundary detection algorithm.

(d) Store those MTF's and examine their effectiveness on the reconstructed images by employing the Reconstruction Package on different heart studies.

The Reconstruction Package can also be modified to examine other internal organs of the human body. Modifications can be easily achieved if suitable exploitation of the anatomic structure of the organs is made and a mathematical model is thus derived in place of the heart's model.

The capabilities of the methods used in the Reconstruction package and in general the overall advantages of the Package for clinical application can provide the basis for future work in exploiting the properties of Emission Imagery for the benefit of medicine.

APPENDICES

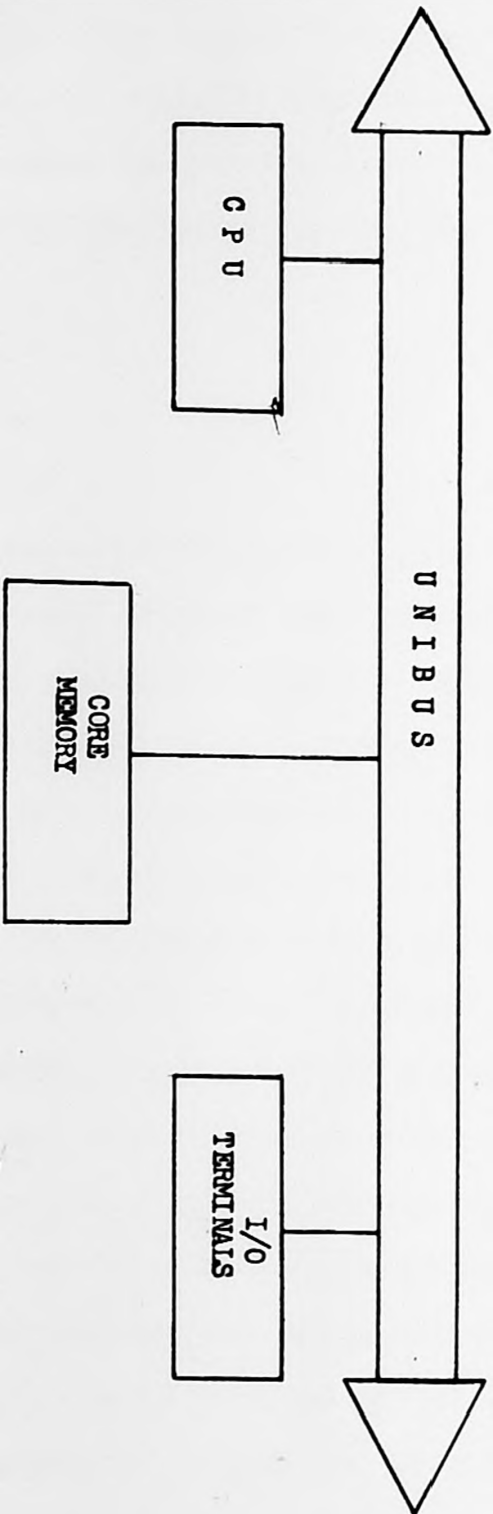
Appendix I

THE PDP-11 COMPUTER.

The PDP-11 computer consists of the UNIBUS, the Central Processing Unit (CPU), and the Core Memory as seen in Figure I(a). Input/Output terminals communicate with the CPU via the UNIBUS.

The PDP-11 computer has the following features:

1. Asynchronous Operation is a mode of computer functioning which guarantees highest possible speed of operation for the different system components. It also safeguards against software and hardware changes in case of replacement of the system's devices.
2. Direct Memory Access (DMA), which provides the possibility of Input/Output transfer without program intervention. The transfer is performed through special channels which steal 'time-slices' from the central processor whenever necessary. The computer logic, performing the DMA, is basically independent of the logic involved in the programmed transfer.
3. Stack Processing, which enables hardware sequential memory manipulation that facilitates efficient handling of the structured data, subroutines, and interrupts.
4. Eight General Purpose Registers, which are fast integrated



I (a) PDP - 11 diagram

APPENDICES

circuits used for accumulators or address generation.

5. Interrupts, which permit the processor to respond automatically to requests from peripheral devices. Upon receiving a request the computer stops the background program and performs the interrupt routine for the peripheral device.

(i) UNIBUS.

The UNIBUS is the hardware that connects all peripheral devices, memories, and the central processor unit, thus establishing a means of system communication. The special feature of the UNIBUS is that the CPU uses the same set of signals to communicate with the core memory and all the I/O devices. Consequently, the same set of program instructions used to reference the memory is used to reference the peripheral devices. Device-status registers, device-control registers, and device-data registers are each assigned a unique memory address[45]. The UNIBUS consists of 56 signal lines. All devices, including the processor, are connected to these lines in parallel. Of the 56 lines 51 are bidirectional, in that they permit signals to flow in either direction, and the remaining five are unidirectional used for priority bus control. Bidirectional and asynchronous communications on the UNIBUS provide the devices with the facility to send, receive, and exchange data independently without the processor's intervention. Communication between two devices takes the form of a 'master-slave' relationship. At any time, the 'master' device controls the bus, while communicating with the 'slave' device. Traffic regulation is achieved

APPENDICES

by assigning priorities to the devices in controlling the UNIBUS. For each control signal sent by the 'master' device there must be a response by the 'slave' device for transfer completion. Full 16-bit words or 8-bit bytes of information can be transferred on the UNIBUS between 'master' and 'slave' devices[46].

(ii) Central Processing Unit

The PDP-11 central processor is a 16-bit general purpose, parallel logic processor using 2's complement arithmetic. The processor can directly address 32,768 8-bit bytes. It is connected to the UNIBUS as a subsystem, controls the time allocation of the UNIBUS for peripherals, and performs arithmetic, logical, and instruction decoding operations. It contains multiple high speed general-purpose registers, which can be used as accumulators, address pointers, index registers, and other specialised functions. It can perform data transfer between I/O devices and memory without disturbing the processor registers[46]. There are 8 general purpose registers. The sixth register is used as the stack pointer, where stack is a temporary data storage area which allows a program to make efficient use of frequently accessed data, by adding or deleting words or bytes within the stack in a 'last-in, first-out' manner (various items may be added in sequential order and retrieved or deleted in reverse order). The seventh register is used as the machine's program counter and contains the address of the next instruction to be executed. There are 400 instructions accomplishing all operations of the PDP-11. The PDP-11 uses both single and double operand address instructions for words or bytes. There are several

APPENDICES

modes of addressing, which include sequential addressing forwards or backwards, addressing indexing, indirect addressing, and stack addressing.

The CPU of the PDP-11/40 computer system has the provision of accepting an Extended Instruction Set (EIS) option, which gives it the capability of performing hardware fixed point arithmetic. Additionally, it can accept the Floating Point Unit, which enables the execution of four special instructions for floating point addition, subtraction, multiplication, and division.

Finally, the CPU includes a time clock and a power supply.

(iii) Core Memory

The computer core memory is composed of a large number of magnetic ferrite cores, each one used to store a bit of information. The direction of magnetization can be changed by changing the direction of the current through a wire threading the core. A 16-bit word is then composed of 16 such cores. Core memory organisation can be viewed as a series of locations, with a number assigned to each location. The PDP-11 memory is designed to accommodate both 16-bit words and 8-bit bytes. The PDP-11 word is divided into a high byte and a low byte. Low bytes are stored at even-numbered memory locations and high bytes at odd-numbered memory locations. Certain memory locations are reserved by the system for interrupt and trap handling, processor stacks, general registers, and peripheral device registers. The rest

APPENDICES

are 'user-locations', in which the user can hold temporarily his program or data.

For the PDP-11/10 version, the available core memory is 24K words, and for the PDP-11/40 system 28K words. For the latter there is provision of extending its core capacity to 128K words by means of the Advanced Memory Management unit, which can be directly interfaced to the PDP-11/40 CPU.

Appendix IIRT-11 OPERATING SYSTEM.

The RT-11 operating system is the part of the computer software, which enables the operator to communicate with the system, program the computer, use the peripherals, and generally render the computer hardware accessible to the user. The RT-11 is specially designed for the PDP-11 minicomputer series. It is a 'single-job' system allowing only one program to reside in core memory at a time. It has, however, the ability to run two programs at the same time in a Foreground/Background mode, in which the foreground program has priority and runs until it relinquishes control to the background, which in turn runs until the foreground program requests continuation of its execution.

These two modes of system operation are handled by two Monitors, the 'single-job' Monitor and the F/B Monitor, which are part of the RT-11 operating system. The user establishes communication with the Monitor through the keyboard terminal by typing commands. There are two types of commands, the 'keyboard' commands and the 'programmed' commands. The 'keyboard' commands are used to load and run the programs, start or restart programs at specific addresses, modify the contents of memory, and assign names to different devices. The

APPENDICES

'programmed' commands, are program instructions requesting Monitor services (utilities), like opening, creating, or closing files.

The RT-11 operating system also incorporates a library of system programs, which provide the user with the facility to develop programs using high level languages (FORTRAN IV, BASIC, FOCAL) or Assembly Language (MACRO-11). Additionally, the system provides a number of software facilities to assist the user in the development of programs. The TEXT-EDITOR, is used to create or modify source files for use as input to the Assembler. The ASSEMBLER or Compiler translates the alphanumeric characters of the program into machine code (binary), to be readily accepted by the computer. A copy of the 'compiled' program is output on the disc device and kept as an object module (.OBJ). The linker combines and relocates separately assembled object programs producing the load module (.SAV), which is the final linked program ready for execution. Files can be renamed, deleted, transferred or listed using the Peripheral Interchange Program (PIP). Debugging of assembled and linked programs can be achieved via the ODT (On-line Debugging Technique). It can be used to print the contents of specified locations, execute all or part of the object program, and search the object program for bit patterns[47].

Appendix IIISINGULAR VALUE DECOMPOSITION-GENERALISED INVERSE.

Lanczos[48] in his attempt to evaluate the Generalised Inverse of a rectangular matrix F ($N \times L, N > L$) has decomposed matrix F into the product of three submatrices, so that the Generalised Inverse Z ($L \times N$) could be systematically computed.

A similar decomposition method is proposed here, which will facilitate the implementation of the Generalised Inverse in the Reconstruction Algorithms.

Equation 7.8 is rewritten here as:

$$B=FI \quad 1.$$

where, $B=(P-N)$ is ($N \times 1$), F is ($N \times L, N > L$), and I is ($L \times 1$).

The product FF^T is a real symmetric matrix with positive or zero eigenvalues. Let F be of rank r , where $r \leq \min\{N, L\}$, so that FF^T ($N \times N$) has r positive and $(N-r)$ zero eigenvalues. If M is a matrix ($N \times N$), which has as columns the normalised eigenvectors of FF^T , then M is orthonormal (i.e. $MM^T = M^T M = I_N$, I_N being the unit or identity matrix) and

APPENDICES

the following holds[31] :

$$M^T (F.F^T) M = R \quad 2.$$

where, R is diagonal, with diagonal elements the r positive eigenvalues of FF^T .

From 2 the following is evident:

$$FF^T = MRM^T \quad 3.$$

Matrix M can be partitioned into two submatrices U and V, such that U contains the eigenvectors of FF^T , corresponding to the positive eigenvalues of FF^T , and V contains the remaining eigenvectors, corresponding to the zero eigenvalues of FF^T . Equation 3 can be represented as:

$$FF^T = \begin{bmatrix} U_{N \times r} & | & V_{N \times (N-r)} \end{bmatrix} \begin{bmatrix} R_{r \times r} & | & 0 \\ \hline 0 & | & 0 \end{bmatrix} \begin{bmatrix} U_{r \times N}^T \\ \hline V_{(N-r) \times N}^T \end{bmatrix} \quad 4.$$

where $R = \text{diag}\{v_1, v_2, v_3, \dots, v_r\}$ are the positive eigenvalues of FF^T .

From 4:

$$FF^T = URU^T \quad 5.$$

APPENDICES

or $FF^T = U\sqrt{R}\sqrt{R} U^T$ 6.

where, the positive sign of the square root is considered. Similarly, the product F^TF , which is $(L \times L)$, can be decomposed into:

$$F^TF = \begin{bmatrix} D_{L \times r} & \\ & E_{(L \times (L-r))} \end{bmatrix} \begin{bmatrix} R_{r \times r} & 0 \\ 0 & 0 \end{bmatrix} \begin{bmatrix} D_{r \times L}^T \\ E_{((L-r) \times L)}^T \end{bmatrix} \quad 7.$$

where, $D (L \times r)$ is the submatrix of the orthonormal eigenvectors of F^TF , corresponding to the r positive eigenvalues of F , and $E (L \times (L-r))$ is the submatrix of the orthonormal eigenvectors, corresponding to the zero eigenvalues. Submatrix R is the same as in 4, since the eigenvalues of FF^T are the same as the eigenvalues of F^TF .

From 7

$$F^TF = DRD^T \quad 8.$$

It is evident that

APPENDICES

$$U^T U = D^T D = I_r \quad 9.$$

$$\text{and } U U^T = I_N, \quad D D^T = I_L \quad 10.$$

since each matrix has orthonormal columns.

Equation 6 can now be written as:

$$F F^T = U T D^T D T U^T = (U T D^T) (U T D^T)^T \quad 11.$$

where, $T = + R$

From equation 11 the decomposition of F is obvious:

$$F = U T D^T \quad 12.$$

From equations 10, U (Nxr) is the left inverse of U^T , and D^T (rxL) is the right inverse of D. Therefore:

$$U = (U^T)^{-1}_{\text{Left}}, \text{ and } D^T = (D)^{-1}_{\text{Right}} \quad 13.$$

and T is a diagonal matrix.

The Generalised Inverse can be now defined as:

APPENDICES

$$Z = DSU^T \quad 14.$$

where,

S: is (rxr) diagonal and its diagonal elements are :

$1/v_1, 1/v_2, 1/v_3, \dots, 1/v_r$, where $v_1, v_2, v_3, \dots, v_r$

are the positive square roots of the eigenvalues of FF^T and

$$v_1 \geq v_2 \geq v_3 \geq \dots \geq v_r$$

D: is (Lxr) consisting of the orthonormalised eigenvectors of FF^T .

U: is (Nxr) consisting of the orthonormalised eigenvectors of FF^T .

Z: is (LxN) the Generalised Inverse of F (NxL).

What is left now is to prove that 14 satisfies all the Penrose conditions. From 7.10, $ZFZ=Z$ and $(FZ)^T = FZ$, are equivalent to:

$$ZZ^T F^T = Z \quad 15.$$

similarly, from $FZF=F$ and $(ZF)^T = ZF$

$$ZFF^T = F^T \quad 16.$$

APPENDICES

Thus it is sufficient to show that Z satisfies 15 and 16. Substituting 14 and 12 in 15,

$$(DSU^T) \cdot (DSU^T)^T \cdot (UTD)^T =$$

$$(DSU^T) \cdot (US^T D^T) \cdot (DT^T U^T) = DSU^T = Z$$

since, $UU^T = I_N$, $D^T D = I_r$, $S^T T = I_r$

Similarly, from 16,

$$(DSU^T) \cdot (UTD)^T \cdot (UTD)^T =$$

$$(DSU^T UTD^T) \cdot (UTD)^T = (UTD)^T = F^T$$

Thus, the decomposition of matrix F (NxL) into the product of three matrices enabled us to express explicitly its Generalised Inverse Z (LxN), which was then proved to be unique, satisfying the Penrose conditions. In case of a non-singular square matrix A (NxN), matrices U and D are constructed by the eigenvectors of A and A respectively, the diagonal matrix T consists of the N eigenvalues of A, and Z is the inverse A^{-1} of A.

REFERENCES

References

1. Robert C. Hsieh and William G. Wce, 'On methods of three dimensional reconstruction from a set of radioisotope scintigrams'. IEEE Trans. Sys. Man. Cyb. vol. SMC-6 no. 12 1976, pp. 854-862.
2. T. F. Budinger and G. T. Gullberg, 'Three dimensional reconstruction in nuclear medicine emission imaging', IEEE Trans. Nucl. Sci. vol. NS-21 no 3 1974, pp. 2-20.
3. T. F. Budinger and G. T. Gullberg, Lawrence Berkeley Laboratory Report, LBL-2146, 1974.
4. T. F. Budinger, 'Three dimensional imaging of the myocardium with isotopes' in Cardiovascular Imaging and Image Processing Theory and Practice, 1975, pp. 263-71.
5. T. F. Budinger, 'Developments in digital computer implementation in nuclear medicine imaging', Comp. Biomed. Res. , vol. 8 no. 1 1975, pp. 26-52.
6. R. L. Kashyap, M. C. Mittal, 'Picture reconstruction from projections', in Proc. 1st. Int. Joint Conf. on Patt. Recogn. 1973, pp. 286-292.

REFERENCES

7. A. J. Rockmore, A. Macovski, 'A maximum likelihood approach to image reconstruction', in Joint Automat. Contr. Conf. 1977, pp. 782-6.
8. D. B. Kay, B. J. Thompson, 'Optical processing in radionuclide tomographic image reconstruction', Optical Engineering, vol. 16 no. 1 1977, pp. 45-51.
9. P. P. Varoutas, L. R. Nardizzi, E. M. Stokely, 'Digital image processing applied to scintillation images from biomedical systems', IEEE Trans. Biomed. Eng. vol. BME-24 no. 4 1977, pp. 337-47.
10. A. Rosenfeld, 'Picture processing by computer', Academic Press, 1969.
11. A. Rosenfeld, A. C. Kak, 'Digital image restoration', Academic Press, 1976.
12. H. C Andrews, B. R. Hunt, 'Digital picture processing', Prentice-Hall, Inc. 1977.
13. G. J. Hine, 'Instrumentation in Nuclear Medicine', Academic Press 1977.

REFERENCES

14. L. R. Rabiner, B. Gold, 'Theory and application of digital signal processing', Prentice-Hall, Inc. , 1975.
15. N. Ahmed, K. R. Rao, 'Orthogonal transforms for digital signal processing', Springer-Verlag, 1975.
16. J. H. Wilkinson, C. Reinsch, 'Handbook for automatic computation', vol. II, Linear Algebra, Springer-Verlag, 1971.
17. D. Cavouras, 'Three dimensional reconstruction of an object from four of its two dimensional images. ' Report DSS/DC/174 Department of Systems Science, The City University, October 1978.
18. T. F. Budinger et. al, 'Emission computed tomography', Chapter 5 of image reconstruction from projections, vol. 32, of Topics in Applied Physics-Springer 1979.
19. A. C. Kak, 'Algorithms for reconstruction', Cardiovascular imaging and image processing, Theory and Practice, 1975.
20. R. J. Jaszczac et al, 'Radionuclide emission computed tomography of the head with ^{99m}Tc and a Scintillation Camera. ', J. Nucl. Med. , vol. 18 no. 4, pp. 373-380, 1977.

REFERENCES

21. R. Rob, et al, 'Three dimensional reconstruction and display of the heart, lungs and circulation of multiplanar X-ray scanning video densitometry', Cardiovascular imaging and image processing , Theory and Practice, 1975.
22. J. W. Keyes, Jr. , et al, 'The Homogotron-A scintillation camera transaxial tomograph. ', J. Nucl. Med. , vol. 18, no. 4, pp. 381-387, 1977.
23. R. A. Vogel, et al. , 'A new method of multiplanar emission tomography using a seven pinhole collimator and an Anger camera'. J. Nucl. Med. , vol. 19, pp. 648-654, 1978.
24. R. S. Burington 'Handbook of mathematical tables and formulas'. McGraw-Hill Book Company, fifth edition, 1973.
25. J. D. Payne, et al., 'Comparison and performance of Anger cameras'. Radiology, 109: 381-386, Nov. 1973.
26. T. F. Budinger, 'Digital image processing for medical diagnosis using gamma radionuclides and heavy ions from cyclotrons'. Digital processing of biomedical images, editors: K. Preston and M. Onoe, Plenum press, 1976.

REFERENCES

27. B. R. Hunt, 'Digital image processing'. Applications of digital image processing, Oppenheim, Prentice Hal, Inc.1978.
28. A. K. Boardman, 'Constraint optimisation and its applications to scintigraphy'. Phys. Med. Biol., Vol.24, No.2, pp:363-371, 1979.
29. R. Penrose, 'A generalised inverse for matrices'. Proc. Camb. Phil. Soc., 51, pp:406-413, 1955.
30. R. Penrose, 'On best approximate solutions of linear matrix equations'. Proc. Camb. Phil. Soc., 52, pp:17-19, 1956.
31. D. I. Steinberg, 'Computational matrix algebra'. McGraw-Hill, 1974.
32. R. C. Mead et al, 'Quantitative methods in the evaluation of Thallium-201 myocardial perfusion images'. J. Nucl. Med., Vol.19, pp:1175-1178, 1978.
33. G. W. Hamilton, 'Thallium-201 myocardial imaging: characterisation of the ECG-synchronised images'. J. Nucl. Med., Vol.19, pp:1103-1110, 1978.
34. D. E. Kuhl, R. Q. Edwards, 'Image separation radioisotope scanning'. Radiology 80, pp:653-661, 1963.

REFERENCES

35. G. N. Hounsfield, 'Computerised transverse axial scanning (tomography) Part 1. Description of system'. Br. J. Radiology 46, pp:1016-1022, 1973.
36. R. S. Ledley, 'Introduction to computerised tomography'. Comp. Biol. Med., Pergamon press, Vol.6, pp:239-246, 1976.
37. B. R. Hunt, 'The application of constraint least squares estimation to image restoration by digital computer'. IEEE Trans. Comp., Vol. C-22, No.9, Sep. 1973.
38. C. H. Chow and T. Kaneko, 'Boundary detection of radiographic images by a threshold method'. IEEE Trans. Comp., Vol. C-22, pp:1530-1535, 1973.
39. G. T. Herman and H. K. Liu, 'Dynamic surface detection'. Proc. of the Sympos. on comp. aided diagnosis of med. imag., Nov.11, pp:27-32, 1976.
40. M. Kuwahara et al, 'Processing of RI-Angiocardiographic images'. Digital processing of biomedical images, editors: K. Preston and M. Onoe, Plenum press, 1976.
41. H. O. Anger, 'Scintillation camera'. Rev. Sci. Instrum., 29, pp:27-33, 1958.

REFERENCES

42. F. J. Th. Wackers, R. B. J. De Jong, 'Myocardial imaging with Thallium-201'. *Medicamundi*, Vol.21, No.2, pp:103-113, 1976.
43. D. J. H. Moore and D. J. Parker, 'On non-linear filters involving transformation of the time variable'. *IEEE Trans. Inf. Th.*, Vol.It-9, No.4, July 1973.
44. *Encyclopaedia Britannica. The Heart.*
45. B. Soucek, 'Minicomputers in data processing and simulation'. *Wiley-Interscience*, 1972.
46. D.E.C. 'PDP-11/10 and PDP-11/40 processor handbook'. *Maynard Massach.*
47. D.E.C. 'RT-11 reference manual'. *Maynard Massach.*
48. C. Lanczos, 'Linear systems in self adjoint form'. *Amer. Math. Month.*, Vol.65, pp:665-679, 1958.
49. D.E.C. 'Gamma-11 Manual'. *Maynard Massach.*
50. H. A. Enge, 'Introduction to Nuclear Physics'. *Addison-Welsey Publ.Co.*, 1971.

REFERENCES

51. G. T. Herman and R. M. Lewitt, 'Overview of image reconstruction from projections'. Vol.32 of Topics in Applied Physics-Springer, 1979.
52. R. M. Mersereau, 'Direct Fourier Transform techniques in 3-d image reconstruction'. Comp. Biol. Med., Pergamon press, Vol.6, pp:247-258, 1976.
53. R. O. Duda and P. E. Hart, 'Pattern classification and scene analysis'. Wiley Interscience Publ., 1973.
54. T. A. Iinuma and T. Nagai, 'Image restoration in radioisotope imaging systems'. Phys. Med. Biology, Vol. 12, pp:501-509, 1967.
55. C. W. Helstrom, 'Image restoration by the method of least squares'. J. Opt. Soc. Am., Vol. 57, pp:297-303, 1967.
56. D. Slepian, 'Linear least squares filtering in distorted images'. J. Opt. Soc. Am., Vol. 57, pp:918-922, 1967.